



Minnesota State University, Mankato
Cornerstone: A Collection of Scholarly
and Creative Works for Minnesota
State University, Mankato

All Undergraduate Theses and Capstone
Projects

Undergraduate Theses and Capstone Projects

2022

Thermal Testing and Simulation of Lunar and Martian ISRU-Based Materials

Andres Campbell
Minnesota State University, Mankato

Follow this and additional works at: <https://cornerstone.lib.mnsu.edu/undergrad-theses-capstones-all>



Part of the [Aerospace Engineering Commons](#)

Recommended Citation

Campbell, A. (2022). Thermal testing and simulation of Lunar and Martian ISRU-based materials [Bachelor of Science thesis, Minnesota State University, Mankato]. Cornerstone: A Collection of Scholarly and Creative Works for Minnesota State University, Mankato. <https://cornerstone.lib.mnsu.edu/undergrad-theses-capstones-all/4/>

This Thesis is brought to you for free and open access by the Undergraduate Theses and Capstone Projects at Cornerstone: A Collection of Scholarly and Creative Works for Minnesota State University, Mankato. It has been accepted for inclusion in All Undergraduate Theses and Capstone Projects by an authorized administrator of Cornerstone: A Collection of Scholarly and Creative Works for Minnesota State University, Mankato.

THERMAL TESTING AND SIMULATION OF LUNAR AND MARTIAN ISRU-BASED MATERIALS

By Andres Campbell

A Senior Thesis Submitted in Partial Fulfillment of the
Requirements for the Degree of
Bachelor of Science
in
Engineering with an Aerospace Focus

Minnesota State University, Mankato
Mankato, Minnesota
April 2022

April, 2020

Thermal Testing and Simulation of ISRU-Based Materials

Andres Campbell

This Senior Thesis has been examined and approved by the following members of the student's committee.

Dr. Jacob Swanson

Dr. Rebecca Bates

Michael Fiske

Dr. Robert Sleezer

ACKNOWLEDGEMENTS

I would first like to thank my peers and faculty within the Twin Cities Engineering program for their flexibility and support throughout my education at MSU, Mankato. I would like to thank my fellow members of the Lunar PAD team for their work on the Lunar PAD project that led to this thesis and their support throughout. I would like to thank Michael Fiske, Dr. Curtis Banks, and Jaxson Earwood at Marshall Space Flight Center for their execution of the physical experiment component. This work would not have been possible without the support of Brianna Anklam, Rosamaria Campbell, Alejandra Pelinka, Cindy Campbell-Lashley, Evelyn Lashley, and other members of my family.

Table of Contents

Acknowledgements	ii
Abstract	vi
1. Introduction	1
2. Background	3
A. Previous Work	3
B. Structural Health Monitoring.....	5
C. CAD, FEA, & CFD Simulations	6
D. Materials	9
1. Test 1: 6061 Aluminum Alloy.....	13
2. Test 2: CSA and Lunar Regolith Simulant.....	15
3. Test 3: MgO and Martian Regolith Simulant	17
4. Test 4: Lavacrete	19
3. Methodology	21
A. Guidelines for Design of Experimentation.....	21
B. Physical Experiment	24
C. Simulated Experiment	30
1. CAD Models.....	30
2. CFD Environmental Parameters.....	32
3. CFD Propane Torch Flame Parameters	33
4. CFD Simulation Setup Parameters	37

5.	FEA Simulation Parameters	41
D.	Data Analysis and Calculation	43
1.	Simulated Temperature Gradient Calculation	45
2.	Experimental Temperature Gradient Calculation.....	46
4.	Results	47
A.	CFD Simulation Results	48
1.	Simulated Images	48
2.	Simulated Experiment Data.....	56
B.	Physical Results	59
1.	Physical Experiment Images	59
2.	Physical Experiment Data	62
C.	Comparison Results	65
1.	Simulated and Physical Data	65
2.	Simulated and Physical Flame Contact	67
D.	Calculated Results.....	73
1.	Temperature Gradient Calculation Results.....	73
E.	FEA Simulation Results	74
1.	Simulated Strain Images.....	74
2.	Simulated Stress, Strain, and Displacement Data.....	77

5. Discussion & Conclusion.....	78
A. Discussion.....	78
1. Similarities and differences between simulated and physical experiments....	78
2. Effects of aggregate on thermal conductivity.....	88
3. Simulated strain response to temperature.....	92
4. Other possible influences on strain not seen in simulations.....	97
5. Mass loss of samples	99
B. Conclusion.....	101
1. Future Work.....	101
2. Conclusion.....	104
3. Summary.....	108
6. Nomenclature	109
7. References	110

Thermal Testing and Simulation of Lunar and Martian ISRU-Based Materials

Andres Campbell

A Senior Thesis Submitted in Partial Fulfillment of the
Requirements for the Degree of
Bachelor of Science in
Engineering with an Aerospace Focus

Minnesota State University, Mankato
Mankato, Minnesota
April, 2022

ABSTRACT

Upon the eventual return of humans to the lunar surface, leveraging local resources to construct landing pads and other infrastructure is an essential component to minimize cost and risk. The inability to accurately model landing and launch scenarios to predict damage to lunar structures poses risks to astronaut and equipment safety. The following experiment is an investigation of using simulation software and temperature sensors to model lunar and Martian regolith simulant-based concrete exposed to thermal loads. The basis of this experiment is built upon standards defined by the American Society for Testing and Materials, the fundamental axioms of structural health monitoring, simulation software capabilities and limitations, and the properties of likely candidates for materials used for lunar and Martian in-situ construction. Parallel testing was with simulation software, and physical equipment with material cube samples. The goal of this testing is to collect comparable temperature data to determine the accuracy of the simulation and determine the resulting temperature and strain response within the material. This thesis seeks to address the lack of characterization of lunar and Martian regolith simulant-based concrete in their expected use conditions. The outcomes of this experiment serve as a preliminary basis for future testing and characterization of in-situ based materials to be used to create critical infrastructure to support a sustained human presence on the moon and Mars.

1. INTRODUCTION

As humans establish an extended presence on the moon and Mars, several types of structures become necessary to ensure the safety of astronauts, landers, and other equipment. Examples of these structures include landing pads that protect the lander and surrounding equipment from high-velocity particles, habitats and shelters that protect astronauts, and roadways that prevent equipment degradation due to dust accumulation. The scope of many of these structures extends well beyond what we can reasonably expect to load, launch, and deploy from Earth due to cost and complexity. As a result, the need for in-situ resource utilization (ISRU) for construction and other purposes has become especially apparent. These local resources can be used with existing additive manufacturing technologies to create many of these structures. Additive manufacturing (AM) intended for the moon and Mars has made significant advancements in recent years with projects like the NASA 3D-Printed Habitat Challenge, the PISCES ISRU-based analog test site and landing pad, and the Lunar PAD 3D-printed landing pad for cratering and dust mitigation. Structural health monitoring (SHM) has been used for civil engineering projects like bridges and buildings, with hundreds or thousands of sensors used to measure various parameters. The implementation (and possible modification) of Earth-based structural health monitoring techniques is a component of extraterrestrial construction that has yet to be fully investigated. A combination of computational fluid dynamics (CFD) and finite element analysis (FEA) simulation software is frequently used to virtually assess structures before they are constructed or implemented. The advantage of

these simulations is that they are low-cost and low risk while providing a plethora of information, but the accompanying disadvantage is that it is nearly impossible to create a perfectly realistic representation of the materials, structure, or conditions. Many of the ISRU materials and processes used to create these structures is vastly different from what would typically be used on Earth and may require different considerations. Although SHM techniques require investment in tools and expertise, the value of its implementation outweighs the cost.

This experiment seeks to address the disparity between terrestrial SHM techniques and extraterrestrial materials and conditions using a small-scale test and simulation. The underlying background information presented here focuses on structural health monitoring techniques used on Earth, capabilities and limitations of the simulation software used, and ISRU materials for extraterrestrial structures. The experiment is divided into two parallel parts, with the first being a physical test of material samples under a propane torch, and the second being a simulated recreation of that test. The data from the physical and simulated tests are then compared to each other to verify the reliability of the simulation with respect to the empirical data.

2. BACKGROUND

A. Previous Work

The Lunar PAD project began in 2019 with the goal of designing a landing and launch pad for extraterrestrial surfaces, such as the moon and Mars. Since its inception, I have served as the principal investigator of the undergraduate student team leading the research and design of a 20 foot-diameter subscale pad. This subscale design would serve as a proof-of-concept for using ISRU and AM methods (concrete 3D printing) to construct a necessary piece of lunar infrastructure. The subscale pad was constructed in October 2020 with instrumentation support from NASA Marshall Space Flight Center (MSFC) and construction support from ICON, an Austin, Texas-based concrete 3D printing company. A subscale hot-fire test was performed in March 2021 with support from Texas A&M University. The research, design, construction, testing, and analysis work done on the Lunar PAD project influenced many of the goals and methods used in this experiment. Examples of the influence of the Lunar PAD project include the basis of the experiment, the inclusion of certain materials, and the use of specific software and tools.

The subscale Lunar PAD was constructed using a combination of traditional and ISRU-based methods and used ICON's proprietary Lavacrete material with lunar regolith simulant fiber-woven rebar. The Lunar PAD design underwent several iterations of simulations using SolidWorks packages to determine the effectiveness of the design in mitigating both plume stagnation and high velocity ejecta. However, these simulations were unable to recreate the erosion damage to the pad directly underneath the motor in the

hot fire test shown in Figure 1. Despite the pad being instrumented with thermocouples, pressure transducers, and fiber optic strain sensors, the full extent of internal and external damage was impossible to fully predict given the extreme conditions of the exhaust plume. During the pad construction in October 2020, various types of Lavacrete samples were collected with the intent of performing tensile, compression, and three-point bend testing. Additional cube samples were created to test the temperature response, which were used for this experiment. Those samples were returned to MSFC, and additional cube samples of ISRU-based materials were created, which allowed for extra experimentation that led to this thesis.



Figure 1a – 1b: Photos taken of the Lunar PAD before (a) and after (b) the hot-fire test. Enhanced contrast for clarity.

B. Structural Health Monitoring

Many civil engineering applications use structural health monitoring instrumentation and techniques to track various conditions, experienced by structural members. There are several “fundamental axioms of structural health monitoring” that are an influence on the approach of this thesis (Worden, Farrar, Manson, & Park, 2007). Each of these axioms are explained in depth by K. Worden, et.al. and many of those concepts are cited and connected to relevant aspects of this experiment in subsequent sections. This project aims to take some of these structural health monitoring axioms designed for Earth-based structures and apply them to structures on the moon or Mars that utilize local resources for construction. Each of the listed axioms serve as a guide for the purpose and procedure of the following experiment.

Axiom I: All materials have inherent flaws or defects;

Axiom II: The assessment of damage requires a comparison between two system states;

Axiom III: Identifying the existence and location of damage can be done in an unsupervised learning mode, but identifying the type of damage present and the damage severity can generally only be done in a supervised learning mode;

Axiom IVa: Sensors cannot measure damage. Feature extraction through signal processing and statistical classification is necessary to convert sensor data into damage information;

Axiom IVb: Without intelligent feature extraction, the more sensitive a measurement is to damage, the more sensitive it is to changing operational and environmental conditions;

Axiom V: The length- and time-scales associated with damage initiation and evolution dictate the required properties of the SHM sensing system;

Axiom VI: There is a trade-off between the sensitivity to damage of an algorithm and its noise rejection capability;

Axiom VII: The size of damage that can be detected from changes in system dynamics is inversely proportional to the frequency range of excitation.

C. CAD, FEA, & CFD Simulations

The simulated component of this experiment was performed using SolidWorks 2020 Student Edition for Computer Aided Drawing (CAD), the accompanying Finite Element Analysis (FEA) SolidWorks Simulation, and Computational Fluid Dynamics (CFD) SolidWorks Flow Simulation packages. CAD software is frequently used to model individual parts, connected assemblies, and use other software packages to analyze the assembly in various ways. One of the goals of this experiment is to use flow and loading simulations to estimate the thermal and structural response of materials under extreme thermal loads. The simulation software used in this experiment was successfully used for previous simulation work on the Lunar PAD project, with extreme temperature conditions from the solid rocket motor exhaust being somewhat comparable to the temperatures produced by the propane torch.

Limitations of the SolidWorks simulation software relevant to this experiment include the inability to accurately model combustion, multi-phase flow, multiple fluids in a single subdomain, and sub-atomic material structures. SolidWorks Flow Simulation 2020 is incapable of simulating combustion, or the reaction of heat, fuel, and oxygen. As a result, “combustion” is represented as either a heat source applied to a face or volume, or a fluid source with a higher temperature than the environmental fluid. Similarly, the software can only simulate a single fluid within a volumetric domain. While the software can simulate multiple fluids in separate sealed containers, the external simulation used in this experiment causes the entire computational domain to be a single volume. As a result, the environmental fluid (in this case, air) must be the same as the ejected fluid. Furthermore, the software is unable to simulate phase changes, such as the evaporation of water, as this would be two different fluids (liquid water & gaseous water) in the same domain. SolidWorks Flow Simulation is capable of defining geometries as a porous medium to allow flow through a material. However, the specified porosity of a material is not reflected in the sub-atomic structure of the CAD model. The sub-atomic structure is a significant consideration for many material properties and the resulting response to high temperatures. Despite these limitations, SolidWorks remains a relatively accurate and effective tool for flow simulations and finite element analysis.

The reason for selecting SolidWorks and SolidWorks simulation packages for this experiment was based on previous work with similar conditions. Previous work on the Lunar PAD project using SolidWorks simulation packages was used for the re-creation of

a solid rocket motor static hot-fire test. Dr. Adonios Karpetis at Texas A&M University assisted with calculating the motor flow parameters and confirmed that the simulation results were similar to exhaust plumes seen in his previous work with rocket exhaust modeling. After the hot-fire test, data was collected from various sensors installed on the Lunar PAD. This data was compared with virtual sensors placed in similar locations on the simulation. Dr. Peter Liever is a CFD simulation specialist at NASA Marshall Space Flight Center and confirmed our physical data and simulated data were reasonably similar, with more details published in the *Lunar PAD Post-Hot Fire Test Performance Evaluation* conference paper (Campbell, et al., 2022).

SolidWorks was also selected based on the flow calculation capabilities of the software. Like most other CFD simulation software, SolidWorks Flow Simulation uses Navier-Stokes equations as the foundation for calculating laminar flow conditions in fluid regions. These equations are supplemented by fluid state equations for density, viscosity, and thermal conductivity where applicable. Furthermore, SolidWorks calculates laminar, transitional, and turbulent flow using a modified k-epsilon ($k-\epsilon$) model. This is especially important, as we are certain to see turbulent flow given the high temperature of the flame and high pressure at the stagnation point where the flame contacts a surface. An accurate calculation of turbulence near the stagnation region is needed to reliably determine the heat flux through the material. The $k-\epsilon$ model is a two-equation turbulent model for CFD and uses partial differential transport equations to describe the transport of kinetic energy (k) and turbulent dissipation (ϵ). The modified version used in SolidWorks has proven to be a reliable method

of calculating flow near a wall without needing to introduce additional terms into the transport equations or additional wall functions (Lam & Bremhorst, 1981). By reducing computation time and complexity for near-wall flow without compromising calculation accuracy, we can allocate more resources to generate a finer mesh which increases the resolution of results. The ability to accurately calculate near-wall turbulent flow and previous experience with modeling extreme temperature scenarios prove SolidWorks Flow Simulation as a capable and preferable tool to execute the simulated component of this thesis.

D. Materials

This section begins with a brief background of why we are using in-situ resource utilization, and how this concept connects with the material testing performed in this thesis. An overview of the components of concrete will be followed by a more in-depth discussion of aggregate, cement, and the effects of concrete components on material properties. Finally, with that context established, the specific materials being tested in this thesis will be discussed qualitatively and quantitatively.

Resources on the moon and Mars can be used with additive manufacturing to minimize launch up-mass costs while constructing critical infrastructure. The collection of regolith as an aggregate enables the creation of many variations of concrete. Different methods may rely on the use of other materials, such as binders or additives. The goal of constructing safe and reliable infrastructure on the moon and Mars is most efficiently met by using local

resources, such as regolith, with additive manufacturing. The properties of regolith on the moon and Mars vary widely between different regions. The primary focus of human settlement missions to the moon is on local water availability, which presents the south pole region as a likely settlement candidate with its permanently shadowed craters holding water ice. The lunar south pole also contains basalt rock found in lunar mare regions. This basalt rock is an appealing candidate for a lunar-based aggregate, and JSC – 1A Lunar Regolith Simulant (LRS) closely resembles natural lunar basalt in many ways. Based on the information we have from robotic missions to Mars, JSC – Mars 1A Martian Regolith Simulant (MRS) is similarly regarded as a close analog of real Martian regolith (Allen, et al.). Although we have not yet fully characterized the properties of ISRU materials like the ones we have on Earth, their components (aggregate and cement) have been analyzed to some degree.

Concrete, in general terms, consists of an aggregate and paste. The aggregate material accounts for a majority of the volume of concrete and is characterized as fine or coarse. Fine aggregates, such as sand, are less than 0.375-inch in diameter while coarse aggregates, such as gravel, are between 0.375 and 1.5 inches in diameter (Portland Cement Association, n.d.). The paste is a combination of water and cement for most applications. One of the defining properties of the paste is the water-cement ratio (W/C), defined by the weight of water divided by the weight of cementitious material. The combination of cement and water in various W/C ratios creates a chemical reaction that binds the aggregate and eventually cures to form concrete.

Conventional concrete typically contains sand and stone as the aggregate, and water and cement as the binding paste. The aggregate component is usually a majority of the mass and volume of concrete, and as a result, a majority of the properties of the concrete are dependent on the properties of the aggregate. Additionally, a bulk quantity of a particular type of aggregate can vary in particle diameter, shape, density, and other mechanical properties. The variability of aggregate particles is constrained by requirements like ASTM C33/C33M – 16 “Standard Specifications for Concrete Aggregates”. The cementitious material is usually a combination of calcium carbonate, such as limestone or chalk, and aluminum silicates, such as clay or shale. The combination of water and cement alone forms a thin slurry that still requires aggregate to fully react to form a stable concrete.

The resulting mixture can create a wide variety of structural features that are “random” at the atomic level but can be generally characterized. These atomic-level differences in structures can still be impactful on the thermal conductivity and overall performance of the material under extreme heat conditions. Several studies have investigated the relationship between thermal conductivity and other concrete material properties (Asadi, Shafigh, Hassan, & Mahyuddin, 2018). This review of thermal conductivity by Asadi, Shafigh, Hassan, and Mahyuddin used hot wire and plane source transient testing, and hot plate steady-state testing, as per ASTM C177. This compilation of thermal conductivity values and functions is used in place of more specific values for the materials used in this thesis. For example, the thermal conductivity of the specific combination of lunar regolith simulant aggregate mixed with Calcium Sulfoaluminate (CSA) cement (a combination of

materials used in this thesis) has not yet been tested and characterized. As a result, many of the properties defined in the tables below are of other, similar materials, where applicable. Later sections in this thesis will discuss the alignment between these extrapolated thermal conductivity values and the actual thermal conductivity of the physical test samples.

This thesis aims to test and compare the performance of materials that would likely be used for lunar and Martian ISRU structures. As a result, each test is classified according to the unique cement, aggregate, and additives used (with the exception of the 6061 aluminum alloy) and correspond to their respective test numbers, as shown in Table I below.

TABLE I. SUMMARY OF MATERIAL SAMPLE COMPOSITION

Test	Cement	Aggregate	Additives
1	Unwrought 6061 Aluminum Alloy	N/A	N/A
2	Calcium Sulfoaluminate (CSA)	JSC – 1A “Lunar Regolith Simulant”	Citric acid set retardant
3	Magnesium Oxide (MgO) w/ Monopotassium Phosphate (MKP)	JSC – Mars 1A “Martian Regolith Simulant”	Boric acid set retardant
4	“Lavacrete” – Proprietary blend based on Ordinary Portland Cement	Sand + Gravel (ASTM C33)	Unknown, proprietary

Test 2 and Test 3 materials are recognized as likely candidates for creating in-situ structures on the moon and Mars because they utilize a simulated local resource as the primary aggregate. Test 1 and Test 4 materials serve as reference materials commonly used on Earth, with Lavacrete also having been used for the Lunar PAD. In order to recreate the physical experiment in a simulation and draw meaningful conclusions from the

comparison, we must identify and investigate the prevailing properties of each material with the following additional assumptions:

- All concrete materials and listed material properties contain a water – cement (W/C) ratio of 0.3 – 0.4
- All materials and listed material properties are assumed to be a completely homogenous mixture of its constituents.
- All material structures are assumed to be isotropic.
- All listed materials properties indicated as “averaged” are representative of the average taken between the lower and upper limit of the range of values given by the source.
- All listed materials properties in the following tables are not representative of the “typical” sample, nor are they representative of the samples used in this thesis. These values serve as an initial basis for simulation input parameters, and subsequent analysis.

Chapter 5 will further explore the validity of using these assumptions. Each material is discussed in terms of the context in which they are used on Earth or the moon, notable qualities of the material structure or composition, and a table of values to be used for simulations.

1. Test 1: 6061 Aluminum Alloy

Aluminum alloys are commonly used on Earth across many industries for its relatively low mass, high strength, and workability. Aluminum alloys all have aluminum as the predominant metal but are further distinguished by their alloying elements and manufacturing processes. Upon the introduction of magnesium and silicon as the alloying

metals with aluminum, the resulting material is classified as 6061 grade aluminum alloy. The microstructure of this particular sample is considered unknown, as it varies widely with the exact preparation method. This sample was unwrought, meaning there was no additional manufacturing processes, such as rolling, forging, and drawing. This implies that the average grain size is larger than a wrought material sample. The grain size of metals has been shown to have a direct effect on thermal conductivity (Ihlefeld, Brown-Shaklee, & Hopkins, 2011). All of the simulation material properties in Table II were found for 6061 aluminum alloy, but it is unknown whether they are applicable to wrought or unwrought and the effects of this discrepancy are not the primary focus of this paper.

TABLE II. 6061 ALUMINUM ALLOY MATERIAL PROPERTIES

Property	Value	Type – Source
Elastic Modulus [GPa]	68.9	Aluminum 6061 – (The Aluminum Association, Inc., Revised 2001)
Poisson’s Ratio [dimensionless]	0.33	Aluminum 6061 – (The Aluminum Association, Inc., Revised 2001)
Shear Modulus [GPa]	26	Aluminum 6061 – (The Aluminum Association, Inc., Revised 2001)
Mass Density $\left[\frac{kg}{m^3}\right]$	2700	Aluminum 6061 – (The Aluminum Association, Inc., Revised 2001)
Tensile Strength [MPa]	310	Aluminum 6061 – (The Aluminum Association, Inc., Revised 2001)
Compressive Strength [kPa]	22.610	Aluminum 6061 – (Ravi, Sivananthan, & Samuel, 2019)
Thermal Expansion Coefficient $\left[\frac{1}{K}\right]$	22e-6	Aluminum 6061, averaged – (Applied Ceramics, Inc., n.d.)
Thermal Conductivity $\left[\frac{W}{m*K}\right]$	167	Aluminum 6061 – (The Aluminum Association, Inc., Revised 2001)
Specific Heat $\left[\frac{J}{kg*K}\right]$	8	Aluminum 6061 – (The Aluminum Association, Inc., Revised 2001)

Emissivity [<i>dimensionless</i>], wavelength dependent	0.15, 1000 μm 0.11, 1600 μm	Aluminum 6061, averaged – (Fluke Process Instruments, 2021)
Absorptivity $\left[\frac{1}{\text{mm}}\right]$, wavelength dependent	0.07, 100 μm 0.075, 200 μm 0.035, 300 μm 0.07, 400 μm 0.075, 500 μm 0.07, 600 μm 0.075, 700 μm 0.065, 800 μm 0.09, 1100 μm 0.095, 1500 μm 0.13, 2000 μm	Aluminum 6061 – (Tunna, O'Neill, Khan, & Sutcliffe, 2005)
Refractive index [<i>dimensionless</i>]	1.44	Aluminum 6061 - (Yaws, 1999)

2. Test 2: CSA and Lunar Regolith Simulant

Calcium Sulfoaluminate (CSA) cement is a common fast-setting hydraulic cement (FSHC), similar to ASTM Type III Ordinary Portland Cement. The primary appeal of FSHC is that its compressive strength develops quickly over the curing period. Many of the material properties of CSA that would be used for accurately recreating the material in simulations were given as a range and/or heavily dependent on the exact mixture or process used. As a result, many of the properties shown in the table below use a combination of values from CSA-specific studies and Type III Ordinary Portland Cement concrete and are indicated as such. The microstructure of CSA-based concrete has been investigated alongside OPC concrete properties for similarly sized cubic samples (Bescher, 2018) and have revealed several relevant properties to this thesis. The cumulative pore volume and average pore diameter of CSA concrete is significantly less than Type III OPC concrete. The lower pore volume indicates less overall negative space within a given volume of

concrete, thus increasing density. The average pore diameter distribution between CSA and Type III OPC concrete further supports this trend, as a majority of CSA concrete pores are ~ 0.008 microns in diameter with a total volume ~ 0.15 cubic microns, compared with the majority of Type III OPC concrete pores being ~ 0.08 microns in diameter with a total volume of ~ 0.37 cubic microns. Unfortunately, the CAD and simulation software is incapable of allowing the modification of such specific properties. Citric acid was also added to the mixture as a set retardant. A study investigated the incorporation citric acid into various types of concrete and found that several mechanical properties were affected (Khalil, 2009). This includes a decrease in the W/C ratio and increase in compressive strength, splitting tensile strength, modulus of rupture, and dynamic modulus of elasticity at all ages. Table III lists the material properties applied to the simulated experiment.

TABLE III. JSC – 1A LUNAR REGOLITH SIMULANT + CSA CEMENT CONCRETE MATERIAL PROPERTIES

Property	Value	Type – Source
Elastic Modulus [GPa]	38.8	CSA – (Vahid Afroughsabet, 2019)
Poisson's Ratio [dimensionless]	0.186	Type I OPC – (Carmichael, 2009)
Shear Modulus [GPa]	19.4	Type I & Type III OPC – Calculated via $\left[G = \frac{E}{2(1+\nu)}\right]$
Mass Density $\left[\frac{kg}{m^3}\right]$	3150	Type III OPC – (Lehigh Technical Services, 2002)
Tensile Strength [MPa]	2.73722	Type III OPC – (Louis Schuman, 1943) (averaged)
Compressive Strength [MPa]	72.2	CSA – (Ioannou, Reig, Paine, & Quillin, 2014)
Thermal Expansion Coefficient $\left[\frac{1}{K}\right]$	4.5e-6, 0 - 300 C 7.7e-5, 300 – 600 C 1.04e-5, 600 – 800 C	Type III OPC – (Naus, 2010)

Thermal Conductivity $\left[\frac{W}{m*K}\right]$	0.97	CSA – (Huang, Pudasainee, Gupta, & Liu, 2021)
Specific Heat $\left[\frac{J}{kg*K}\right]$	750	CSA – (Winnefeld & Kaufmann, 2011)
Emissivity [dimensionless], wavelength dependent	0.85	CSA – (Khare, Bannerman, & Glasser, 2017)
Absorptivity $\left[\frac{1}{mm}\right]$, wavelength dependent	0.5	Unspecified concrete – (Kim, Youm, & Reda Taha, 2014)
Refractive index [dimensionless]	2.55	Unspecified concrete – (Sato, et al., 1996)

3. Test 3: MgO and Martian Regolith Simulant

Magnesium-based binders are similar in that magnesium oxide (“Magnesia”, MgO) reacts with water and another component. This other component is typically either magnesium oxysulfate or magnesium oxychloride. Magnesia is a relatively common binding agent that has many appealing properties for ISRU additive manufacturing. In the case of magnesium oxysulfate (“MOS”, MgSO₄), “the general properties of MOS binder include its relative lightweight, high-temperature resistance, excellent fire resistance and its low thermal conductivity” (Al-masaeid, 2019). Magnesium oxychloride (“MOC”, MgCO₃) is another magnesium-based binding agent with similar properties to magnesium oxysulfate. Investigations of magnesium-based binders, (Mo, Deng, Tang, & Al-Tabbaa, 2014) and (Walling & Provis, 2016), describe the structure and some properties of concrete using magnesium-based cement. The resulting microstructure is assumed to be denser on average than Type III OPC concrete. Granular boric acid set retardant was also added while mixing dry constituents. Boric acid is commonly used for extending the hydration period

of cement and aggregate before it has cured. However, boric acid (and boron compounds in general) in concrete has been studied previously (Davraz, 2014), and have documented negative effects on compressive strength. Table IV lists the material properties applied to the simulated experiment.

TABLE IV. JSC – MARS 1A MARTIAN REGOLITH SIMULANT + MAGNESIA CEMENT CONCRETE MATERIAL PROPERTIES

Property	Value	Type – Source
Elastic Modulus [GPa]	263.5	MgO, averaged – (Nobre, Hawreen, Bravo, Evangelista, & de Brito, Magnesia (MgO) Production and Characterization, and Its Influence on the Performance of Cementitious Materials: A Review, 2020)
Poisson’s Ratio [dimensionless]	0.36	MgO, averaged – (AZoNetwork UK, n.d.)
Shear Modulus [GPa]	107	MgO, averaged – (AZoNetwork UK, n.d.)
Mass Density $\left[\frac{kg}{m^3}\right]$	3560	MgO, averaged – (AZoNetwork UK, n.d.)
Tensile Strength [MPa]	96	MgO, averaged – (Nobre, Hawreen, Bravo, Evangelista, & de Brito, Magnesia (MgO) Production and Characterization, and Its Influence on the Performance of Cementitious Materials: A Review, 2020)
Compressive Strength [GPa]	1.135	MgO, averaged – (Nobre, Hawreen, Bravo, Evangelista, & de Brito, Magnesia (MgO) Production and Characterization, and Its Influence on the Performance of Cementitious Materials: A Review, 2020)
Thermal Expansion Coefficient $\left[\frac{1}{K}\right]$	10.5e-6	MgO, averaged – (AZoNetwork UK, n.d.)
Thermal Conductivity $\left[\frac{W}{m*K}\right]$	41.8679	MgO – (Nobre, Hawreen, Bravo, Evangelista, & de Brito, Magnesia (MgO) Production and Characterization, and Its Influence on the Performance of Cementitious Materials: A Review, 2020)
Specific Heat $\left[\frac{J}{kg*K}\right]$	955	MgO, averaged – (AZoNetwork UK, n.d.)

Emissivity [<i>dimensionless</i>], wavelength dependent	0.85	“Brown Concrete”, averaged – (Klein Tools, n.d.)
Absorptivity $\left[\frac{1}{mm}\right]$, wavelength dependent	0.5	Unspecified concrete – (Kim, Youm, & Reda Taha, 2014)
Refractive index [<i>dimensionless</i>]	2.55	Unspecified concrete – (Sato, et al., 1996)

4. Test 4: Lavacrete

Lavacrete is a proprietary material developed by ICON used to construct the Lunar PAD subscale lunar landing pad and was subsequently tested with an M-class solid rocket motor. Although it is unlikely that Lavacrete or other types of Earth-based concrete will be directly imported to the moon, this material serves as a point of comparison to the Lunar PAD test. Many of the properties of Lavacrete were provided directly from ICON. ICON has indicated that their Lavacrete is an “Ordinary Portland Cement-based mix” with “advanced additives”, and as a result, any other values not given by ICON were assumed to be similar to Type I Portland-cement based concrete. Table V lists the material properties applied to the simulated experiment.

TABLE V. LAVACRETE MATERIAL PROPERTIES

Property	Value	Type – Source
Elastic Modulus [<i>GPa</i>]	30.44	Lavacrete – (ICON)
Poisson’s Ratio [<i>dimensionless</i>]	0.18	Lavacrete – (ICON)
Shear Modulus [<i>GPa</i>]	12.89	Lavacrete – (ICON)
Mass Density $\left[\frac{kg}{m^3}\right]$	1900	Lavacrete – (ICON)
Tensile Strength [<i>MPa</i>]	2.44	Lavacrete – (ICON)
Compressive Strength [<i>MPa</i>]	41.36854	Lavacrete – (ICON)

Thermal Expansion Coefficient $\left[\frac{1}{K}\right]$	7.4e-13	Type I OPC – (Emmons & Vaysburd, 1995)
Thermal Conductivity $\left[\frac{W}{m*K}\right]$	1.1	Type I OPC – (Mounanga, Bastian, & Khelidj, 2018)
Specific Heat $\left[\frac{J}{kg*K}\right]$	1000	Type I OPC, averaged – (Ge, 2005)
Emissivity [<i>dimensionless</i>], wavelength dependent	0.9	“Rough Concrete”, averaged – (Klein Tools, n.d.)
Absorptivity $\left[\frac{1}{mm}\right]$, wavelength dependent	0.5	Unspecified concrete – (Kim, Youm, & Reda Taha, 2014)
Refractive index [<i>dimensionless</i>]	2.55	Unspecified concrete – (Sato, et al., 1996)

3. METHODOLOGY

A. Guidelines for Design of Experimentation

This thesis is divided into three distinct parts: the physical test, simulation, and data analysis. A summary of physical torch tests, simulations, and analyses performed on all materials can be found in Table I. The “physical test” consists of the using the propane torch on physical material samples and is described in III.F. The “simulation” is a digital recreation of the physical test, using CAD, CFD, and FEA software, and is described in III.G. The “data analysis” component of this experiment consists of using physical test data and simulation data to characterize and compare the temperature and strain response within the material, as described in III.H. Finally, the analysis component will comment on differences in physical test data and speculate on reasons for those differences.

Three types of data were collected from the physical propane torch experiment: temperature data via thermocouple, mass data via scale, and feature data via visual observation. A k-type thermocouple was used for measuring the center temperature of each sample. Because the maximum stagnation temperature of the propane torch was expected to reach up to ~ 2300 K, the high temperature limit of k-type thermocouple offers reassurance that the maximum temperature would not be exceeded when measuring the propane torch temperature or the internal cube sample temperature. The mass of each sample was measured via a scale to ± 0.45 grams (± 0.001 lbs.). Qualitative observations of changes in sample dimensions, color, cracks, erosion, and spalling were made with photos/video. Temperature, mass, and visual feature

data was collected before and after the test in an effort to assess the damage between two different states, in alignment with SHM Axiom II. Despite taking these measurements, we must also consider Axiom IVa as a limitation of instrumentation: “Sensors cannot measure damage. Feature extraction through signal processing and statistical classification is necessary to convert sensor data into damage information.”

Some testing conditions, such as the amount of time the propane torch is activated and the distance between the cube sample and propane torch, were determined based on the first physical experiment on the aluminum alloy sample. This preliminary test intended to check the distance that the propane torch could be held from the cube sample while the tip of the flame contacted the cube face, a condition that will be explained in more detail in the later sections.

Other testing conditions, such as the orientation of the cube sample, were pre-tested with simulations. All of these simulations used identical environmental and propane torch flame parameters, as described in detail in III.G. A preliminary simulation was created with the propane flame pointing horizontal “flame side” (pointing sideways), vertical “flame up” (pointing downward), and vertical “flame down” (pointing upward), while gravity was acting in the downward direction. A fourth simulation was created with no gravity to use as a comparison. For each orientation, the average temperature and heat flux data was measured from the cube face contacting the flame, shown in Figure 2a and 2b respectively.

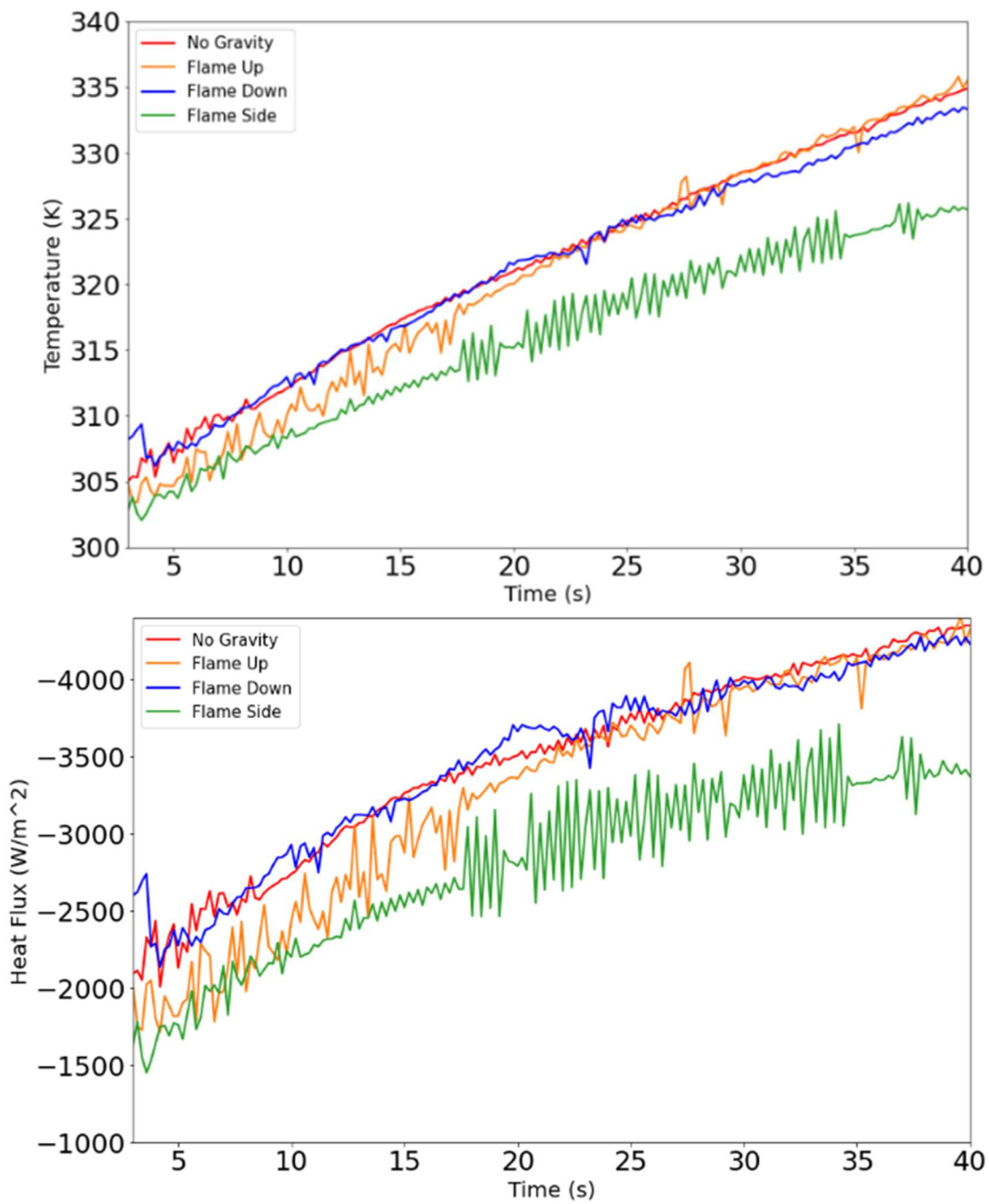


Figure 2a – 2b: Simulated pre-test average temperature (a) and heat flux (b) of the cube sample face in contact with the flame over time.

This orientation test simulation revealed that the flame down orientations was more similar to the no gravity condition than the flame side orientation. However, the flame up orientation had greater fluctuations in temperature and heat flux within the first ~17 seconds, while the flame side orientation had greater fluctuations after ~17 seconds. Average surface heat flux and temperature were the driving parameters to determine flame orientation. By identifying a flame orientation that would result in the most consistent and analogous temperature and heat flux values across the surface of the sample, we can more confidently assume a uniform heating profile. One resulting conclusion was that orienting the flame down would result in more consistent (lower oscillation) values for temperature and heat flux. The other conclusion was that the flame down orientation values would generally align with the no gravity condition, which is more similar to the 1/6 gravity conditions on the moon. The flame down orientation was ultimately selected.

B. Physical Experiment

The procedure of the physical experiment can be divided into four sections: the preparation of the concrete mixture for cube samples, the preparation of instrumentation, conducting the experiment, and compiling the results.

The preparation of each concrete sample followed identical procedures. The 6061-aluminum alloy sample followed different preparation procedures not discussed in this paper. The dry goods, such as cement, aggregate, additives, and fibers, were mixed in an ASTM-compliant 5-quart Humboldt mixer for approximately three minutes. Water was

gradually added and continued to be mixed for an additional five minutes until all components were thoroughly incorporated. ASTM C138 / C138M-17a describes the sample preparation procedure for cube samples used for this experiment. This procedure is typically used for compression testing, but the dimensions of the cube samples fit within the scope of this experiment and available material. While the material was mixing, the cube molds were sprayed with non-stick spray and excess liquid was drained. Once all components were thoroughly mixed, it was poured into the prepared cube molds up to approximately fifty percent of the mold. The material was tamped in two rounds (round 1 & 2 on Figure 3). The mold was overfilled with more of the concrete mixture and the excess material was removed from the top. The material was similarly tamped in the mold for another two rounds (round 3 & 4 on Figure 3). This process was repeated for all materials. Once all the samples were prepared, they were left to cure in excess of the minimum 28-day cure period.

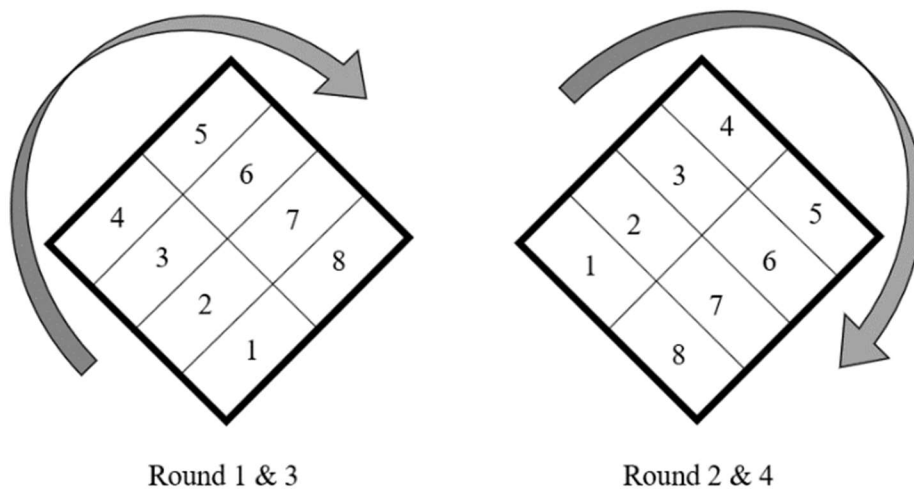


Figure 3: Cube sample tamping order, as per ASTM C138/C138M-17a.

Instrumentation was installed after all cube samples were fully cured. A small hole was drilled into each sample and the thermocouples were installed such that the sensing element was in the center of the cube volume, 2.54 cm (1 in) inward from every direction. Figure 4 shows the location and dimensions of the drilled hole and thermocouple. The thermocouples were anchored in the cube sample using Sauereisen Electrotemp Cement No. 8, a ceramic adhesive that had previously been used on the Lunar PAD project. This ceramic adhesive is “primarily used where high electrical insulation and thermal conductivity are desired” (Sauereisen, 2019). As a result, the ceramic adhesive was not considered for the simulated recreation of the experiment.

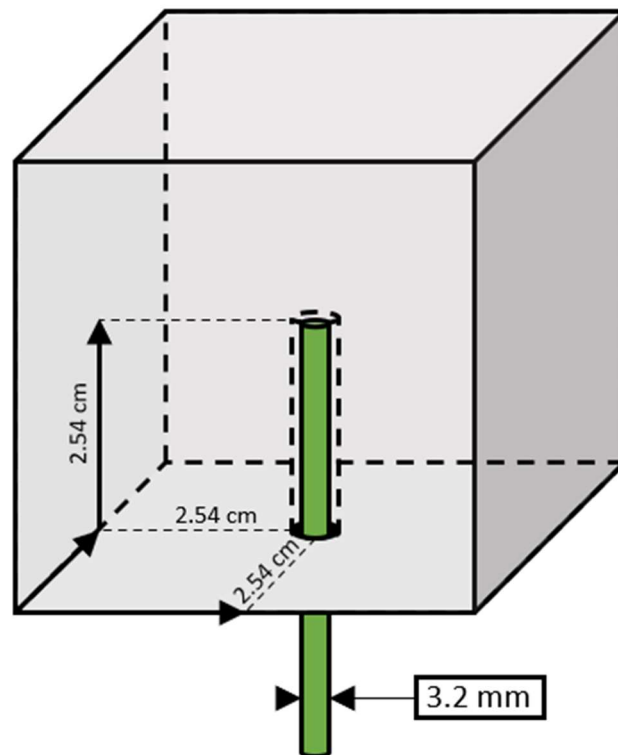


Figure 4: Thermocouple location diagram. Representative of thermocouple location for all material samples.

After the thermocouples were inserted into each material sample, the ceramic adhesive was left to cure for a minimum of 24 hours. The physical test setup could commence once the thermocouple was thoroughly bonded to the material sample. The general experiment setup, as shown in Figure 5 below, consists of using multiple ring stands and clamps to hold the propane torch such that the flame was upright, and the thermocouple was coming out of the top of the cube sample. A thin copper plate was placed underneath each sample as it sat on the ring stand to provide stability and support.

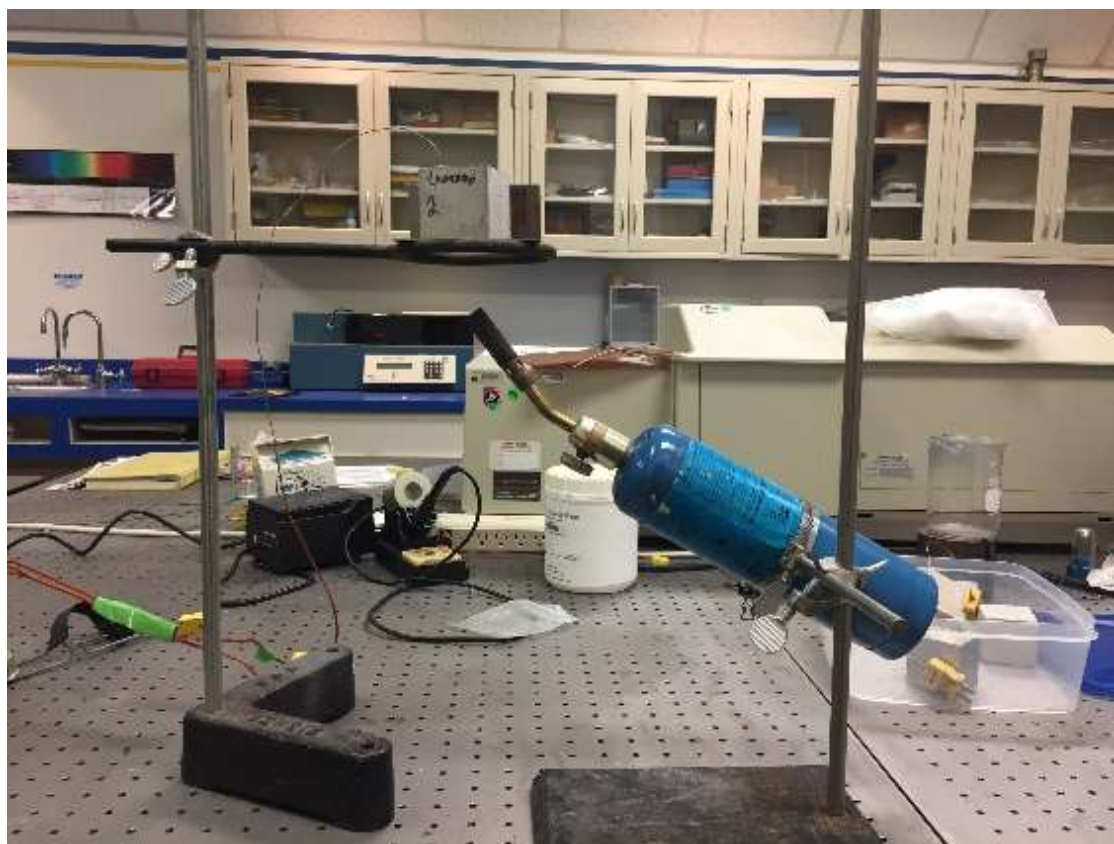


Figure 5: Physical experiment setup, including the propane torch, ring stand, copper plate, and cube sample. The propane torch was readjusted to be more vertical during actual testing.

Prior to igniting the propane torch flame and testing each sample, the time was recorded, and the timer would begin to count a minimum of five minutes before cutting off the supply of propane to the torch and extinguishing the flame. Occasionally during the tests, the angle or location of the propane torch was re-oriented such that blue flame tip was vertical and centered underneath the cube sample. The propane supply was also occasionally adjusted to shorten or extend the length of the blue flame such that the tip was contacting the copper plate. Figure 6a – 6b show the experiment in progress. The full step-by-step procedure is outlined on the next page.

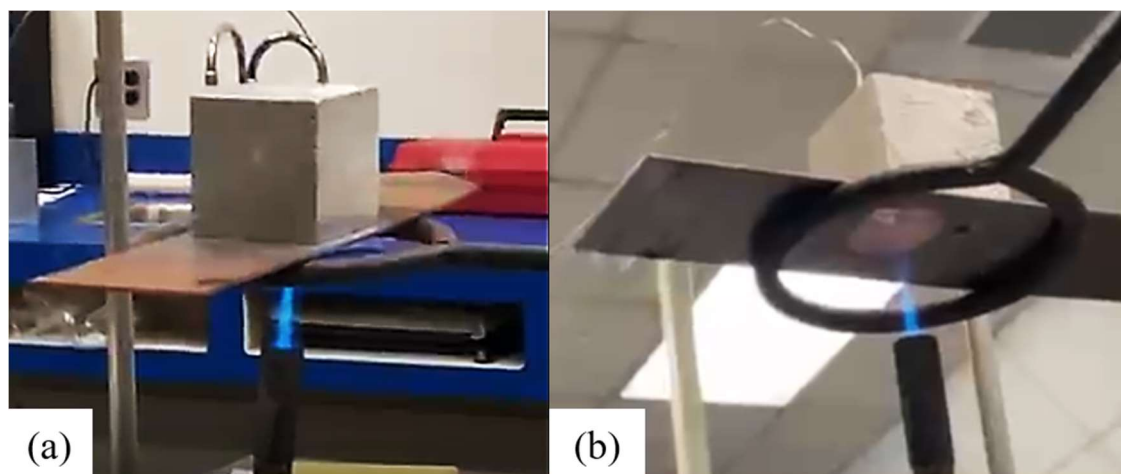


Figure 6a – 6b: Images from video footage captures during testing from above (a) and below (b)

Enhanced for clarity.

Physical Experiment method:

5. Prepare the concrete mixtures.
 - a. Mix aggregate and paste with 5-qt Humboldt mixer.
 - b. Continue mixing until the cubic molds are nearby, lubricated, and drained (2a – 2b).
6. Prepare the cube samples.
 - a. Wet the mold with lubricant spray.
 - b. Drain excess liquid from the mold.
 - c. Pour concrete into the mold to fill approximately 50%.
 - d. Tamping round 1 – 4.
 - e. Overfill the remainder of the mold.
 - f. Tamping round 1 – 4.
 - g. Slide the tamp across the top of the mold to remove excess material.
 - h. Wait 28 days until fully cured.
7. Prepare the instrumentation.
 - a. Test thermocouples before installation
 - b. Drill a 1-inch-deep hole into a face-center of each cube sample.
 - c. Prepare Sauereisen Electrotemp cement #8 “ceramic adhesive”
 - i. Mix 100 parts powder with 13 parts water
 - ii. Stir until thoroughly mixed
 - iii. Repeat as needed
 - d. Pour ceramic adhesive into drilled hole
 - e. Insert thermocouple into drilled hole
 - f. Wait 24 hours until fully cured
 - g. Test thermocouples after installation
8. Conduct experiment
 - a. Measure initial parameters
 - b. Ignite the propane torch
 - c. Expose the cube sample to propane torch flame
 - i. Orient the propane flame upwards towards the cube sample and perpendicular to the cube sample face
 - ii. Maintain a distance from nozzle of the propane torch to the cube sample face such that the tip of the blue flame is contacting the material
 - iii. Maintain exposure for 360 seconds (6 minutes)
 - d. Extinguish the propane torch
 - e. Measure final parameters
 - f. Repeat 4a – 4e for all samples
9. Compile results
 - a. Export data to Excel

C. Simulated Experiment

The physical experiment explained in the previous section was recreated in SolidWorks CAD in order to simulate the same conditions in the SolidWorks Simulation (FEA) and Flow Simulation (CFD) software packages. Four categories are vital to recreating the physical test as closely as possible: CAD models, environmental parameters, propane torch flame parameters, and simulation setup parameters.

1. CAD Models

The cube sample CAD model had the same 2-inch cube dimensions as the test samples that were created, and their material properties, as described above, are applied respectively. A propane torch CAD model identical to the propane torch used for the experiment was found on grabcad.com and imported into an assembly. The copper plate underneath the cube sample was 0.15875 cm (1/16 inch) thick. The mechanical and thermal properties of the copper plate were assumed to be equal to the pre-defined “copper” material in SolidWorks and values are shown in Table VI. The ring stand material was assumed to be grey cast iron, and its material properties are irrelevant to this work as there was no or minimal heat transfer to and from the ring stand. The cube sample, copper plate, and ring stand are shown in Figure 7a and Figure 7b in isometric and side view respectively.

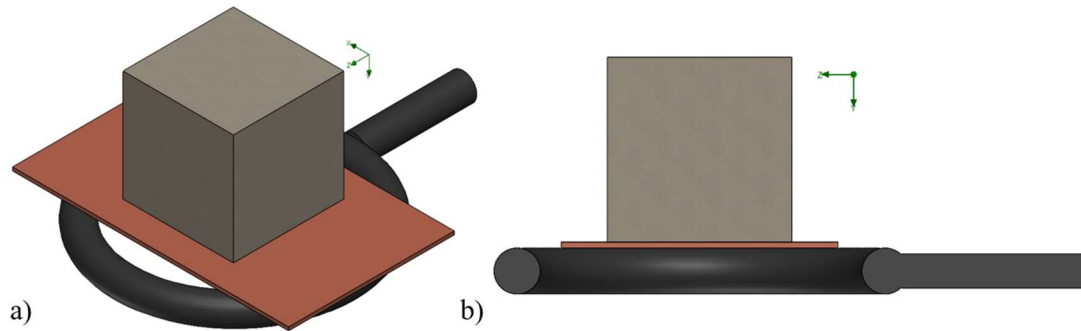


Figure 7a – 7b: Isometric (a) and side (b) views of the cube sample, copper plate, and ring stand CAD models. The side view is cut in half to show the contact between each part.

TABLE VI. COPPER PLATE MATERIAL PROPERTIES

Property	Value	Type - Source
Elastic Modulus [GPa]	110	Copper – SolidWorks pre-defined material
Poisson's Ratio [dimensionless]	0.37	Copper – SolidWorks pre-defined material
Shear Modulus [GPa]	40	Copper – SolidWorks pre-defined material
Mass Density $\left[\frac{kg}{m^3}\right]$	8900	Copper – SolidWorks pre-defined material
Tensile Strength [GPa]	0.39438	Copper – SolidWorks pre-defined material
Thermal Expansion Coefficient $\left[\frac{1}{K}\right]$	2.4 e-05	Copper – SolidWorks pre-defined material
Thermal Conductivity $\left[\frac{W}{m*K}\right]$	390	Copper – SolidWorks pre-defined material
Specific Heat $\left[\frac{J}{kg*K}\right]$	390	Copper – SolidWorks pre-defined material
Emissivity [dimensionless]	0.125	Roughened Copper, averaged - (Fluke Process Instruments, 2022)

2. CFD Environmental Parameters

Alignment between the physically tested and simulated experiments requires an accurate recreation of the environmental conditions at the time of testing. The environmental conditions shown in Table VII use a combination of assumed and measured values. Although trace amounts of moisture were likely found in the air, the experiment was conducted indoors, and humidity was thus considered to be negligible. The ambient atmospheric pressure was not measured directly at the time of testing, but the US National Weather Service provides barometric pressure measurements for Huntsville, Alabama that were used. The ambient temperature was measured directly at MSFC at the time of testing using identical thermocouples to those used for the material samples. These environmental parameters were used for all simulations described in this thesis, including individual simulations, such as the propane torch orientation simulation and the propane torch profile simulation described later in this section.

TABLE VII. ENVIRONMENTAL PARAMETERS

Parameter	Value	Source
Ambient Fluid	100% dry air	Assumed
Ambient pressure [Pa]	101964.16	Measured indirectly (National Weather Service, 2021)
Ambient temperature [K]	294.15	Measured directly
Gravitational Acceleration [$\frac{m}{s^2}$]	9.81	Assumed

3. CFD Propane Torch Flame Parameters

Liquefied petroleum gas (LPG), or propane, is a flammable, hydrocarbon fuel gas. Propane is a well-understood gas, as it is used in many applications. Table VIII shows the propane torch flame parameters used for all simulations, including the pretest simulation used to determine the most appropriate flame orientation. The flow rate shown in the table was assumed constant throughout the simulation, but it should be noted that the actual flow rate fluctuated slightly as there were several instances of the flow valve being adjusted so the flame tip contacted the copper plate. The inlet velocity and stagnation temperature values found in other sources used a propane torch with similar dimensions. In the simulation, the flow started after 0.5 seconds, in order to collect data for the ambient room and material conditions.

TABLE VIII. PROPANE TORCH FLAME PARAMETERS

Parameter	Value	Source
Flow inlet area [m^2]	4.887e-5	Measured via CAD model
Inlet velocity [$\frac{m}{s}$]	9.92093e-5	(Devadiga & Rao, 2013)
Stagnation pressure [Pa]	206843	Given via manufacturer (30 psi regulator)
Stagnation temperature [K]	2253	(Elgas, 2021)

The propane torch parameters shown in Table VIII above were used for an independent torch flame simulation to confirm that the flame profile and blue flame tip temperature were similar. This independent simulation used the same environmental conditions, propane torch flame conditions, and propane torch nozzle dimensions as those used in other simulations, which are assumed to be similar to the physical test. Figure 8a shows the propane torch CAD model used for all simulations, and Figure 8b highlights the origin of the flow source.

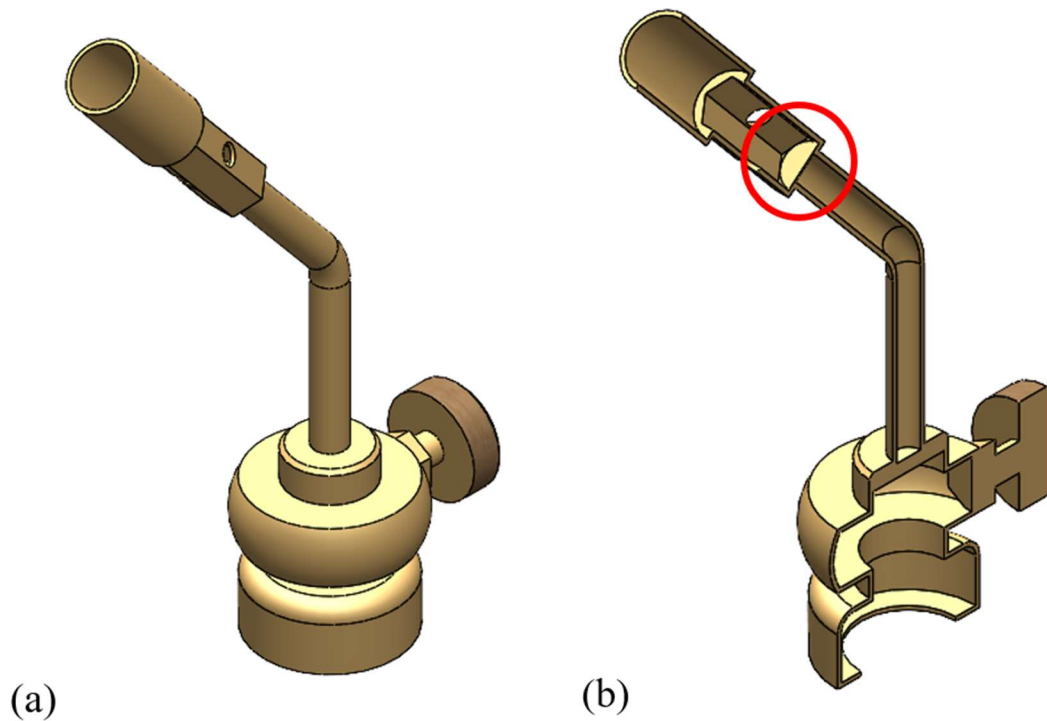


Figure 8a – 8b: The CAD model of the propane torch nozzle used for all simulations shown in an isometric view (a) and a cross-section isometric view (b). Red circle indicates the surface to which the propane torch flame parameters were applied.

The length of the blue flame is an important metric, as a blue flame is indicative of the complete combustion of carbon atoms in the propane hydrocarbon fuel source. Furthermore, the blue flame tip temperature was measured directly and serves as a point of comparison between the simulated and physical torch flame. Prior to the physical testing of each material sample, the propane torch was ignited and the temperature at the tip of the blue flame was measured to be 1018 K by the same k-type thermocouples used for the material samples. A simulated sensor probe was similarly placed, and sketch lines were drawn from the center of the torch nozzle tip to the farthest point where $T = 1018$ K, the measured blue flame tip temperature. The length from the torch nozzle to the tip of the blue flame shown on the sketch line in the simulation will serve as a reference metric for the distance between the torch nozzle and the cube sample face. The length of the sketch line was 7.863 cm and is assumed to be equal to the length of the simulated blue flame and the distance between the torch nozzle and cube sample in the physical test. Although it is likely that the position of the physical propane torch was slightly different than the simulation, this metric would minimally ensure that the sample is being exposed to the same 1018 K temperature.

Figure 8a shows the results of a torch flame simulation using parameters in Table VIII. This flame profile was then compared with CFD simulation work found in literature, shown in Figure 9b (ISSI, 2013). The temperature region most similar to the measured 1018 K is indicated with the cyan-green boundary (1100 K). The distance between the flame base and the tip of the cyan-green boundary is approximately 11cm, which is a difference of

33% when compared to my independent simulation. However, comparing these flames based on the ratio of width to length may account for differences in nozzle geometry. The ratios of width to length of the Figure 8a and 8b simulations is approximately 0.141 and 0.136, respectively. These ratios only have a difference of 3%, which demonstrates that the profile of the simulated propane torch flame in this thesis is acceptable and in agreement with other research and simulations.

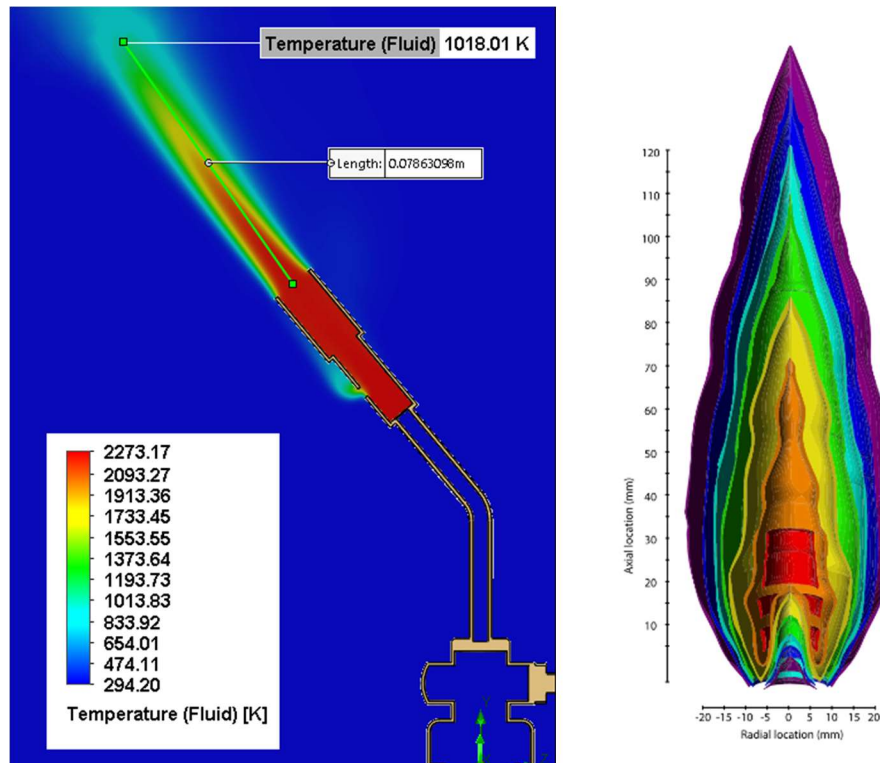


Figure 9a – 9b: Cross-section view of the independent propane torch flame simulation (a) and a similar propane torch simulation found in literature (b). The Figure 9a labeled fluid temperature of 1018.01 K is assumed to be the tip of the blue flame and is labeled sensor as 7.863 cm long. The Figure 9b colors are representative of temperature, where; 1,750 K > Red, 1,700 K > Orange, 1,600 K > Yellow, 1,350 K > Green 1,100 K > Cyan, 875 K > Blue, 750 K > Purple.

4. CFD Simulation Setup Parameters

A simulation mesh uses the previously mentioned fluid dynamics equations to calculate mass, volume, energy transfer between each cell. Increasing the number of smaller cells also increases the number of these calculations being performed, and thus increases the resolution and accuracy of the simulation. The computational domain was a two-meter cube, with the cube sample in the center. A coarse global mesh was applied to the entire computational domain and finer local meshes were created around two points of interest: the propane torch nozzle, and the volume within and around the cube sample. This combination of global and local meshes will reduce overall computation time and increase calculation resolution in relevant areas.

The torch local mesh is centered on the propane torch and focuses on setting a high fluid region refinement level. Higher fluid refinement levels increase the number of cells within a fluid volume. The cube local mesh is centered on the cube sample and focuses on setting a high solid refinement levels. Higher resolution in the cube mesh results in more accurate solid temperature data, which is then exported into the FEA simulation discussed in a later section. The mesh refinements for the global, torch, and cube meshes are detailed in Table IX.

TABLE IX. SIMULATION MESH PARAMETERS

Global Mesh Parameters	
Parameter	Value
Fluid cell refinement level	0
Solid cell refinement level	0
Fluid – Solid boundary refinement level	0
Torch Mesh Parameters	
Parameter	Value
Fluid cell refinement level	6
Solid cell refinement level	0
Fluid – Solid boundary refinement level	3
Cube Mesh Parameters	
Parameter	Value
Fluid cell refinement level	2
Solid cell refinement level	4
Fluid – Solid boundary refinement level	2

Figure 10a shows the volume containing the torch local mesh while Figures 10b and 10c show the cube local mesh from two perspectives. Each of these local meshes correspond to the parameters set in Table IX.

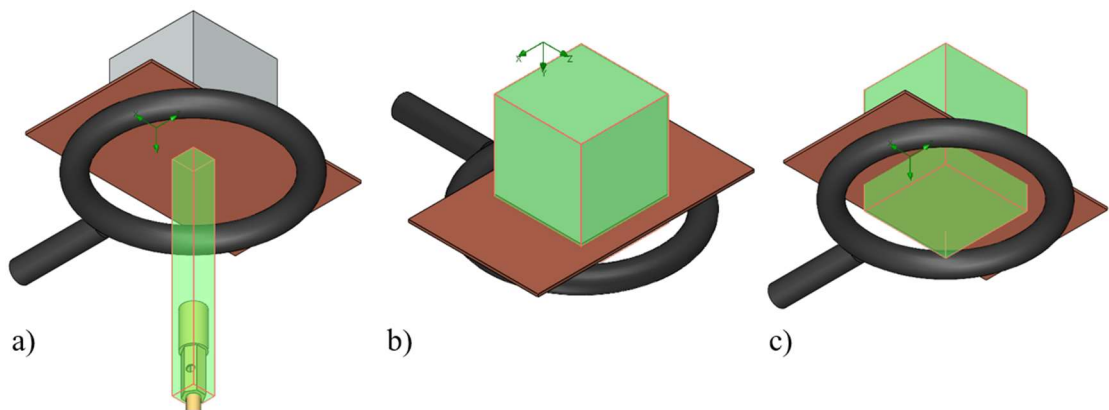


Figure 10a – 10c: Torch local mesh applied to the torch nozzle and the space between the torch and copper plate (a) as well as the cube local mesh applied to the cube sample and some of the area between the cube and torch from above (b) and below (c).

Finally, Figure 11 shows a cross-section with a cut plot of the mesh density. The cell colors shown in Figure 11 correspond to the average approximate cell length shown in Table X. These mesh parameters were applied to all simulations.

TABLE X. SIMULATION MESH DIMENSIONS

Cell color	Approximate cell length [cm]
Dark blue	4
Light blue	2
Green	1
Yellow	0.5
Red	0.125

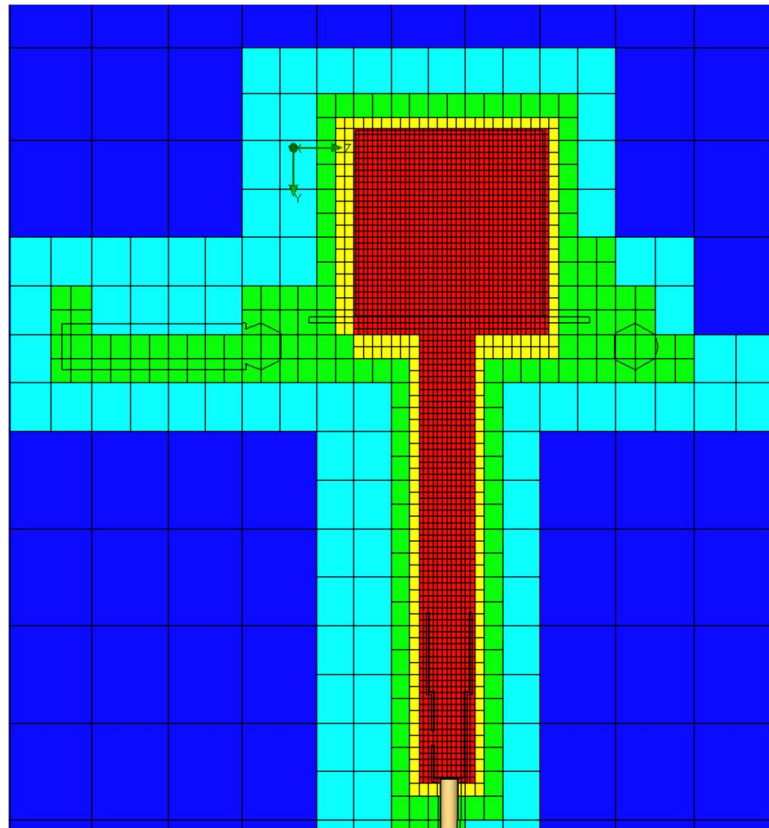


Figure 11: Side view of the assembly with a cut plot of mesh density. Red represents the smallest cells while blue represents the largest cells.

Calculation control options provide additional levels of control for simulation finishing conditions, adaptive refinement, solving, and results saving. The use of additional SolidWorks simulation features in this thesis, such as time-dependence, open more options for control to be defined. All modes of heat transfer were simulated for each material, which also allowed for the input of emissivity and other thermal material properties listed in previous sections. The following calculation control options were applied to all simulations.

The finishing conditions for this simulation focused on simulated time and completing all mesh refinements. The amount of “simulated time” each cube sample was exposed to the propane torch varied between tests but followed the same rule of adding a minimum of 30 seconds to the physical test time. For example, the aluminum 6061 alloy sample was tested for approximately 400 seconds, so the simulation ran for 430 seconds, the CSA + Lunar Regolith Simulant sample was physically tested for 420 seconds and simulated for 450 seconds, and similarly for the remaining samples. This additional 30 seconds of simulated time would ensure that enough data would be collected to compare with the physical sensor data while minimizing computation time and memory allocation. A time step of 0.1 seconds was selected to match the thermocouple data sampling rate. The other finishing condition of completing all mesh requirements was selected because of the number of refinements in this simulation. Satisfying this finishing condition requires that all initial mesh refinements are generated, as well as the mesh refinements discussed above. These options are summarized in Table XI.

TABLE XI. CFD SIMULATION CALCULATION CONTROL OPTIONS

Parameter	Value
Physical time [s]	[physical test time] + 30 seconds
Time step [s]	0.01
Refinements	Global, Torch, Cube

5. FEA Simulation Parameters

In order to simulate the internal strain response of the material from the thermal load of the propane torch, SolidWorks' FEA simulation add-on was used in tandem with CFD simulations. The most important parameters to be defined in setting up the FEA simulation are the mesh, fixtures, and loads. Much like the CFD simulation setup that was just described, the FEA simulation is capable of various types of mesh customization. The focus of this mesh setup was to increase the accuracy and resolution of the mesh within the cube sample. As a result, a finer mesh (~2mm) was generated for the cube sample while a coarser mesh (~6mm) was generated for the ring stand and copper plate. For all FEA simulations, it is required that fixtures are properly defined in order to constrain the stress, strain, and displacement generated from loads. In this case, we are most interested in seeing the strain within the cube sample. As a result, we cannot apply fixtures to the cube sample itself, as that would prevent any type of displacement and generate inaccurate results. Instead, the fixtures were applied to the top of the copper plate contacting the cube and to the ring stand. This would allow the cube sample to react to thermal loads and ignore displacement results seen in the copper plate and ring stand, however small. In addition to simulating static, fatigue, and thermal loading scenarios independently, the SolidWorks FEA software is capable of importing loading conditions from a SolidWorks CFD simulation. Gravitational

loads were not included in these simulations in order to measure the strain resulting from isolated thermal loads. Unlike CFD simulations, the FEA software is incapable of simulating a transient scenario where results can be calculated and compiled over time. Instead, the FEA software requires individual simulations for each time moment. In order to capture the transient aspect of this experiment, two FEA simulations were run for each material. The first simulation uses CFD results at $t = 120$ seconds about mid-way through the simulation where all cube sample center temperature began rising. The second simulation uses CFD results at $t = 300$ seconds, considered the end of the experiment. All of these parameters are summarized in Table XII. Figure 12 also shows the mesh and fixtures applied to all FEA simulations.

TABLE XII. FEA SIMULATION PARAMETERS

Parameter	Value
Cube Mesh Element Size [<i>mm</i>]	4 ± 2
Fixtures	Copper Plate, Ring Stand
Loads	Imported from CFD simulations at: $t = 120$ seconds $t = 300$ seconds

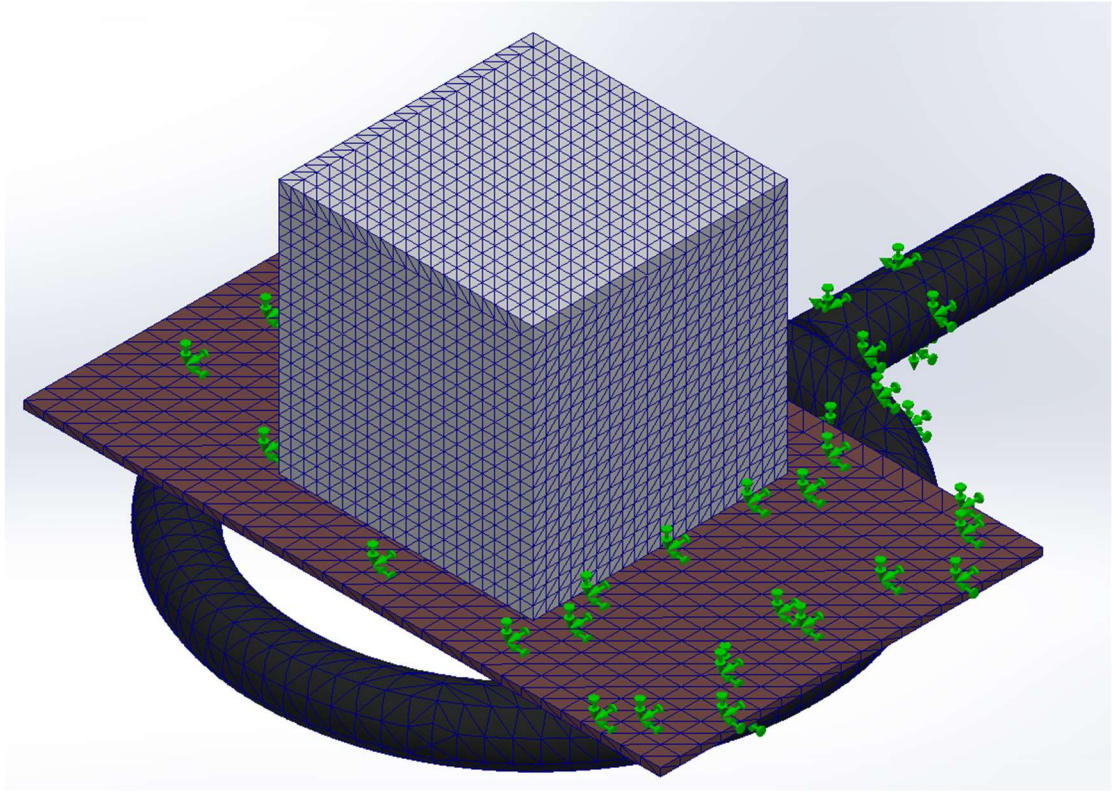


Figure 12: FEA Simulation mesh and fixtures applied to all simulations.

D. Data Analysis and Calculation

The data analysis component of this thesis is based on several SHM Axioms. For example, SHM Axiom IVa explains “Feature extraction through signal processing and statistical classification is necessary to convert sensor data into damage information”, with sensor data being the mass, dimensions/features, and temperature measured before, after, and during the test. Upon the collection of physical and simulated sensor data using the methods described above, the main statistical method to compare this data was the Pearson Correlation Coefficient (PCC). Additional details and outcomes of using the PCC are described in the Chapter 5. Figure 13 shows the high-level data analysis process for the

simulated and physical experiment. The simulated experiment provides an abundance of data in the form of sensors, goals, and various plots. III.H.1 describes the process that will use this simulation data to calculate the temperature gradient within the material. Because the only measured temperature value in the physical experiment was from the thermocouple embedded in the cube sample, the temperature of the surface of the cube sample is inferred from simulation. III.H.2 similarly describes the process of calculating the temperature gradient using the combination of simulated and physical sensor data. Finally, the temperature gradient of the simulated and physical experiments will be compared to the simulated strain gradient for a qualitative analysis in the Chapter 5.

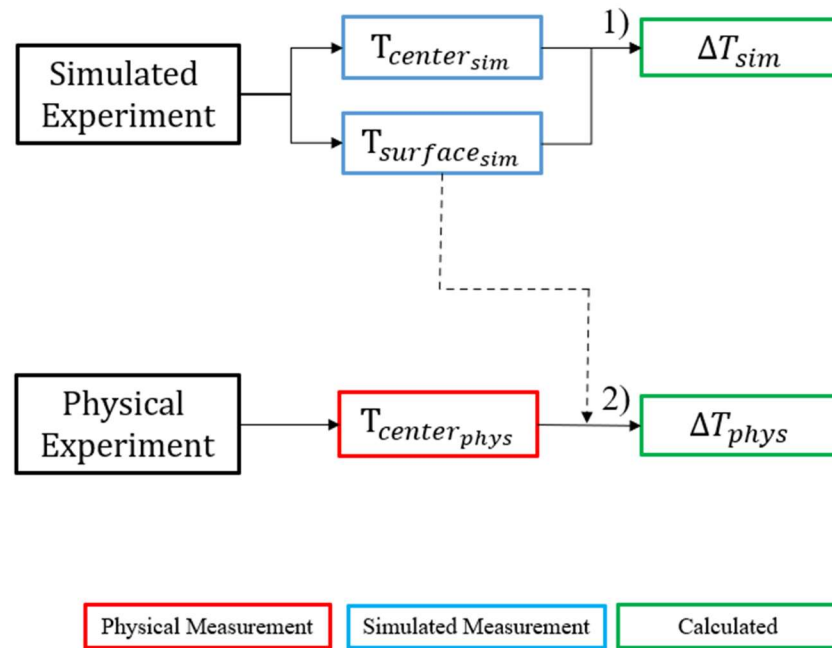


Figure 13: Data analysis process diagram. Red boxes indicate directly measured values from the physical experiment. Blue boxes indicate directly measured values from the simulation. Green boxes indicate calculated values based on measured values.

1. Simulated Temperature Gradient Calculation

The expected simulated and experimental temperature measured from the center of the cube sample can be calculated using several heat transfer equations. The source of the heat coming from the propane torch means convective and radiative modes of heat transfer are occurring, with conductive heat transfer occurring from the surface to the center of the cube sample. The primary mode of heat transfer in this experiment is conduction through the cube sample from the torch flame face to the center of the cube. The 1-D heat flux by conduction, \dot{q}_{cnd} is described by the Equation 1 where k is the thermal conductivity of the material, and $\frac{dT}{dx}$ is the temperature gradient over the length or depth of the material. These values are visually represented in Figure 14.

$$\dot{q}_{cnd} = -k \frac{dT}{dx} \approx -k (T_{surface_{sim}} - T_{center_{sim}}) \quad (1)$$

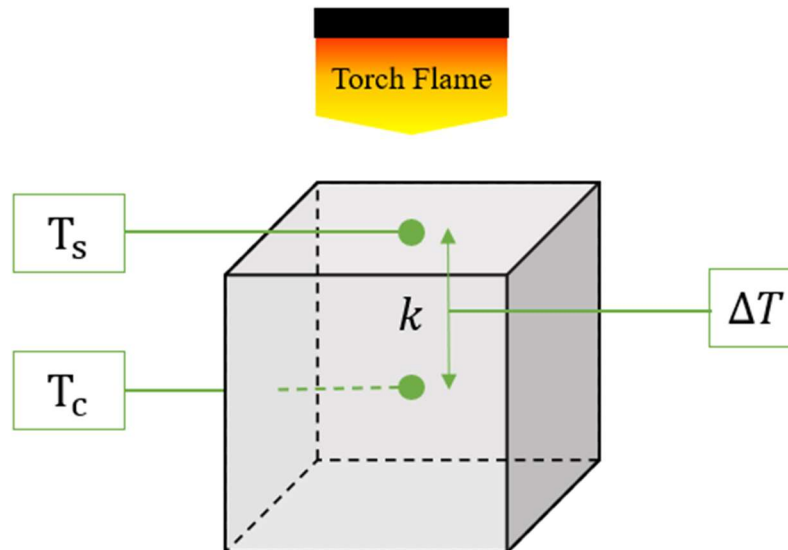


Figure 14: The variables of heat transfer by convection. The orientation of this diagram does not represent the orientation of the sample and torch flame during experimentation and simulation.

2. *Experimental Temperature Gradient Calculation*

The calculation of the experimental temperature gradient follows a similar process as the calculation of the simulated temperature gradient, described in III.H.1 above. However, the temperature of the surface of the cube sample was not measured during the physical experiment. As a result, the simulated surface temperature will be used for these calculations instead. The other modes of heat transfer, convection and radiation were also unmeasured and will not be calculated. The equation for conductive heat transfer is shown again in Equation 2 below, but with the cube sample center temperature measured by the thermocouple ($T_{cente\ phys}$) instead of the simulated sensor variable ($T_{cent\ sim}$).

$$\dot{q}_{cnd} = -k \frac{dT}{dx} \approx -k \left(T_{surface_{sim}} - T_{cente\ phys} \right) \quad (2)$$

4. RESULTS

This chapter will present and briefly summarize results, and the following chapter will discuss them in further detail. The results shown will follow a generally similar order to that shown in the Chapter 3, starting with the simulation and then the physical experiment. In each of the following sections, a shortened name is given to each test for brevity in tables and figures, as shown in Table XIII.

TABLE XIII. TEST SAMPLE SHORT NAMES AND ABBREVIATED NAMES

	Test 1	Test 2	Test 3	Test 4
Short name	Aluminum 6061 Alloy	CSA + Lunar Regolith Simulant	MgO + Mars Regolith Simulant	Lavacrete
Abbreviated name	AL	CSA	MGO	LAVA

Due to the transient nature of this experiment, images and data were collected at regular intervals and are labeled with the time elapsed from the beginning of the experiment (e.g., $t = 60$ seconds). Every data table in the following sections will minimally include “final” values taken at $t = 300$ seconds. Although some of the physical tests ran longer than 300 seconds, this was largest value that at least all tests were run. Data from the simulated and physical experiments were compiled in various plots and generated using Google Co-lab, a python-based compiler that allows for seamless module integration and data importing from a local Google Drive.

A. CFD Simulation Results

1. Simulated Images

Each of the simulated experiment images shown in this section were taken from the SolidWorks Flow Simulation cut plot and surface plot features. Each plot will use similar isometric and side perspectives to demonstrate the CAD model setup in Figures 7a – 7b in the Chapter 3. All figures also include a probe that display the temperature at the center of the cube sample and at the surface of the cube sample, contacting the copper plate.

The aluminum 6061 alloy sample had the highest thermal conductivity of any of the samples tested, and thus the temperature difference between the surface and center was expected to be lower than other samples. This caused a very narrow range between the coldest to hottest temperatures. Therefore, the color scale for temperature values had to be changed for all AL figures to maintain a gradient visual representation of temperature. Figure 15a of the $t = 10$ seconds time moment shows a 2 K difference between the lowest value (blue = 303 K) and highest value (red = 305 K) on the plot while Figure 15b of the $t = 60$ seconds time moment shows a similarly small 1.5 K difference, but the range is significantly higher overall (334.5 K – 336 K).

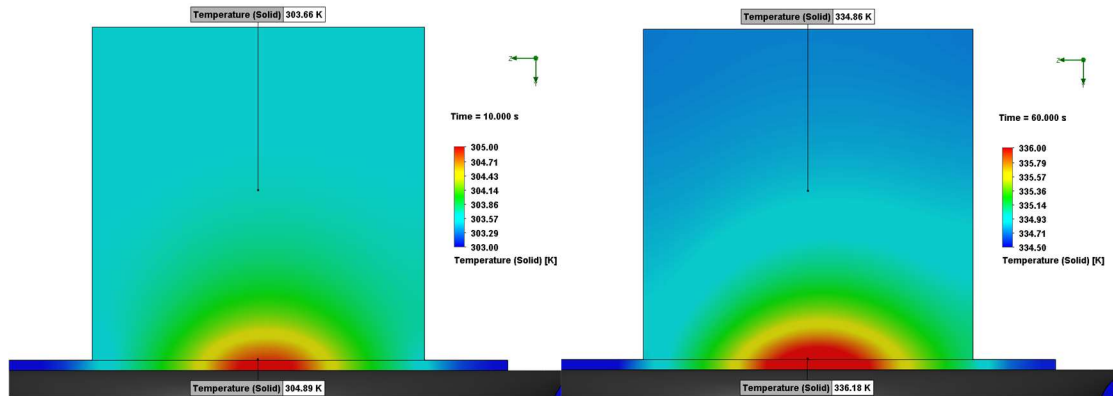


Figure 15a – 15b: Temperature cut plot of the AL sample at $t = 10$ seconds (14a) and $t = 60$ seconds (14b). Note the significantly changed values of the color scale for temperature.

Once again, Figures 16a – 16b show the temperature gradient with a 1.5 K range. The maximum value of the range increases from 336 K at $t = 60$ seconds, to 356 K at $t = 120$ seconds, and 370 K at $t = 180$ seconds. The average temperature is steadily increasing by approximately 20 K per 60 seconds.

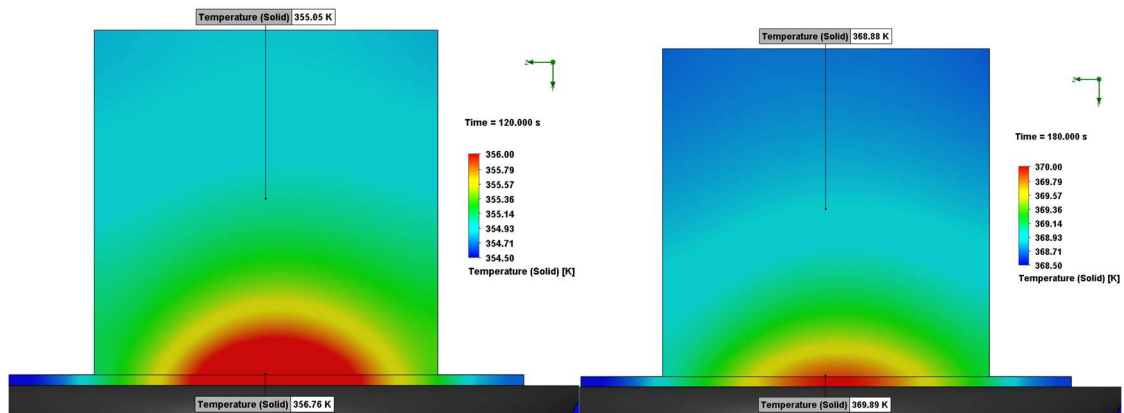


Figure 16a – 16b: Temperature cut plot of the AL sample at $t = 120$ seconds (16a) and $t = 180$ seconds (16b). Note the significantly changed values of the color scale for temperature.

The last two time moment intervals are shown in Figure 17a – 17b. The color scale remains very narrow, at 1.5 K. At this point, the color range is only increasing by 10 K.

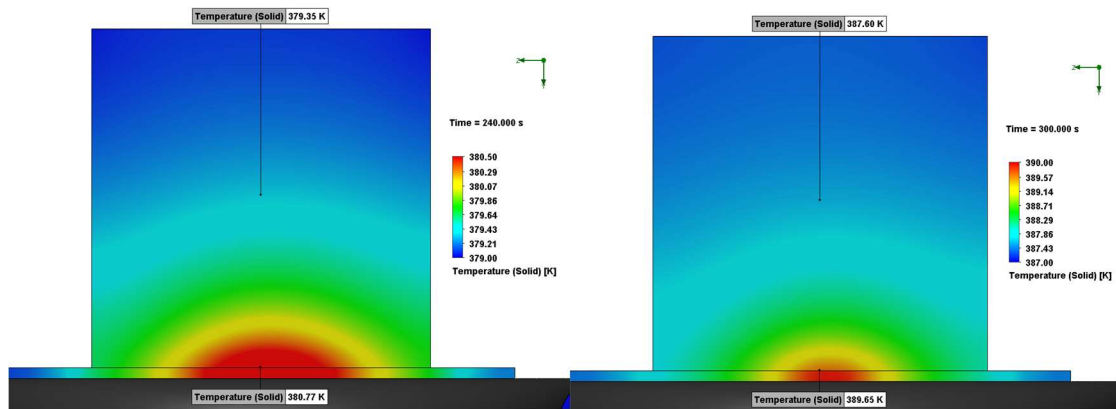


Figure 17a – 17b: Temperature cut plot of the AL sample at $t = 240$ seconds (17a) and $t = 300$ seconds (17b). Note the significantly changed values of the color scale for temperature.

The CSA + Lunar Regolith Simulant sample, on the other hand, had the lowest thermal conductivity, and thus the temperature difference between the surface and center was expected to be higher than all other samples. Although the temperature increase was higher than expected, the change was gradual enough to use the same value color scale (293.15 K – 300 K) for all images. Figure 18a – 18b show the CSA sample solid temperature between $t = 10$ seconds and $t = 60$ seconds. At this point, the center temperature is unchanged, and heat is still being transferred through the first third of the material.

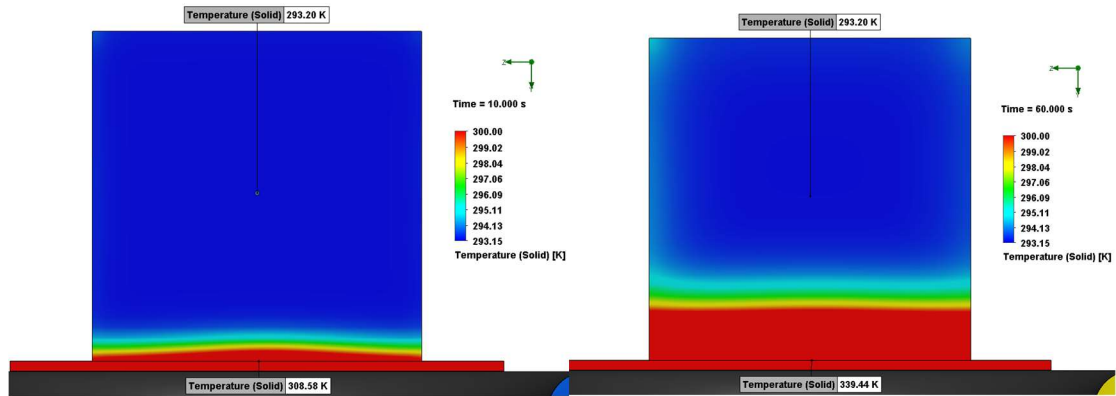


Figure 18a – 18b: Temperature cut plot of the CSA sample at $t = 10$ seconds (18a) and $t = 60$ seconds (18b). All CSA figures use the same value color scale to represent temperature.

Figures 19a - 19b show the $t = 120$ seconds and $t = 180$ seconds time moments. In these figures, it becomes clear that there is asymmetrical heating in the top corners of the sample. The rate of the temperature increase within the material appears to be somewhat consistent between each 60 second interval.

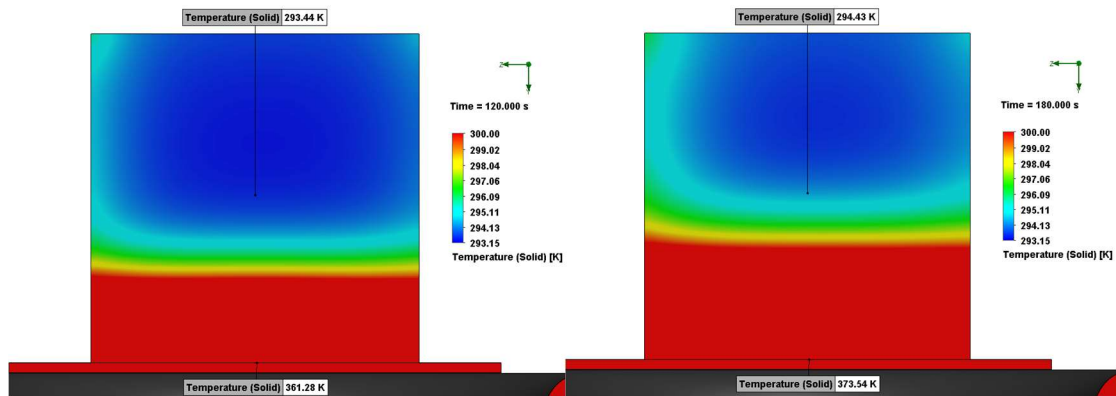


Figure 19a – 19b: Temperature cut plot of the CSA sample at $t = 120$ seconds (19a) and $t = 180$ seconds (19b). All CSA figures use the same value color scale to represent temperature.

Finally, Figures 20a – 20b show the 240 second and 300 second time moments. In these figures, the center temperature is experiencing a more significant change and a majority of the sample has experienced some amount of temperature increase. The asymmetrical heating continues and biases towards the left.

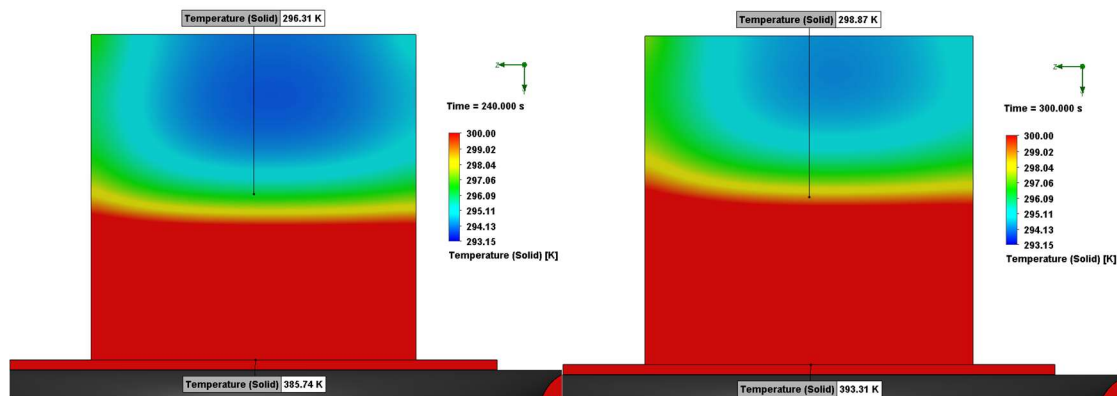


Figure 20a – 20d: Temperature cut plot of the CSA sample at $t = 240$ seconds (20a) and $t = 300$ seconds (20b). All CSA figures use the same value color scale to represent temperature.

Of the concrete samples, the MgO + Martian Regolith Simulant sample had the most significant and rapid temperature change. Despite this, all of the MgO figures below still use the same color value scale (293.15 K – 330 K). By using the same color scale, it also becomes more apparent that the entire cube sample is heating more rapidly rather than the slower temperature creep seen in the CSA and Lavacrete samples. Figure 21a and 21b show the first two time moments for the MGO sample, and unlike the other concrete samples, the temperature noticeably changes within 60 seconds.

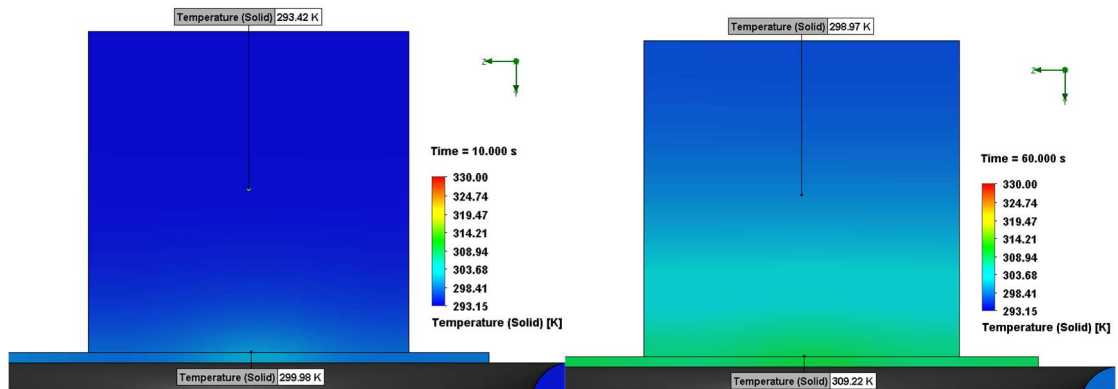


Figure 21a – 21b: Temperature cut plot of the MGO sample at $t = 10$ seconds (21a) and $t = 60$ seconds (21b). All MGO figures use the same value color scale to represent temperature.

Figure 22a and 22b show the continuing trend of almost uniform heating throughout the cube sample. At this point in the simulation, other concrete samples also saw some asymmetrical heating that was not seen in the MGO sample.

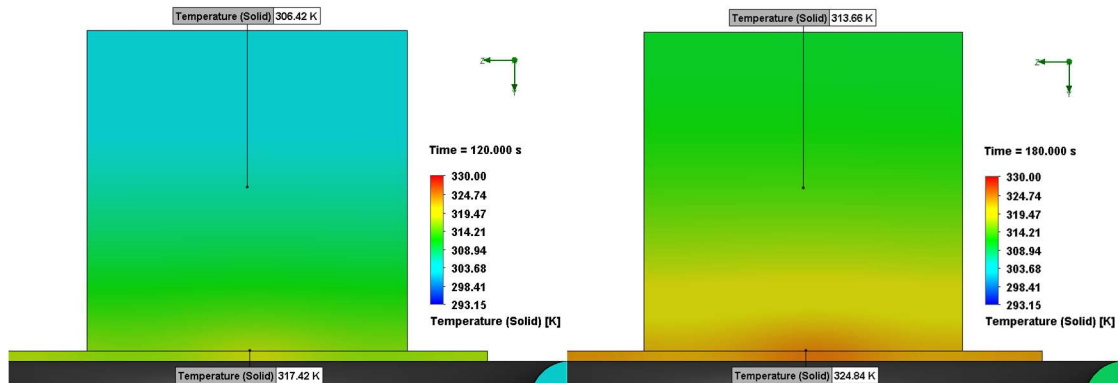


Figure 22a – 22b: Temperature cut plot of the MGO sample at $t = 120$ seconds (22a) and $t = 180$ seconds (22b). All MGO figures use the same value color scale to represent temperature.

Finally, Figure 23a and 23b show the last two time moments of the MGO sample. Once again, the heating profile remains somewhat uniform, and the center of the cube sample increases in temperature by about 7 K.

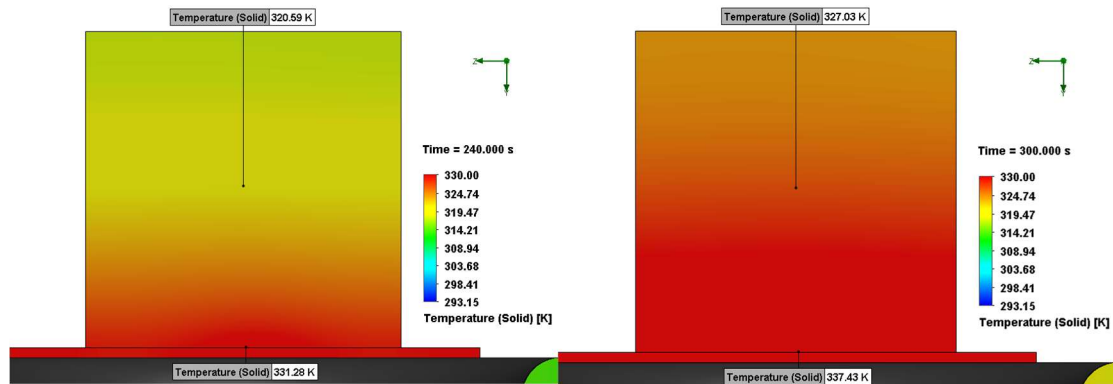


Figure 23a – 23b: Temperature cut plot of the MGO concrete sample at $t = 240$ seconds (23a) and $t = 300$ seconds (23b). All MGO figures use the same value color scale to represent temperature.

The simulated Lavacrete sample experienced a small enough overall temperature change such that all LAVA figures use the same color scale. Much like other concrete samples, the temperature change was much more gradual than the aluminum 6061 alloy sample. Figure 24a and 24b show the solid temperature of the profile, and the rate of change initially appears more similar to the CSA sample than the MGO sample.

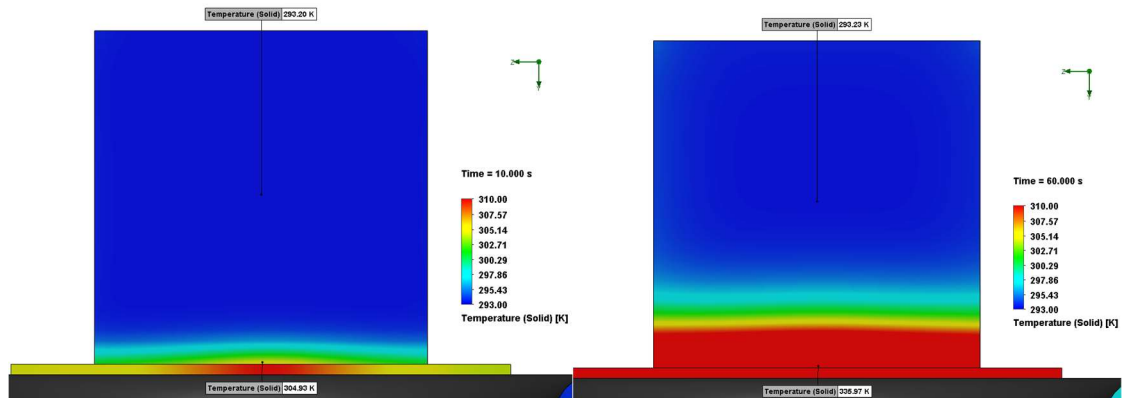


Figure 24a – 24b: Temperature cut plot of the Lavacrete concrete sample at $t = 10$ seconds (24a) and $t = 60$ seconds (24b). All Lavacrete figures use the same value color scale to represent temperature.

Figures 25a - 25b show the $t = 120$ second and $t = 180$ second time moments. At this point, the heating profile becomes somewhat parallel with the bottom face of the cube. However, there slight asymmetrical heating becomes apparent on one side of the sample, and the effects of this asymmetry will propagate in the next set of figures.

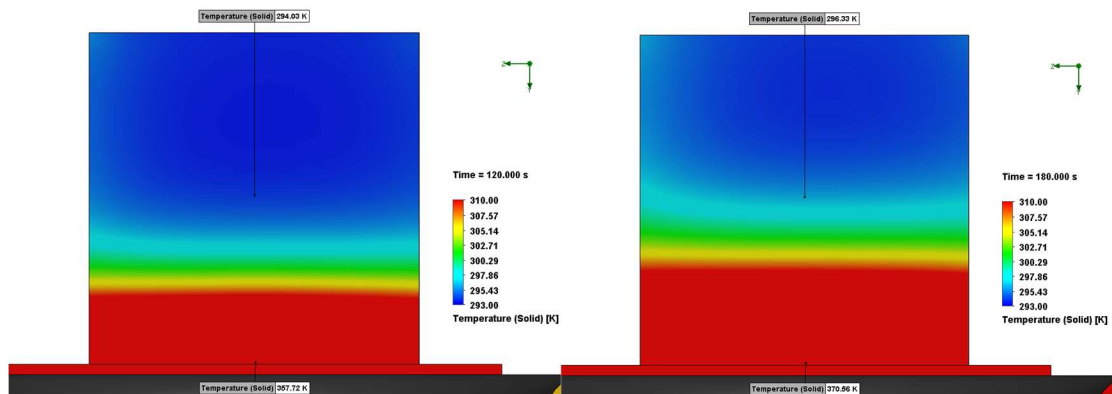


Figure 25a – 25b: Temperature cut plot of the Lavacrete concrete sample at $t = 120$ seconds (25a) and $t = 180$ seconds (25b). All Lavacrete figures use the same value color scale to represent temperature.

Finally, Figures 26a – 26b show the $t = 240$ seconds and $t = 300$ seconds time moments. In these figures, the asymmetrical heating seen in the previous figures becomes more apparent and begins to affect the entire temperature profile. The previously parallel line has become slanted downwards from the left, which coincides with the asymmetrical heating. However, the CSA sample saw a similar asymmetrical heating but did not have the same type of slanted temperature profile.

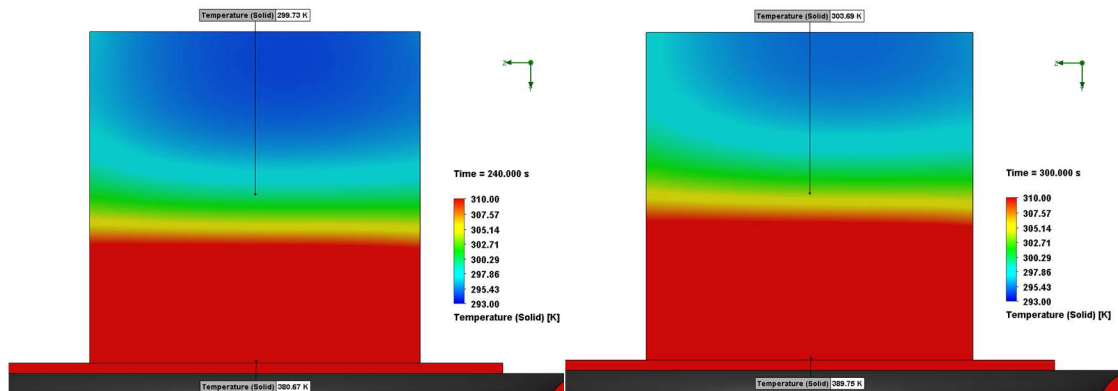


Figure 26a – 26b: Temperature cut plot of the Lavacrete concrete sample at $t = 240$ seconds (26a) and $t = 300$ seconds (26b). All Lavacrete concrete figures use the same value color scale to represent temperature.

2. Simulated Experiment Data

The results from simulations were all gathered from specified project goals that generated plots of temperature over time. As mentioned in the Chapter 3, the “Center” temperature reading from the simulated experiment is directly comparable to the thermocouple data from the physical experiment while the “Surface” temperature is used

for later calculations. Table XIV show the initial and final temperature at the center of the cube and at a centered point on surface of the cube contacting the copper plate.

TABLE XIV. SIMULATED DATA SUMMARY

Test 1: 6061 Aluminum Alloy		
	Center	Surface
T = 0s, Temperature [$^{\circ}C$]	20.05	20.05
T = 120s, Temperature [$^{\circ}C$]	81.89	114.45
T = 300s, Temperature [$^{\circ}C$]	114.45	115.38
ΔT , Temperature [$^{\circ}C$]	+ 94.40	+ 95.33
Test 2: CSA + Lunar Regolith Simulant		
	Center	Surface
T = 0s, Temperature [$^{\circ}C$]	20.05	20.05
T = 120s, Temperature [$^{\circ}C$]	20.28	25.72
T = 300s, Temperature [$^{\circ}C$]	25.73	120.17
ΔT , Temperature [$^{\circ}C$]	+ 5.68	+ 100.12
Test 3: MgO + Mars Regolith Simulant		
	Center	Surface
T = 0s, Temperature [$^{\circ}C$]	20.05	20.05
T = 120s, Temperature [$^{\circ}C$]	33.30	53.90
T = 300s, Temperature [$^{\circ}C$]	53.91	64.23
ΔT , Temperature [$^{\circ}C$]	+33.86	+44.18
Test 4: Lavacrete		
	Center	Surface
T = 0s, Temperature [$^{\circ}C$]	20.05	20.05
T = 120s, Temperature [$^{\circ}C$]	22.25	27.86
T = 300s, Temperature [$^{\circ}C$]	30.54	118.70
ΔT , Temperature [$^{\circ}C$]	+ 10.49	+ 98.65

The full data set for each material is shown individually in Figure 26. The significant difference in thermal conductivity between the aluminum 6061 alloy and the other concrete samples becomes especially apparent. Figure 27a shows all center temperature data on the same plot. In order to better see the temperature data from the concrete samples, which are the focus of this thesis, Figure 27b only shows the temperature of the concrete samples.

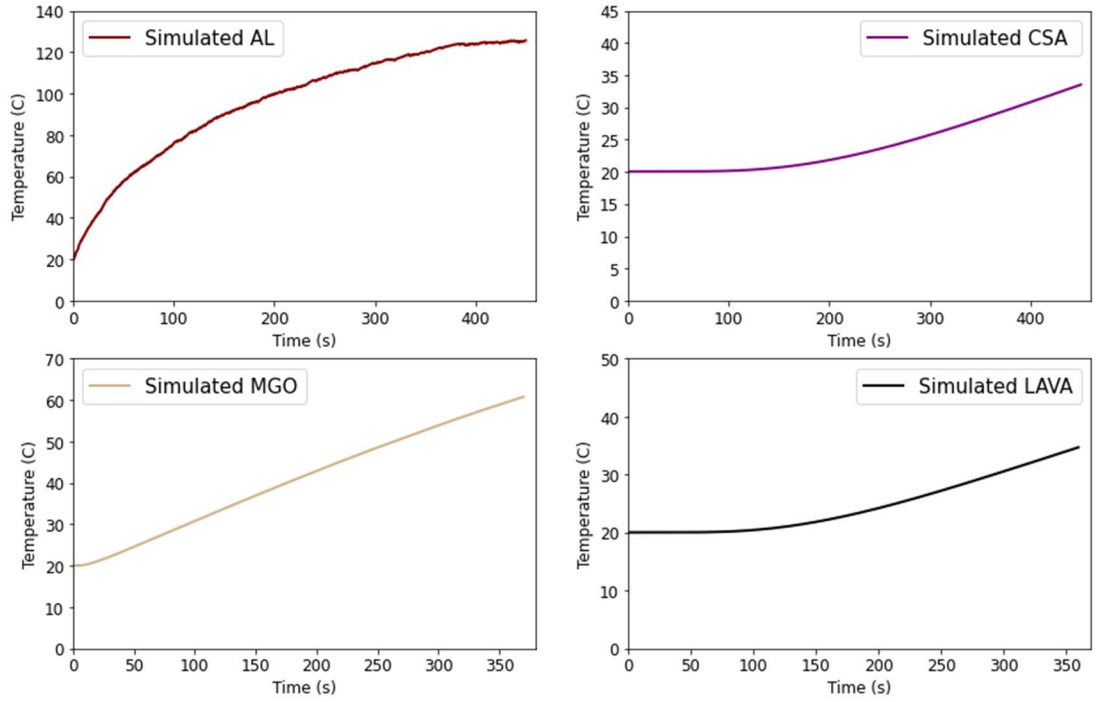


Figure 27: Temperature data from all of the simulated tests over the full test period

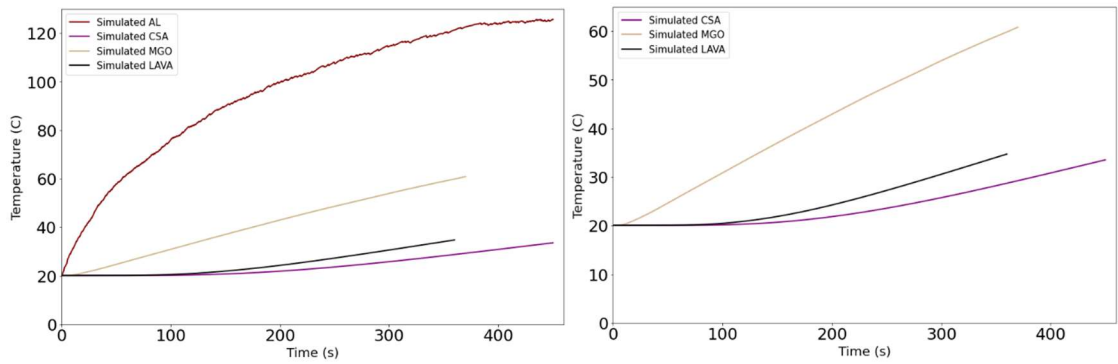


Figure 28a - 28b: Temperature data from all of the simulated tests (28a) and concrete material samples only (28b).

B. Physical Results

1. Physical Experiment Images

Each of the physical experiment images shown in this section were taken from video footage of the test. The first set of images shown in Figure 29a – 29d are meant to show the similar setup of each sample, corresponding to Figure 5 in the Chapter 3.

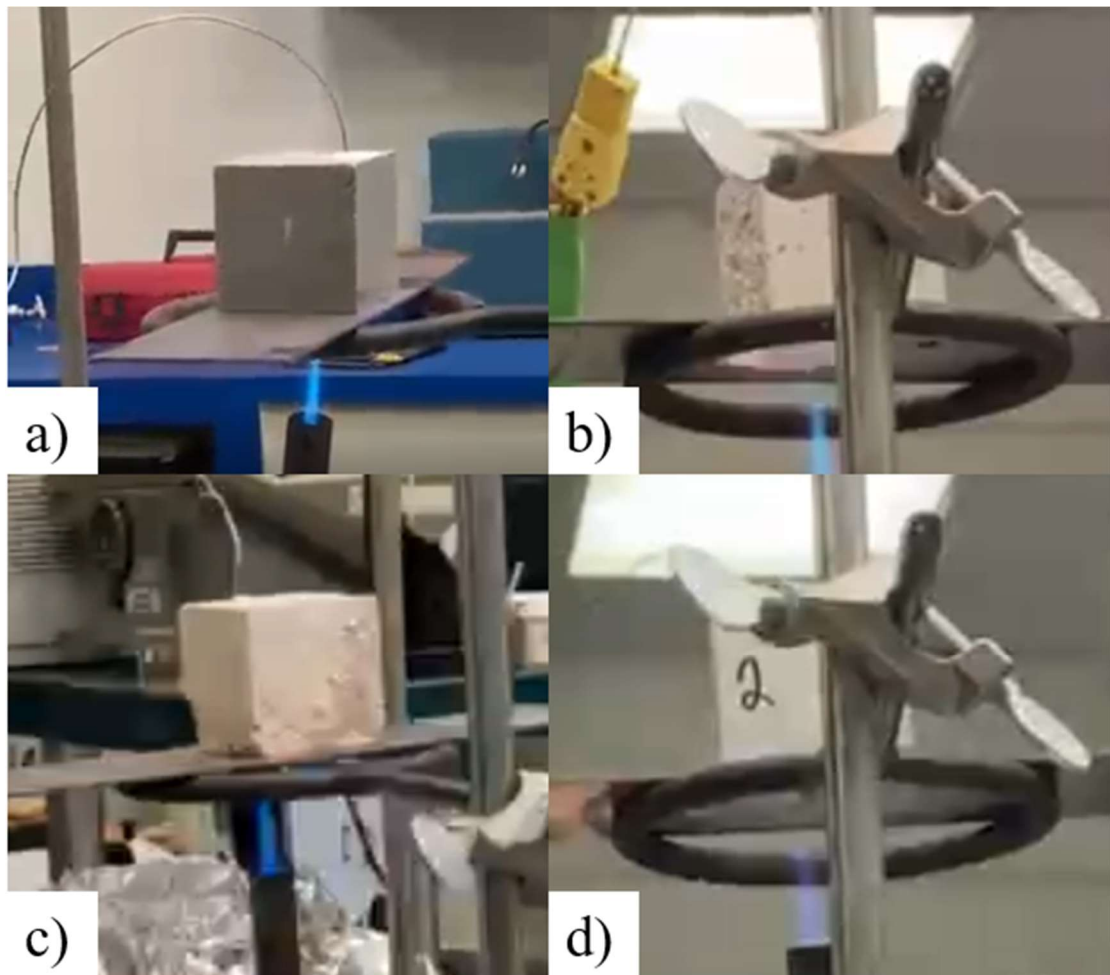


Figure 29a – 29d: Images taken during the physical experiment of the AL (29a), CSA (29b), MGO (29c), and LAVA (29d) samples

The first physical test conducted was the aluminum 6061 alloy. Figure 30a – 30b show the aluminum 6061 alloy sample at the beginning and end of the test. No notable changes were seen or reported in the color or shape of the sample.

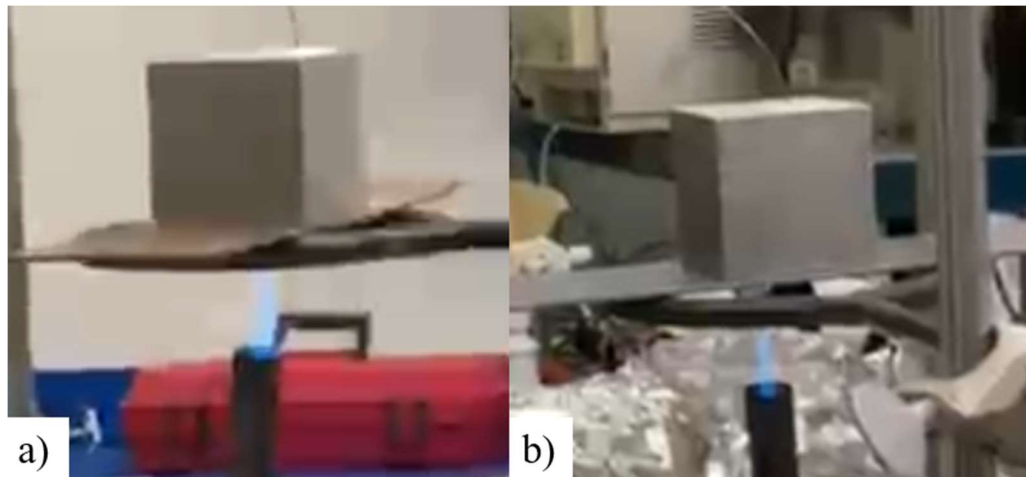


Figure 30a – 30b: Images taken during the physical experiment of the AL sample at $t = 10$ seconds (30a) and $t = 300$ seconds (30b)

The second physical test conducted was the CSA + Lunar Regolith Simulant concrete. Figure 31a – 31b show the CSA + Lunar Regolith Simulant sample at the beginning and end of the test. No notable changes were seen or reported in the color or shape of the sample.

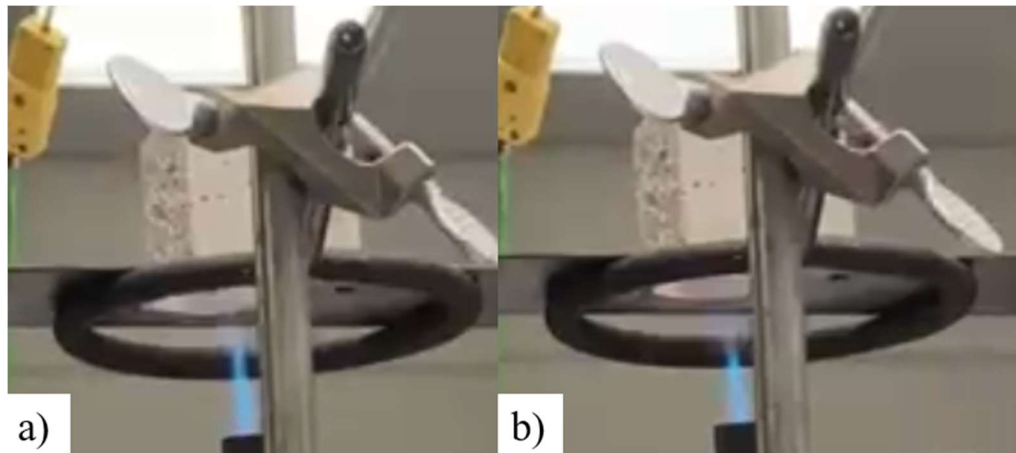


Figure 31a – 31b: Images taken during the physical experiment of the CSA sample at $t = 10$ seconds (31a) and $t = 300$ seconds (31b)

The third physical test conducted was the MgO + Martian Regolith Simulant concrete. Figure 32a – 32b show the MgO + Martian Regolith Simulant sample at the beginning and end of the test. No notable changes were seen or reported in the color or shape of the sample.

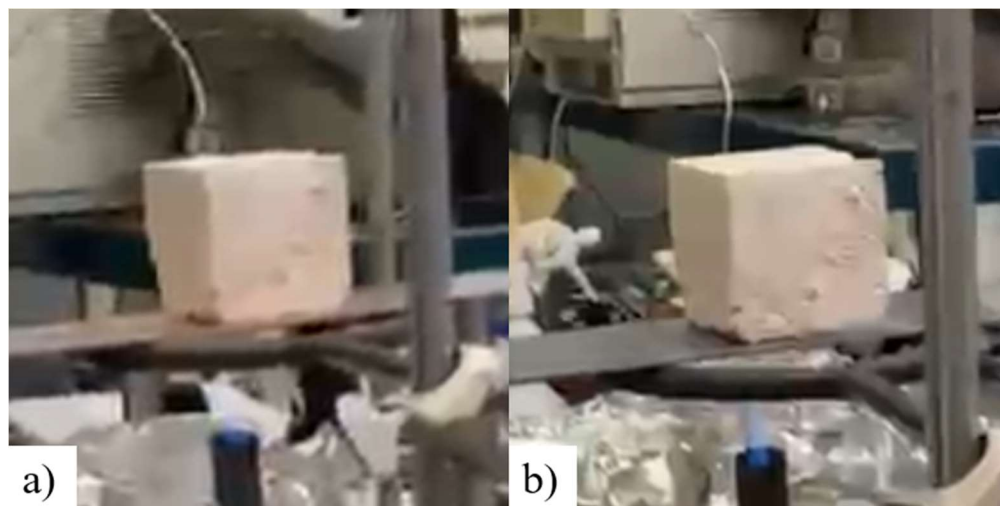


Figure 32a – 32b: Images taken during the physical experiment of the MGO sample at $t = 10$ seconds (32a) and $t = 300$ seconds (32b)

The fourth and final physical test conducted was the OPC-based “Lavacrete”. Figure 33a – 33b show the Lavacrete sample at the beginning and end of the test. No notable changes were seen or reported in the color or shape of the sample.

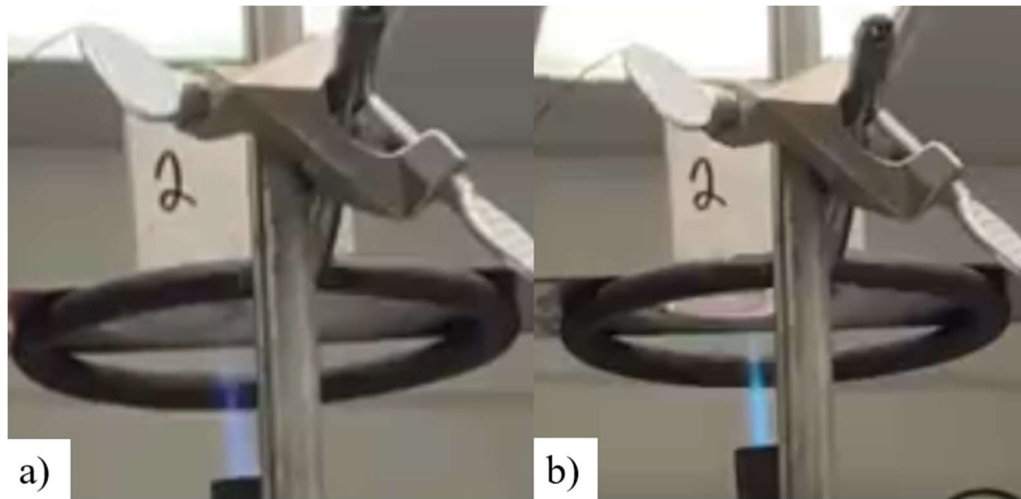


Figure 33a – 33d: Images taken during the physical experiment of the LAVA sample at $t = 10$ seconds (33a) and $t = 300$ seconds (33b)

2. Physical Experiment Data

The quantitative measurements of the physical experiment were either taken by a scale for mass or a thermocouple for temperature. Mass measurements were taken before and after the experiment and are shown in Table XV. The temperature of the sample was taken before, during, and after the ignition of the propane torch. The initial and final temperature of each sample is similarly shown in Table XVI.

TABLE XV. EXPERIMENTAL MATERIAL SAMPLE INITIAL & FINAL MASS

	Test 1: Aluminum 6061 Alloy	Test 2: CSA + Lunar Regolith Simulant	Test 3: MgO + Mars Regolith Simulant	Test 4: Lavacrete
Initial Mass [g]	383.73915	204.1166	254.0117	268.52668
Final Mass [g]	382.83196	198.67346	253.10454	265.80513
Δ Mass [g]	- 0.90719	- 5.44314	- 0.90716	- 2.72155

TABLE XVI. EXPERIMENTAL MATERIAL SAMPLE INITIAL & FINAL TEMPERATURE

	Test 1: Aluminum 6061 Alloy	Test 2: CSA + Lunar Regolith Simulant	Test 3: MgO + Mars Regolith Simulant	Test 4: Lavacrete
T = 0s, Temperature [°C]	20.94	21.91	21.40	21.94
T = 120s, Temperature [°C]	59.37	22.73	21.74	22.73
T = 300s, Temperature [°C]	161.54	39.85	28.59	24.00
Δ T, Temperature [°C]	+140.6	+17.94	+7.19	+2.06

Figure 34 shows the plot of internal temperature of each material sample individually. The aluminum 6061 alloy internal temperature showed a rapid response to the propane torch flame, having a notable impact on internal temperature within a few seconds. This was to be expected, as this was the only metallic sample. As expected, the AL sample had the sharpest and most significant temperature change. The relatively low temperature increase of the LAVA and MGO samples were somewhat surprising, and the implications of this are discussed in the Chapter 5.

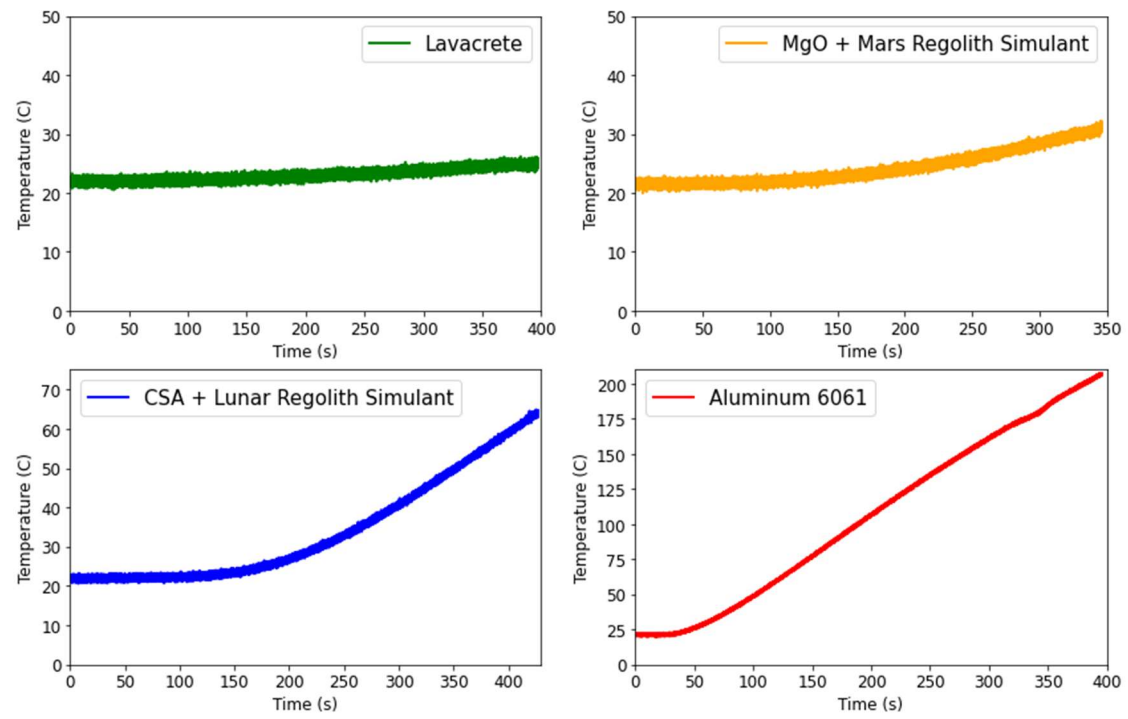


Figure 34: Temperature data from all of the physical tests over the full test period.

A combined plot of all tests is shown in Figure 35a. The significant difference in thermal conductivity between the aluminum 6061 alloy and the other concrete samples becomes especially apparent. In order to better see the temperature data from the concrete samples, which are the focus of this thesis, Figure 35b only shows the temperature of the concrete samples.

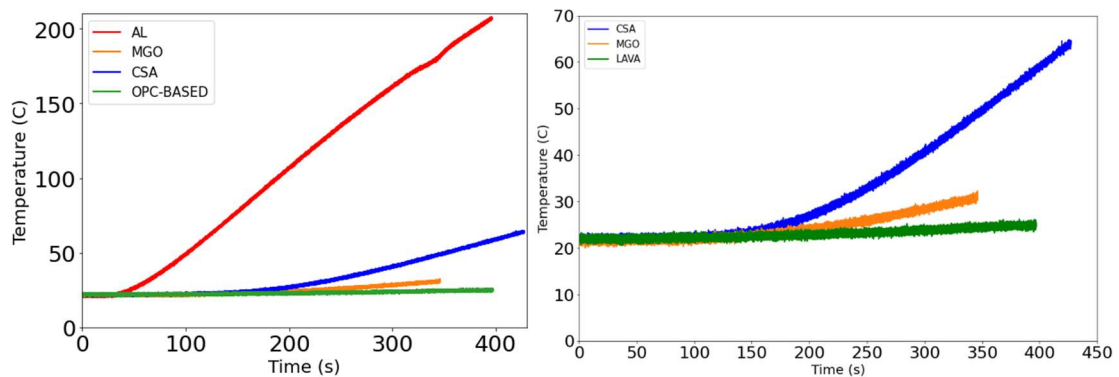


Figure 35a - 35b: Temperature data from all of the physical tests (35a) and concrete material samples only (35b).

C. Comparison Results

1. Simulated and Physical Data

This section compares data from the physical and simulated experiment. More specifically, this section focuses on the center temperature measured from the physical thermocouple and simulated sensor. Although some of the data and plots are individually shown in previous sections, Table XVII shows data at 60 second intervals and includes a percent difference calculation for each time moment. The percent different calculation is taken with respect to the physical temperature data.

TABLE XVII. SIMULATED AND PHYSICAL CENTER TEMPERATURE DIFFERENCE

Test 1: Aluminum Alloy 6061			
	Physical	Simulated	Percent Difference
T = 0s, Temperature [$^{\circ}C$]	20.94	20.05	- 4.27
T = 60s, Temperature [$^{\circ}C$]	30.03	61.71	+ 105.46
T = 120s, Temperature [$^{\circ}C$]	59.37	81.90	+ 37.95
T = 180s, Temperature [$^{\circ}C$]	94.31	95.74	+ 1.51
T = 240s, Temperature [$^{\circ}C$]	129.52	106.20	- 18.00
T = 300s, Temperature [$^{\circ}C$]	161.54	114.45	- 29.15
ΔT , Temperature [$^{\circ}C$]	140.59	94.404	- 32.86
Test 2: CSA + Lunar Regolith Simulant			
	Physical	Simulated	Percent Difference
T = 0s, Temperature [$^{\circ}C$]	21.91	20.05	- 8.47
T = 60s, Temperature [$^{\circ}C$]	21.85	20.05	- 8.20
T = 120s, Temperature [$^{\circ}C$]	22.73	20.29	- 10.76
T = 180s, Temperature [$^{\circ}C$]	25.71	21.29	- 17.20
T = 240s, Temperature [$^{\circ}C$]	31.45	23.16	- 26.32
T = 300s, Temperature [$^{\circ}C$]	39.85	25.73	- 35.14
ΔT , Temperature [$^{\circ}C$]	17.94	5.68	- 68.36
Test 3: MgO + Martian Regolith Simulant			
	Physical	Simulated	Percent Difference
T = 0s, Temperature [$^{\circ}C$]	21.40	20.05	- 6.32
T = 60s, Temperature [$^{\circ}C$]	21.49	25.85	+ 20.27
T = 120s, Temperature [$^{\circ}C$]	21.74	33.30	+ 53.16
T = 180s, Temperature [$^{\circ}C$]	23.91	40.54	+ 69.52
T = 240s, Temperature [$^{\circ}C$]	25.45	47.47	+ 86.54
T = 300s, Temperature [$^{\circ}C$]	28.59	53.91	+ 88.57
ΔT , Temperature [$^{\circ}C$]	7.18	33.86	+ 371.34
Test 4: Lavacrete			
	Physical	Simulated	Percent Difference
T = 0s, Temperature [$^{\circ}C$]	21.94	20.05	- 8.61
T = 60s, Temperature [$^{\circ}C$]	22.50	20.08	- 10.75
T = 120s, Temperature [$^{\circ}C$]	22.73	20.88	- 8.14
T = 180s, Temperature [$^{\circ}C$]	23.12	22.26	- 3.72
T = 240s, Temperature [$^{\circ}C$]	23.37	24.22	+ 3.65
T = 300s, Temperature [$^{\circ}C$]	24.00	27.86	+ 16.07
ΔT , Temperature [$^{\circ}C$]	2.06	7.81	+ 278.46

Beyond the 60-second interval time moments shown in Table XVI, Figure 36 shows plots of the full dataset of both physical and simulated experiments. In general, the physical experiment data lines appear thicker because they experienced small fluctuations that were not seen in simulations.

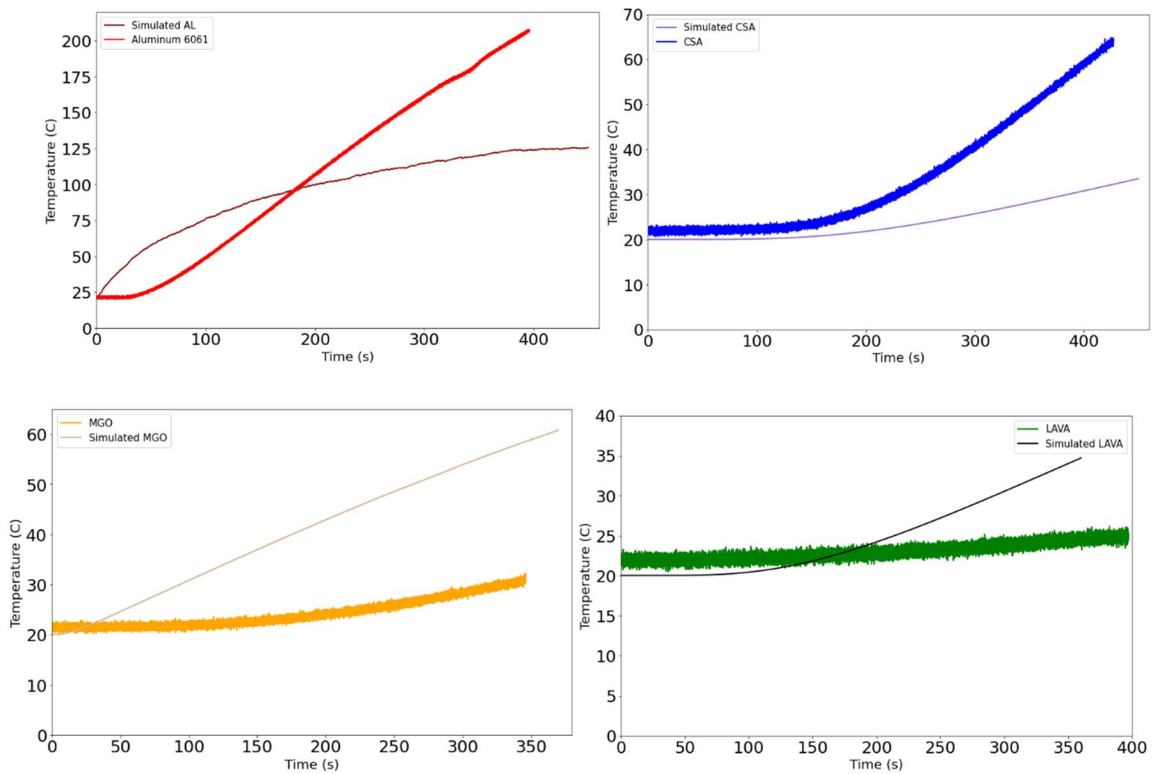


Figure 36: Temperature data comparing simulated and physical center temperature over time.

2. Simulated and Physical Flame Contact

Although the accuracy of the simulated torch flame is not the focus of this thesis, it is an important consideration for possible differences from the physical test. As described in the Chapter 3, the distance of the propane torch was kept constant while the intensity of the propane flame was controlled by a valve on the tank. The valve was adjusted such that the tip of the blue part of the flame was contacting the copper plate underneath the sample.

At several points throughout the physical experiment, the location or distance of the propane torch blue flame tip would deviate slightly. When this happened, MSFC personnel would reorient the torch to fix the location of the flame contacting the copper plate or adjust the propane intake valve to fix the length of the blue flame.

Between tests, the copper plate was cooled before placing another sample on top. This was an important step to prevent early heating of the sample, even despite the high thermal conductivity of the copper plate, which would reheat quickly anyway. Figure 37a -37b show the increasing size of the radiating heat area from $t = 60$ seconds to $t = 240$ seconds, at which point, the size of the radiating area was constant for the remainder of the test. Figure 38a – 38b show the surface temperature of the copper plate for the simulated experiment from a similar perspective at the same $t = 60$ s and $t = 240$ s time moments.

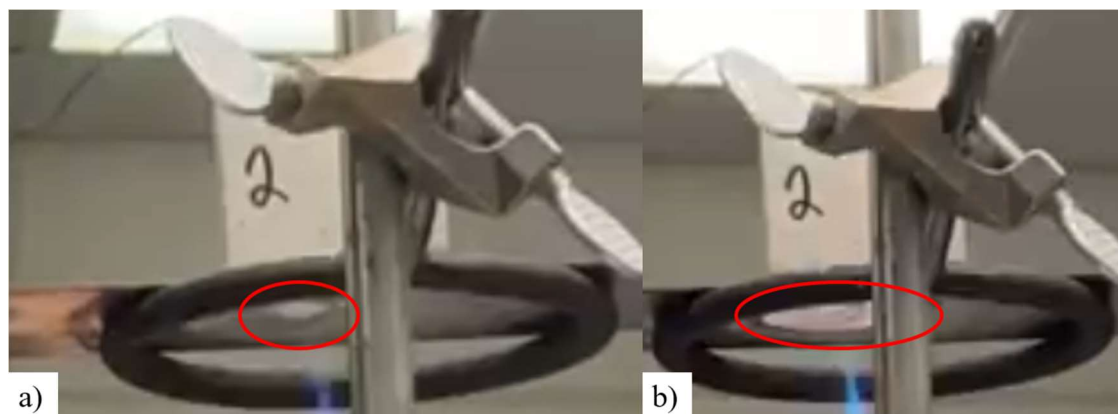


Figure 37a – 37b: Images taken from the physical experiment of the Lavacrete sample at $t = 60$ seconds (37a) and $t = 240$ seconds (37b). The size of the radiating area of the copper plate increased until $t=4$ minutes and remained roughly this size for the remainder of the test.

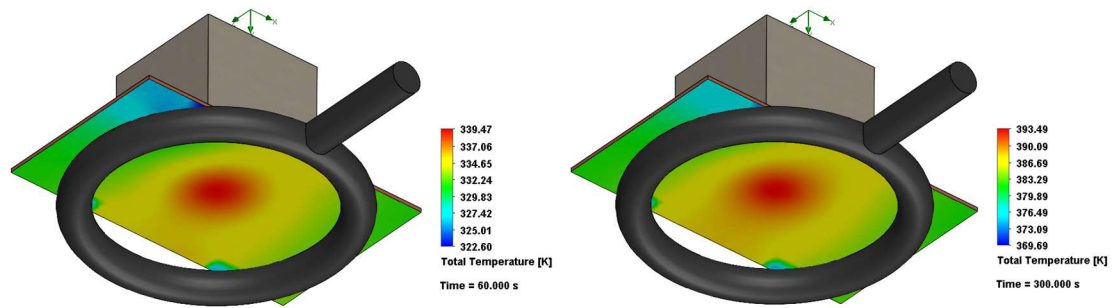


Figure 38a – 38b: Images taken from the simulated experiment of the CSA sample at $t = 60$ seconds (38a) and $t = 300$ seconds (38b) for temperature

Although heat flux data was not measured during the physical experiment, simulations allow us to view the heat flux within the cube sample. Figure 39 shows a cut plot of the heat flux with respect to the y-axis at $t = 240$ s. In this case, the greater the negative value (indicated by blue), the greater the heat transfer from the propane flame to the cube sample. In alignment with intuition, the greatest heat flux is seen closer to the copper plate and the least heat flux is seen at the top of the cube sample. There initially appears to be a radially outward heat transfer from the bottom-center of the cube sample. However, as that heat travels through the material towards the center, the profile becomes more uniform.

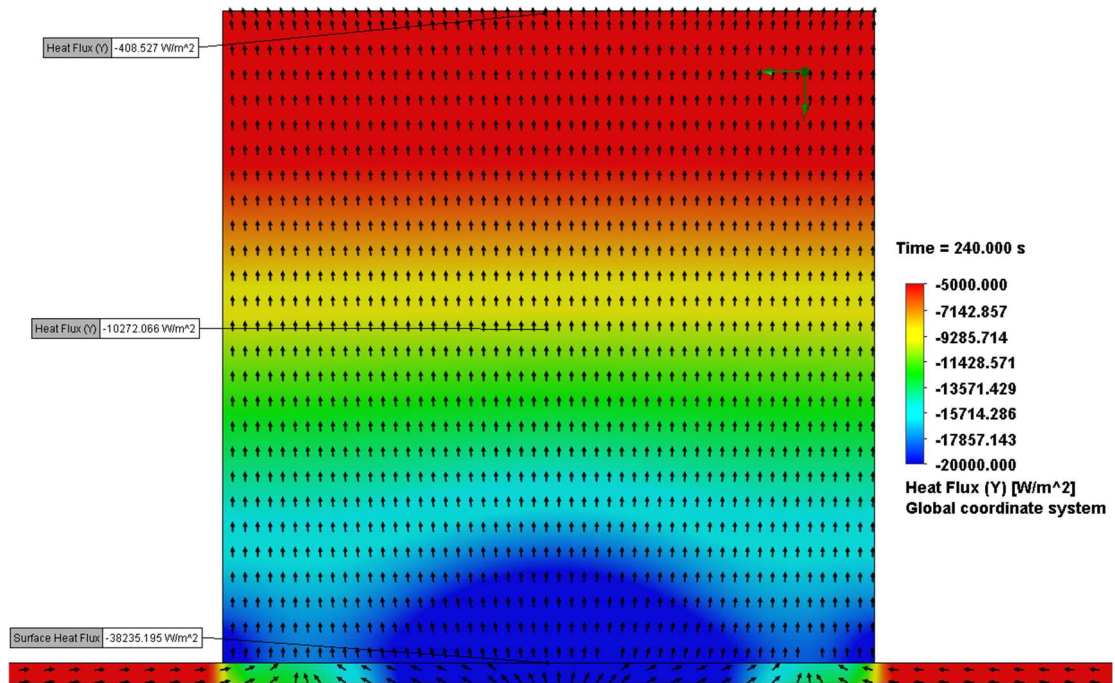


Figure 39: Heat flux cut plot from the simulated experiment of the MGO sample at $t = 240$ seconds.

In addition to images of the surface of the copper plate and within the material, heat flux data was collected from the surface of the cube sample contacting the copper plate. This data is plotted in Figure 40 and summarized in Table XVIII. Based on this data, it is reasonable to assume a consistent amount of heat flux for each simulated experiment. Table XVIII also includes the average heat flux and standard deviation calculation, which does not exceed 22% for any of the tests. Once again, the values shown in the chart and table are negative values, and the greater negative value indicates greater heat flux. From this data set, it becomes apparent that the heat flux was relatively constant for each test but was not consistent across all tests.

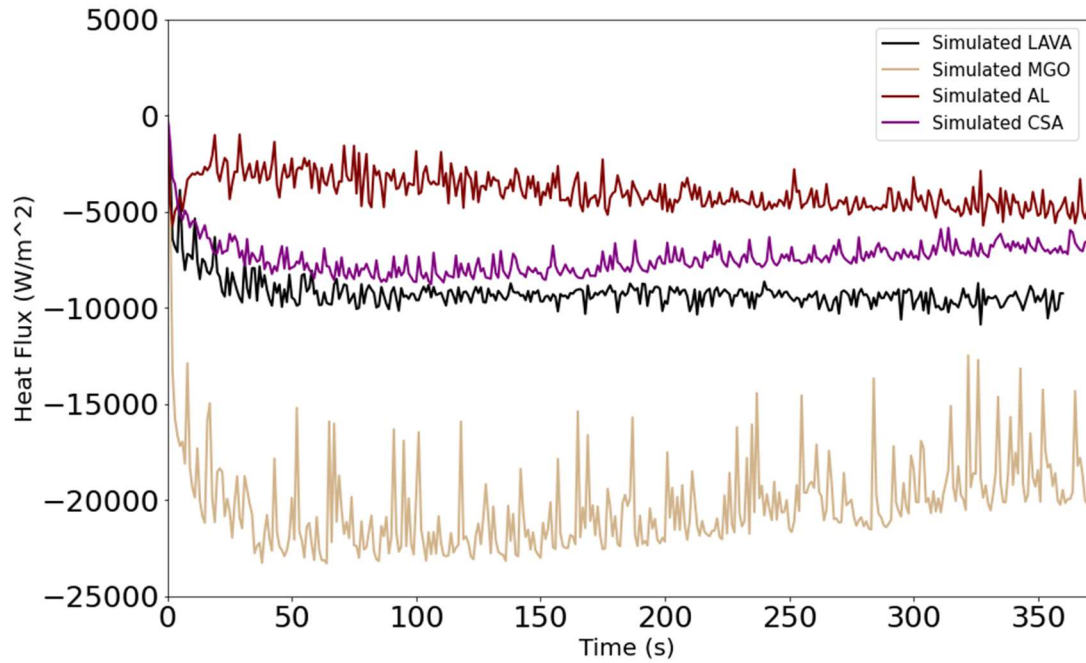


Figure 40: Heat flux cover time from the simulated experiment of all samples

TABLE XVIII. HEAT FLUX

Test 1: Aluminum 6061 Alloy	
T = 10s, Heat Flux $\left[\frac{W}{m^2}\right]$	-3028.25
T = 60s, Heat Flux $\left[\frac{W}{m^2}\right]$	-4033.94
T = 120s, Heat Flux $\left[\frac{W}{m^2}\right]$	-3093.37
T = 180s, Heat Flux $\left[\frac{W}{m^2}\right]$	-3959.92
T = 240s, Heat Flux $\left[\frac{W}{m^2}\right]$	-4915.37
T = 300s, Heat Flux $\left[\frac{W}{m^2}\right]$	-3215.58
Average, Heat Flux $\left[\frac{W}{m^2}\right]$	-4145.82
Standard Deviation	902.2638255 (21.76 % of avg.)
Test 2: CSA + Lunar Regolith Simulant	
T = 10s, Heat Flux $\left[\frac{W}{m^2}\right]$	-5515.08
T = 60s, Heat Flux $\left[\frac{W}{m^2}\right]$	-7682.04

T = 120s, Heat Flux $\left[\frac{W}{m^2}\right]$	-8333.87
T = 180s, Heat Flux $\left[\frac{W}{m^2}\right]$	-6645.999656
T = 240s, Heat Flux $\left[\frac{W}{m^2}\right]$	-7791.42
T = 300s, Heat Flux $\left[\frac{W}{m^2}\right]$	-7414.33
Average, Heat Flux $\left[\frac{W}{m^2}\right]$	-7550.08
Standard Deviation	858.84 (11% of avg.)
Test 3: MgO + Martian Regolith Simulant	
T = 10s, Heat Flux $\left[\frac{W}{m^2}\right]$	-35185.55
T = 60s, Heat Flux $\left[\frac{W}{m^2}\right]$	-31025.02
T = 120s, Heat Flux $\left[\frac{W}{m^2}\right]$	-35308.93
T = 180s, Heat Flux $\left[\frac{W}{m^2}\right]$	-30611.56
T = 240s, Heat Flux $\left[\frac{W}{m^2}\right]$	-35931.12
T = 300s, Heat Flux $\left[\frac{W}{m^2}\right]$	-33525.70
Average, Heat Flux $\left[\frac{W}{m^2}\right]$	-33597.98
Standard Deviation	2299.36 (6.84% of avg.)
Test 4: Lavacrete	
T = 10s, Heat Flux $\left[\frac{W}{m^2}\right]$	-7470.49
T = 60s, Heat Flux $\left[\frac{W}{m^2}\right]$	-9107.50
T = 120s, Heat Flux $\left[\frac{W}{m^2}\right]$	-9159.62
T = 180s, Heat Flux $\left[\frac{W}{m^2}\right]$	-9143.89
T = 240s, Heat Flux $\left[\frac{W}{m^2}\right]$	-9054.70
T = 300s, Heat Flux $\left[\frac{W}{m^2}\right]$	-9116.61
Average, Heat Flux $\left[\frac{W}{m^2}\right]$	-8842.14
Standard Deviation	672.93(7.61% of avg.)

D. Calculated Results

1. Temperature Gradient Calculation Results

The calculation process for the temperature difference between the surface and center of the cube sample was described in the Chapter 3. Table XIX shows the simulated values using the surface and center temperature from simulations, and the “actual” values using the surface temperature from simulations and the center temperature from the embedded thermocouple.

TABLE XIX. TEMPERATURE GRADIENT CALCULATION

Test 1: Alluminum Alloy 6061		
	Simulated	“Actual”
T_s [$^{\circ}C$]	115.38	115.38 (assume same as simulated)
T_c [$^{\circ}C$]	114.45	161.54
ΔT [$^{\circ}C$]	0.93	46.16
Test 2: CSA + Lunar Regolith Simulant		
	Simulated	“Actual”
T_s [$^{\circ}C$]	120.17	120.17 (assume same as simulated)
T_c [$^{\circ}C$]	25.73	39.85
ΔT [$^{\circ}C$]	94.44	80.32
Test 3: MgO + Martian Regolith Simulant		
	Simulated	“Actual”
T_s [$^{\circ}C$]	64.23	64.23 (assume same as simulated)
T_c [$^{\circ}C$]	53.91	28.59
ΔT [$^{\circ}C$]	10.32	35.64
Test 4: Lavacrete		
	Simulated	“Actual”
T_s [$^{\circ}C$]	118.70	118.70 (assume same as simulated)
T_c [$^{\circ}C$]	24.00	27.86
ΔT [$^{\circ}C$]	94.70	90.84

E. FEA Simulation Results

1. Simulated Strain Images

FEA simulations were run for each cube sample using CFD results at $t=120$ seconds and $t=300$ seconds. Each pair of figures shown below use the same value color scale for each pair in order to show the increasing strain over time. In all of the samples, strain was most concentrated on the face closest to the propane torch and grew upwards. However, the strain was also non-uniform, as seen in all figures for $t=300$ seconds, where there is a curved bowing pattern and a small decrease in strain in the center.

The AL sample experienced strain on the order of 10 to 100 microstrain. Figure 41a and 41b show the growth of the 600 microstrain region (in red) as it travels from the bottom surface towards the center. For both time moments, the strain is greater near the center than near the sides of the sample.

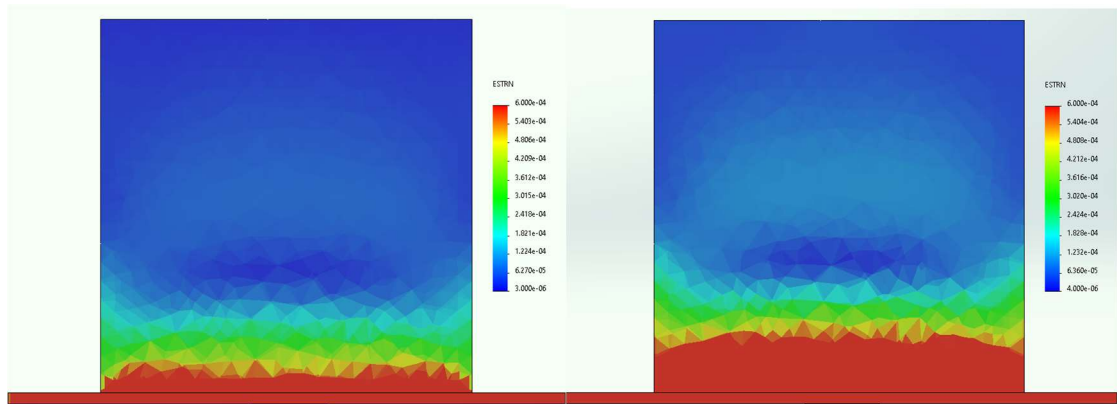


Figure 41a - 41b: Internal cut plot of strain within the AL sample at $t=120$ seconds (41a), and $t=300$ seconds (41b)

The CSA sample experienced extremely small amounts of strain on the order of 0.001 to 0.0001 microstrain. Unlike the AL and other samples, strain seemed to increase at the sides at a similar rate as the center. Despite the significant decrease in the order of magnitude of strain, the overall strain profile remains relatively similar to the strain seen in other samples. Figure 42a and 42b show the strain results of the CSA simulation.

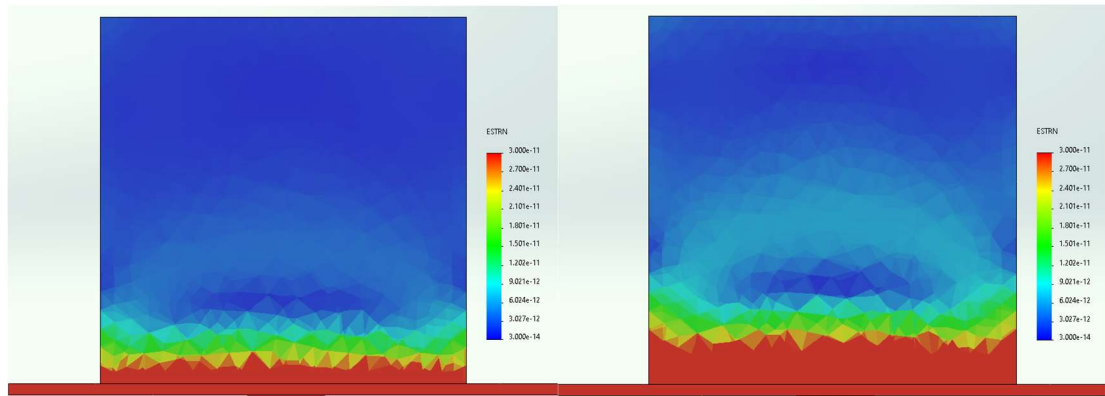


Figure 42a - 42b: Internal cut plot of strain within the CSA sample at t=120 seconds (42a), and t=300 seconds (42b)

The MgO sample experienced a considerable amount of strain on the order of 10 to 1000 microstrain. Similar to other samples, the bowing shape in the center of the sample can be seen in both time moments. The strain also appears to be more concentrated in the center than near the edges. Figure 43a and 43b show the strain results of the MGO simulation.

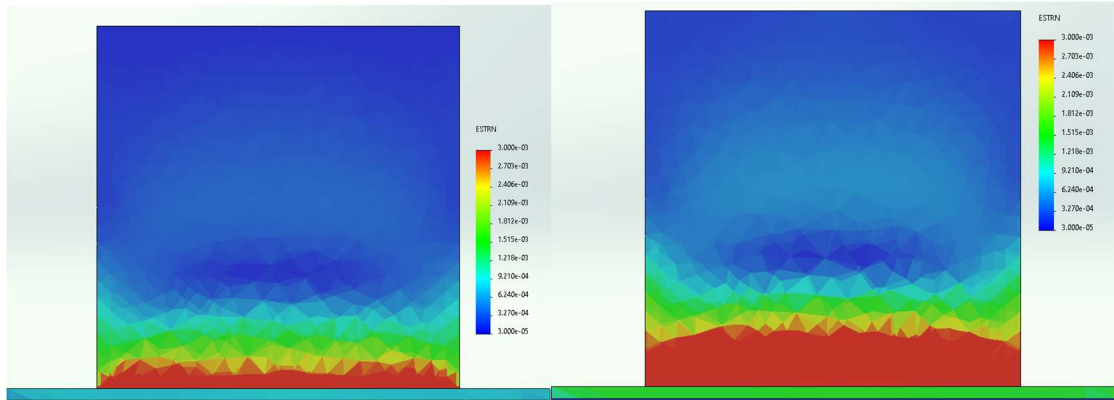


Figure 43a - 43b: Internal cut plot of strain within the MGO sample at $t=120$ seconds (43a), and $t=300$ seconds (43b)

Finally, the Lavacrete sample also experienced extremely small amounts of strain on the order of 0.001 to 0.0001 microstrain. Once again, despite the significant decrease in the order of magnitude of strain observed, the overall strain profile remains similar to that seen in other samples. Figure 44a and 44b show the strain results of the LAVA simulation.

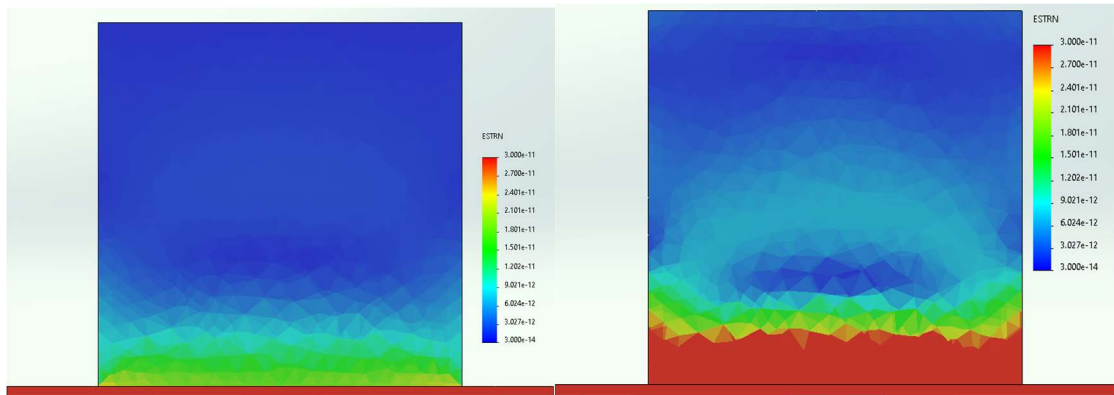


Figure 44a - 44b: Internal cut plot of strain within the LAVA sample at $t=120$ seconds (44a), and $t=300$ seconds (44b)

2. Simulated Stress, Strain, and Displacement Data

In addition to these cut plots, Table XX shows the average stress, strain, and displacement values at the nodes on the surface of the cube contacting the copper plate. These results are separated by the material being testing and the $t = 120$ seconds and $t = 300$ seconds time moments that were simulated. Recall that the surface of the copper plate contacting the cube was defined as a fixture, so these values are representative of the pure stress, strain, and displacement of the cube and not the copper plate.

TABLE XX. SIMULATED STRESS, STRAIN, AND DISPLACEMENT DATA

Test 1: Aluminum Alloy 6061			
	T = 120 seconds	T = 300 seconds	% Increase
Average Stress [<i>Pa</i>]	6.850 e+7	1.320 e+8	192.7
Average Strain [<i>strain</i>]	8.179 e-4	1.576 e-3	192.7
Average Displacement [<i>mm</i>]	5.503 e-5	1.105 e-4	200.7
Test 2: CSA + Lunar Regolith Simulant			
	T = 120 seconds	T = 300 seconds	% Increase
Average Stress [<i>Pa</i>]	1.190 e0	3.182 e0	267.4
Average Strain [<i>strain</i>]	4.522 e-11	7.598 e-11	168.0
Average Displacement [<i>mm</i>]	2.626 e-12	4.965 e-12	189.1
Test 3: MgO + Martian Regolith Simulant			
	T = 120 seconds	T = 300 seconds	% Increase
Average Stress [<i>Pa</i>]	1.274 e+9	2.450 e+9	3.63
Average Strain [<i>strain</i>]	4.076 e-3	7.839 e-3	192.3
Average Displacement [<i>mm</i>]	4.889 e-4	9.835 e-4	201.1
Test 4: Lavacrete			
	T = 120 seconds	T = 300 seconds	% Increase
Average Stress [<i>Pa</i>]	9.146 e-1	3.346 e0	365.8
Average Strain [<i>strain</i>]	2.188 e-11	7.999 e-11	365.8
Average Displacement [<i>mm</i>]	1.701 e-12	5.395 e-12	317.2

5. DISCUSSION & CONCLUSION

A. Discussion

1. Similarities and differences between simulated and physical experiments

The basis of this thesis is built on the similarity between physical experimentation and its simulated recreation. However, there are many limitations to the extent that we are able to apply these models and trust that they are accurate representations of real-world scenarios. This thesis sought to compare simulated and physical phenomena despite these differences, while still acknowledging the possible inaccuracy of the model. There are several points where we can compare the physical test and the simulated test, such as the heating profile of the propane torch flame, the fluctuation of the temperature measurement, and the temperature results themselves.

The first point of comparison for gauging the accuracy of the simulated model was the propane torch flame. Section 4.A showed simulation results focusing on the propane torch flame. The main purpose of the propane torch flame is to heat all cube samples uniformly and consistently such that the physical and simulated results can be compared. Using a combination of physical experiment footage and simulated experiment plots, we can better assess the uniformity and consistency of heat being transferred from the flame to the cube sample. In all physical tests, there was a glowing red-hot region of the copper plate that increased in size with time (shown in Figures 37a and 37b). Although the “red heat” phenomenon cannot be visualized in simulations, the images of the temperature on the flame-contacting side of the copper plate (Figures 38a and 38b) can give some insight into

the possibility of this phenomenon occurring in the simulated experiment. The Draper point describes the “red heat” phenomena using Wien’s displacement law to calculate the temperature at which solid materials will radiate light in the visible spectrum. The temperature at which solid materials typically begin to glow dull red is defined by the Draper point as 525°C (798 K). When looking at Figure 37a for $t = 60\text{s}$, it appears that the glowing region is approximately 1-2 cm in diameter. Assuming the Draper point phenomena is present, this implies that the center of the copper plate at $t = 60\text{s}$ is at least 525°C. However, when looking at Figure 38a of the simulation for the same time moment, the center temperature does not exceed 60°C, which is below the draper point. This inconsistency continues for Figure 37b at $t = 240\text{s}$ where the glowing red region has grown to 4-5 cm in diameter whereas the simulated temperature in Figure 38b still has not exceeded 120°C.

There are a few possible explanations for these inconsistencies. The first of which is that the material properties (primarily thermal conductivity) applied to the copper plate could be incorrect, which could result in a slower rate of heating of the simulated copper plate compared to the physical copper plate. Although the exact properties of the physical copper plate were unknown, it is somewhat reasonable to assume that the SolidWorks pre-defined properties for copper are within the same order of magnitude of the physical copper plate. The second possible explanation is that the flow properties (primarily stagnation temperature) applied propane torch flame could be incorrect, which could result in lower temperature flame compared to the physical propane torch flame. However, this point is

somewhat refuted by the independent flame simulation and comparison to literature discussed in Section 3.C.3.

A third explanation is that the Draper point is not the most accurate basis for correlating visible glow and temperature, and thus the conclusion that the physical and simulated temperatures are inconsistent is itself incorrect. The Draper point is derived from Wein's displacement law for blackbodies and is typically used for metals like steel, and the 525°C temperature is based on reaching the temperature needed to produce a wavelength of 3.6 μm or greater, which is near the minimum wavelength of visible spectrum. The "visibility" of this heat, however, is dependent on other factors, such as the lighting in the environment, the emissivity of the material, the color of the material, and other material properties that might deviate from the theoretical application of the Draper point. Finally, it is also possible that there were other sources of error not included in this short list, and any combination of these sources of error could compound in unpredictable ways.

The second point of comparison between simulated and physical tests is the resolution and accuracy of temperature measurement devices. For the simulated experiment, the simulated "thermocouple" was a coordinate-defined point in the simulation measuring solid temperature. There was very little fluctuation in the simulated data and the reported values were directly based on the simulation calculation at the given node. The physical thermocouple, on the other hand, experienced significant fluctuations for every experiment. These fluctuations were sometimes as high as 2 degrees Celsius within 0.01 seconds. For example, the CSA thermocouple reported a temperature of 21.5 degrees at

1.77 seconds, then 20.9 degrees at 1.78 seconds, and then 22.4 degrees at 1.79 seconds. It is unlikely that the temperature of the sample actually experienced a change of -0.6 degrees (2.7%) and then +1.5 degrees (7.2%) within 0.02 seconds and early enough within the test that the thermocouple would not have detected heating from the propane torch. These types of fluctuations persisted for this test and other tests. Ultimately, these thermocouple fluctuations were likely an artefact of the k-type thermocouple that was selected. Omega, the manufacturer of these thermocouples indicated that temperature fluctuations of ~2.8% are to be expected. As a result, the running average value, rather than the direct value, may be closer to the true temperature seen within the sample. Furthermore, future tests may also seek to use higher precision thermocouples that are less prone to fluctuation. Future testing and data analysis may also seek to correlate the fluctuating physical data to the more consistent simulated data and determine the most appropriate statistical approach for comparing results.

The third point of comparison between simulated and physical tests is the center temperature data itself. Section 4.C.1 directly compared the physical and simulated center temperature data and calculated the percent difference at 60-second intervals. In some cases, this percent difference was as low as 2%, while at other times, it was as high as 100%. In order to describe the overall similarity between the plots for the full experiment time, the Pearson Correlation Coefficient was used. The Pearson Correlation Coefficient (PCC) is defined as the ratio of the covariance of two sets of dependent data (in this case, physical and simulated temperature) that use the same dimension and type of independent

data (in this case, time) and the product of the standard deviation of each dependent data set. Microsoft Excel has an automatic equation for calculating the PCC which was used to calculate the PCC for this thesis, but Equation 3 below shows the full equation used.

$$PCC = \frac{\text{covariance}(\text{physical}, \text{simulated})}{\text{stdev}(\text{physical}) * \text{stdev}(\text{simulated})} \quad (3)$$

In other words, the PCC is used to correlate the consistency at which one dataset increases or decreases with respect to another dataset given the variation of each dataset but does not indicate the scale of that increase or decrease. The value of the PCC can range between -1 and 1, with negative values indicate a negative slope relationship while a positive values indicate a positive slope relationship. Values closer to zero indicate a more inconsistent relationship while values closer to -1 and 1 indicate a more consistent relationship. In all cases in this thesis, the slope is positive, meaning there is a directly relationship between the increase of the physical and simulated temperature, which intuitively makes sense as both increased in response to exposure to the propane torch flame. However, as seen in Section 4.C.1, there were times where the physical temperature increased faster or slower than the simulated temperature. Although the PCC isn't used to express this relative rate of increase, high PCC values can indicate a higher level of confidence that physical and simulated data will consistently increase with respect to each other, at which point scalar multipliers can be used to reach a more similar rate of increase. Table XXI shows the calculated PCC based on data between $t = 0\text{s}$ and $t = 300\text{s}$. The highest PCC was calculated for the MGO sample (~ 0.999) whereas the lowest PCC was calculated for the LAVA sample (~ 0.822).

TABLE XXI. PEARSON CORRELATION COEFFICIENT

	Test 1: AL	Test 2: CSA	Test 3: MGO	Test 4: LAVA
PCC	0.965612628	0.915197303	0.999671961	0.822440178

In addition to table XXI, we can visualize the Pearson Correlation via plots of simulated versus physical temperature data. Figures 45, 46, 47, and 48 include a black dashed line diagonally across the chart to show what a 1-to-1 relationship between simulated and physical data would look like. In other words, the black line represents a situation where the simulated and physical data increases at the same exact rate. Values that fall below this line indicate that the simulated temperature is increasing faster than the physical temperature while values that fall above this line indicate that the physical temperature is increasing faster than the simulated temperature. The first plot, shown in Figure 45, compares simulated and physical temperature data for the aluminum 6061 alloy, represented by the red line. Between $t = 0s$ and approximately $t = 180s$ (shown on Figure 35), the red line falls below the black line, indicating that the simulated temperature is increasing faster than the physical temperature. Then, after $t = 180s$, the physical temperature increases faster than the simulated temperature, and this is shown as the red line crossing above the black line. Both of these trends align with what was observed in the direct plot of both datasets over time in Figure 35.

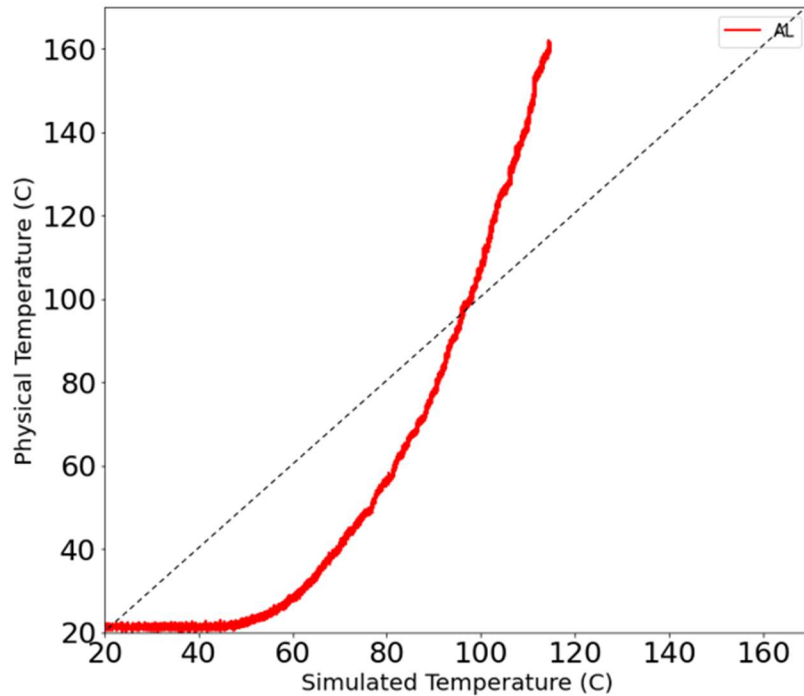


Figure 45: AL simulated center temperature versus physical center temperature.

The second plot, shown in Figure 46, is of simulated versus physical center temperature of the CSA + Lunar Regolith Simulant sample. For the entire test period, the physical temperature increased faster than the simulated temperature. The greater slope of the blue data line compared the black 1-to-1 line also indicates that the rate that the physical data is increasing with respect to the simulated data is increasing at a somewhat consistent rate. Once again, this trend aligns with the data from Figure 35.

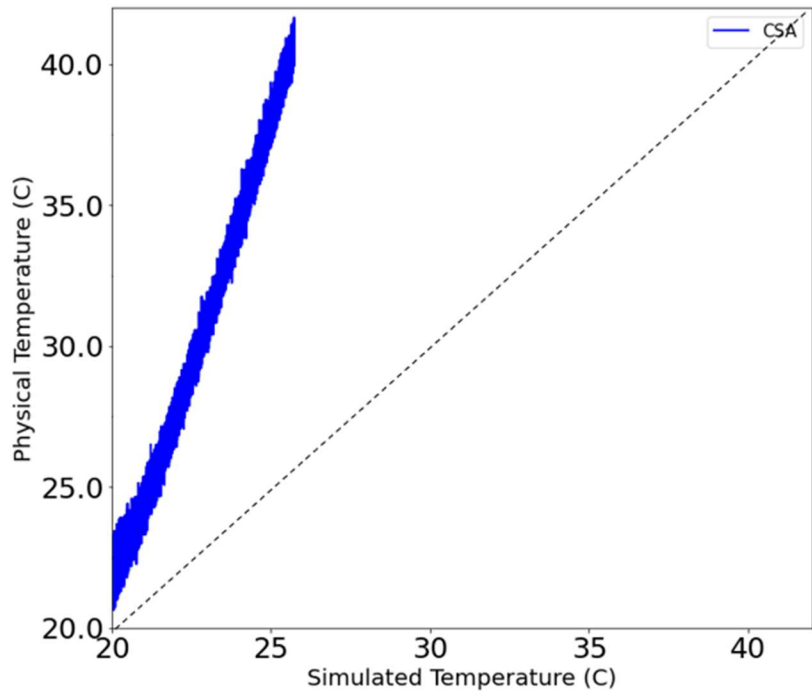


Figure 46: CSA simulated center temperature versus physical center temperature.

The third plot, shown in Figure 47, is of simulated versus physical center temperature of the MgO + Martian Regolith Simulant sample. Unlike the other concrete samples, the simulated MGO sample temperature increased faster than the physical temperature, and this is shown on the plot below as the orange data line being below the black reference line.

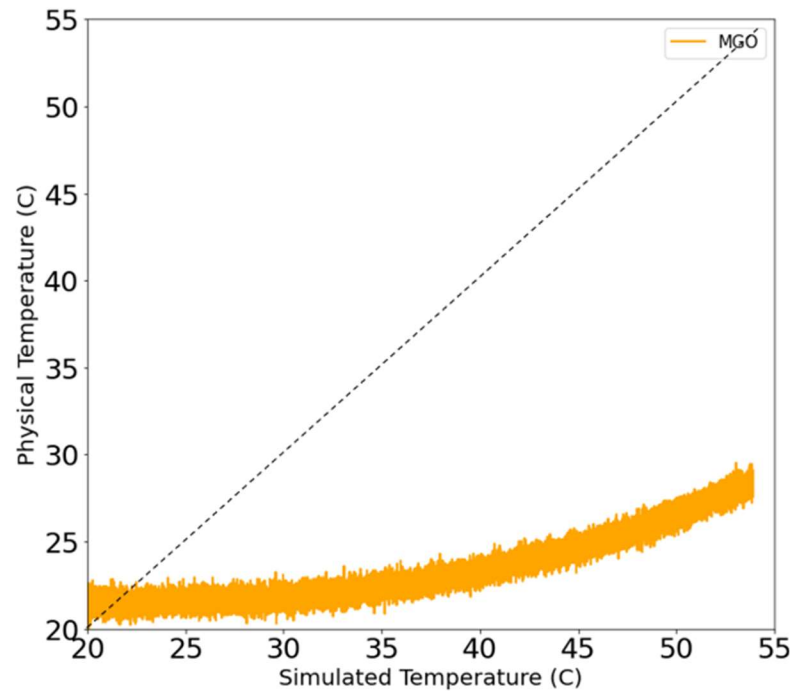


Figure 47: MGO simulated center temperature versus physical center temperature.

The fourth and final PCC plot, shown in Figure 47, is of the Lavacrete sample. Because the overall temperature difference measured in the physical test was so low, the range of values shown on this plot is much smaller, and as a result, the fluctuations that were previously discussed in this section become more apparent and influential. However, if we assume the running average of the measured value is a better representation of the actual temperature, we can better see the trend shown in the plot. Initially, the physical temperature is higher than the simulated temperature, and at approximately $t = 160\text{s}$ (shown in Figure 35), the simulated temperature exceeds the physical temperature. At this point, the simulated temperature continues to increase at a rate that is outpacing the rise of the physical temperature, which is represented in Figure 48 as the green data line crossing the black reference line.

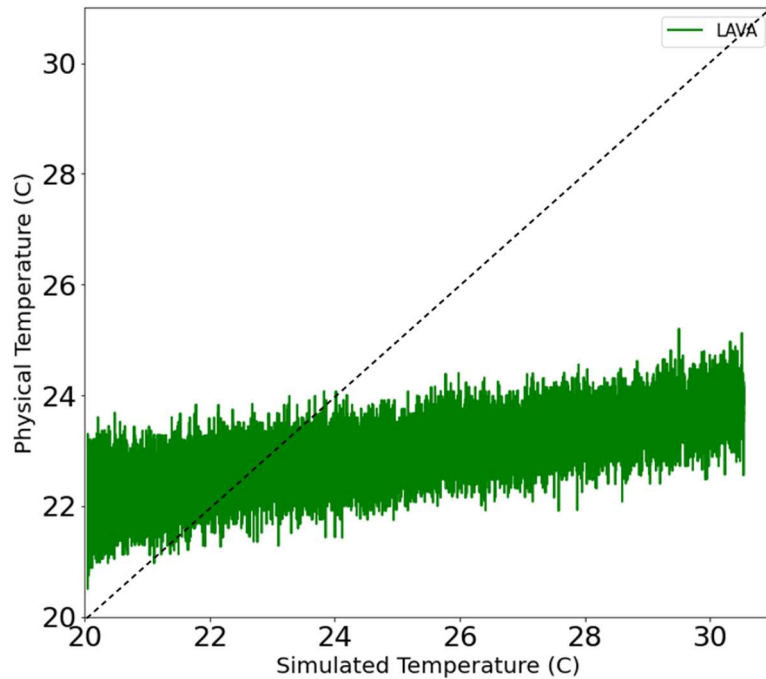


Figure 48: LAVA simulated center temperature versus physical center temperature.

The calculation of the Pearson Correlation Coefficient serves as a useful initial judgement of the consistency between the rate of temperature increase between physical and simulated tests. For the concrete samples with PCC values greater than 0.9 (CSA and MGO), we may be able to multiply the simulated results by a single scalar, piecewise scalar, or by a scalar that changes with time such that the simulated results better align with the physical data. In the absence of more accurate material properties (discussed in the next section), this method may prove useful for increasing the possible alignment between preliminary simulations and physical tests. Ultimately, future tests are needed to verify that this method is applicable, functional, and repeatable before being put to practical use. Nevertheless, the use of the PCC to correlate simulated and physical data shown in this thesis has the potential to be value for future work in structural health monitoring.

2. Effects of aggregate on thermal conductivity

Beyond the systemic differences between the simulation and physical experiment discussed in the previous section, the most impactful difference was the thermal properties of each material according to their aggregate. The properties given to the simulated concrete materials were based on values found in literature. Most of these sources used conventional ASTM C33/C33M or similar aggregate with no additives. With aggregate being a majority of the mass and volume of concrete, the substitution of lunar and Martian regolith simulant used in Test 2 and 3 is likely the primary reason for the difference in temperature slope between physical and simulated experiments.

Table XXII shows a comparison ranking the thermal conductivity value prescribed to simulations, the simulated center temperature, and the physical center temperature. As expected, the aluminum 6061 alloy sample had the highest thermal conductivity and therefore the highest temperature increase for both physical and simulated experiments. The more surprising result is seen in the relative ranks of the CSA + Lunar Regolith Simulant and other concrete samples. The CSA sample with lunar regolith simulant experienced the most significant temperature change of the three concrete samples. This is contrary to simulations where the CSA sample had the lowest temperature change.

TABLE XXII. THERMAL CONDUCTIVITY AND TEMPERATURE SLOPE COMPARISON

	Simulated Thermal Conductivity $\left[\frac{W}{m \cdot K}\right]$	Simulated Center ΔT $[^{\circ}C]$	Physical Center ΔT $[^{\circ}C]$
Highest	AL [167]	AL [94.4]	AL [140.6]
↑	MGO [41.9]	MGO [33.8]	CSA [17.9]
↓	LAVA [1.1]	LAVA [10.9]	MGO [7.2]
Lowest	CSA [0.97]	CSA [5.7]	LAVA [2.1]

Table XXII, shows that the simulated center temperature change aligns with the prescribed thermal conductivity values while the physical center temperature change does not. Again, the likely reason can be attributed to the difference in aggregate used. Although the general properties of these materials are unknown, we can compare the prescribed thermal conductivity values used for simulations to the thermal conductivity of the bulk elements found in lunar and Martian regolith.

A study of JSC – 1A Lunar Regolith Simulant (LRS) (Yuan & Kleinhenz, 2011) found that “thermal conductivity appears to be a linear function of average temperature,” indicating a changing value. The average thermal conductivity of LRS within the temperature range seen in this experiment (20°C -120°C) was approximately $0.23 \frac{W}{m \cdot K}$, which is much less than the $0.97 \frac{W}{m \cdot K}$ prescribed to the CSA + LRS simulations in this thesis. Yuan & Kleinhenz also indicated that the temperature-independent thermal conductivity of LRS was approximately $0.1961 \frac{W}{m \cdot K}$, which is even less than the temperature-dependent value of $0.23 \frac{W}{m \cdot K}$. In addition to the thermal conductivity of LRS changing with temperature, this same study found that the thermal conductivity changed with different heat fluxes.

One common approach to deriving material properties of composite materials is to use a general rule of mixtures, which provides theoretical upper and lower bound values. The rule of mixtures uses a weighted mean by volume to calculate various material properties,

including thermal conductivity. If using the rule of mixtures with the previously mentioned thermal conductivity of $0.23 \frac{W}{m \cdot K}$ for JSC – 1A LRS, the thermal conductivity of the cement used would need to be significantly higher to compensate for the extremely low thermal conductivity of the aggregate in order to produce the $+17.9 \text{ } ^\circ\text{C}$ temperature change seen in the physical sample.

Another study was similarly conducted and found a thermal conductivity of $0.8 \frac{W}{m \cdot K}$ for JSC Mars – 1A Martian Regolith Simulant and glass beads (Siegler, et al., 2012). Like the lunar aggregate, the thermal conductivity of the Martian aggregate was found to be lower than the prescribed value of $41.9 \frac{W}{m \cdot K}$ for simulations. However, in the case of Martian aggregate, there might be slightly more alignment with the physical temperature data. The $+7.2^\circ\text{C}$ temperature change of the MGO sample is closer to what would be expected if we assumed the thermal conductivity is closer to the lower $0.8 \frac{W}{m \cdot K}$ value, rather than the higher $41.9 \frac{W}{m \cdot K}$ value. Similarly using a rule of mixtures approach would lead us to assume that the thermal conductivity of the cement would still need to be significantly lower than the $41.9 \frac{W}{m \cdot K}$ found in literature for MGO based concrete.

Test data from both CSA with Lunar Regolith Simulant and MGO with Martian Regolith Simulant showed more alignment with the thermal conductivity values of lunar and Martian regolith aggregate rather than the prescribed thermal conductivity values of concrete using the same cement, but different aggregate. This partially explains how changing the aggregate, which makes up a majority of the mass and volume, can

significantly change the expected performance of concrete. However, making assumptions using the rule of mixtures still does not explain why the temperature change of both samples was so different than what was expected. For the CSA sample, an aggregate with a thermal conductivity of $0.23 \frac{W}{m \cdot K}$ would need to combine with cement with a thermal conductivity much higher than $0.97 \frac{W}{m \cdot K}$ in order to produce such a high temperature change of $+17.9^{\circ}C$. For the MGO sample, an aggregate with a thermal conductivity of $0.8 \frac{W}{m \cdot K}$ would need to combine with a cement with a thermal conductivity much lower than $41.9 \frac{W}{m \cdot K}$ in order to produce such a low temperature change of $+7.2^{\circ}C$. In both cases, the thermal conductivity of the cement would need to be an order of magnitude different (higher in the case of CSA and lower in the case of MGO) than the values of concrete using the same cement, but different aggregate found in literature in order to produce the temperature change seen in the physical test data. This suggests that the interaction between specific aggregate and cement combinations alter thermal properties more than what can be deduced from the aggregate or cement individually.

3. Simulated strain response to temperature.

As expected, the strain in all simulations was greatest near the source of heat at the bottom of the cube sample. However, the strain did not uniformly decrease throughout the material. In every simulation, a bowing strain pattern with a gap in strain was observed. This pattern does not align with the temperature gradient pattern for all time moments. Figure 49 shows the strain in the CSA sample at $t = 300$ seconds from Figure 43b, but with a white line indicating the strain “bowing pattern” and a black oval indicating the strain “gap”.

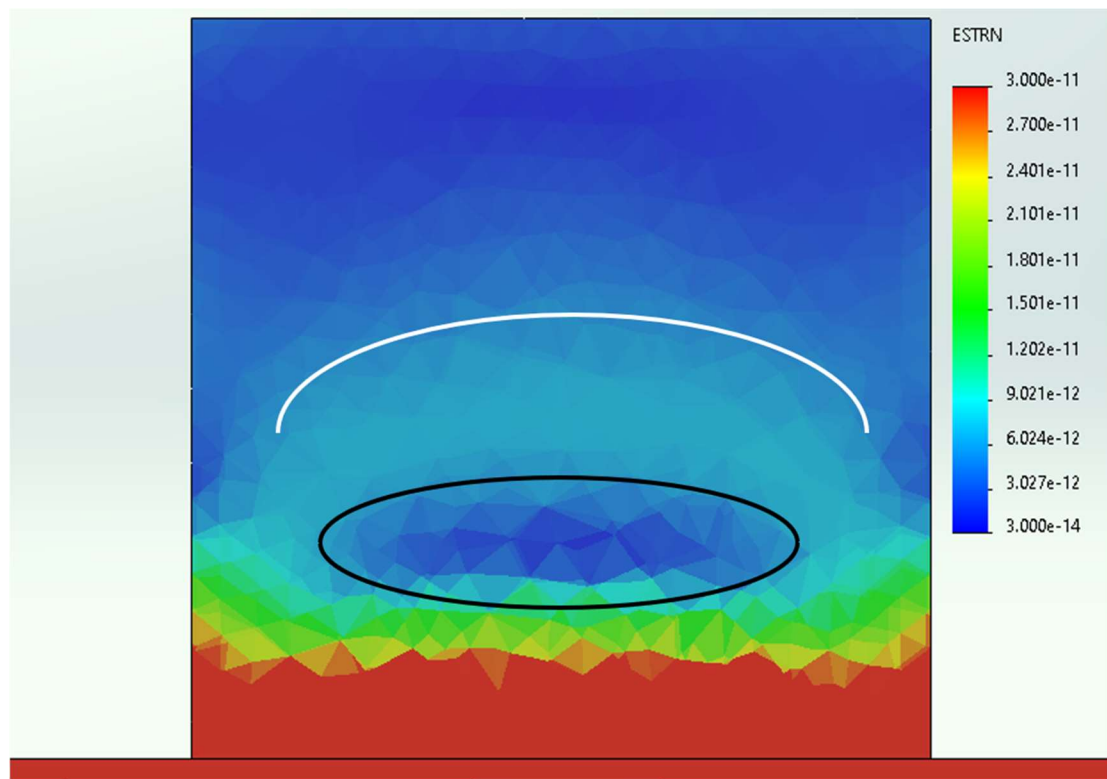


Figure 49: Strain cut plot of the CSA simulation at $t = 300$ seconds. Lines indicate strain bowing pattern (white) and strain gap (black).

Despite this pattern being generally visible in all simulations, there were also some variations between materials. Figures 45a – 45d show the same data from the $t = 300$ seconds time moment for all tests, but the color scale has been adjusted to emphasize the strain gap and bowing pattern. When comparing the results of these simulations, it becomes clear that the further the peak strain (red) has gone from the bottom to the top of the material, the higher the bowing pattern (green) and the larger the strain gap (blue). For example, the AL sample (Figure 50a) and MGO sample (Figure 50c) have higher peak strain than the other two samples, and as a result, their strain bowing shape is taller and the gap is larger.

It is unclear as to the exact cause and relationship between temperature, strain, and the bowing or gap seen in these figures. However, there are a few possible explanations of the existence, shape, and size of the strain response that warrants further investigation. The first explanation may be related to the test conditions, such as the cubic geometry of the samples or the type of heat source. Strain creep along the sides was seen to some extent in most samples. This might be attributed to the geometry resulting in a combined compression and expansion effect that is difficult to quantify, a faster temperature increase near the edges and corners of the sample where the heat has fewer opportunities to be transferred elsewhere, or the heated gas flowing around the copper plate heating the sample on the sides.

Another possible explanation for the size and shape of the strain gap and bowing pattern is related to the magnitude of the strain seen by the surface of the cube sample, which is

related to the temperature increase and the thermal expansion coefficient of the material. The AL and MGO samples experienced a larger bowing pattern that went higher up the sample, compared to the CSA and LAVA samples. The AL and MGO samples also experienced significantly more strain on the bottom face, on the order of 1000 microstrain, compared to the 0.0001 microstrain magnitude seen by the CSA and LAVA samples. Thus, it is possible that the higher order of magnitude of strain resulted in a larger and more prominent bowing pattern.

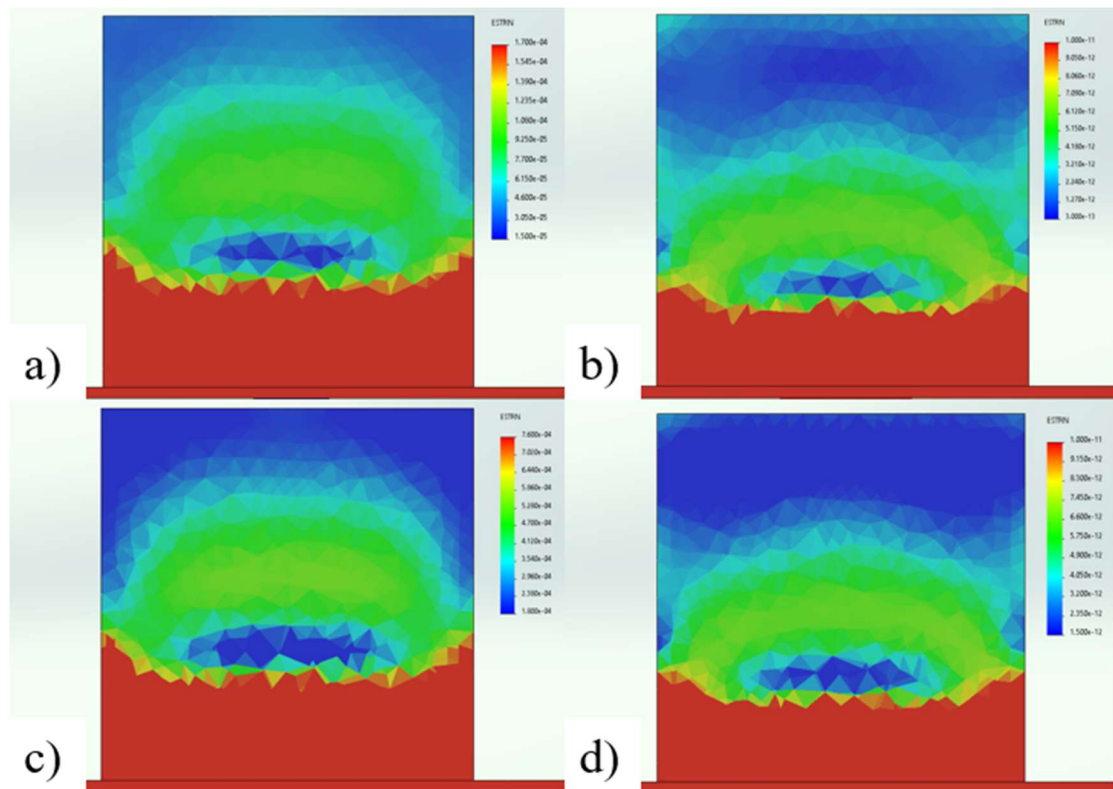


Figure 50a – 50d: Strain simulation of AL (50a), CSA (50b), MGO (50c), and LAVA (50d) at $t = 300$ seconds. These simulations show the same data as was shown in the Chapter 4, but with the color values for strain adjusted to better show the strain bowing pattern and gap.

The FEA simulation setup used to generate the results in Chapter 4 did not include gravitational loads. This was intentionally done to focus on the strain response to temperature alone. However, in order to address and compare the possible effects of gravity on strain, additional simulations were run with the CSA sample material properties using the same simulation setup parameters, but with gravitational loads. Figures 51a – 51c use Earth’s gravitational force ($9.81 \frac{m}{s^2}$) as a representation of the conditions experienced during the physical testing. Figure 51a shows the strain response to gravitational forces alone while Figure 51b shows the strain response to gravity and thermal loads imported from the CFD simulation at $t = 300$ seconds. In Figures 51a and 51b, the same value color scale for strain is used. Figure 51c shows the simulation of thermal loads without gravity, similar to figures shown in previous sections. The strain seen in Figure 51a and 51b are orders of magnitude greater than the no gravity simulation, and thus the color scale for Figure 51c is not the same. Contrary to the previously discussed observations, neither the strain bowing pattern, nor the strain gap are visible in the simulations where gravity is included (Figure 51a and 51b). In general, very few differences can be seen between Figure 51a and 51b because the strain generated from Earth’s gravity is dominating over the strain generated from the thermal shock of the propane torch. However, this does not mean to imply that the strain generated from thermal shock should be considered negligible, especially at the scale of the temperature and pressure generated by a lunar or Martian lander engines.

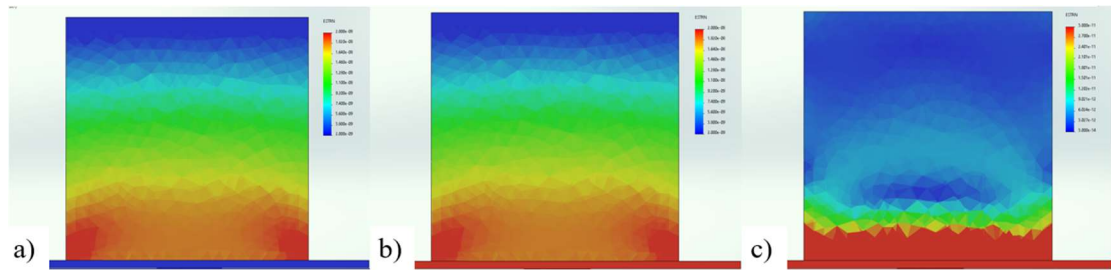


Figure 51a – 51c: Strain cut plot of the CSA simulation with Earth gravity loads only (51a), Earth gravity and thermal loads (51b), and thermal loads only (51c).

Similarly, simulations were run using the moon's gravity. Figures 52a and 52b show similar plots, but with the moon's gravitational force ($1.62 \frac{m}{s^2}$) as a representation of the conditions expected on the lunar surface. The color value scale for Figure 52a and 52b are the same. Figure 52a simulates the moon's gravity load only while Figure 52b simulates the moon's gravity load and the thermal load from the propane torch. Once again, Figure 52c is included to show the strain from thermal loads only, and the color value scale for strain is multiple orders of magnitude less than Figure 52a and 52b. Similar to the simulation of Earth's gravity, the strain generated from the moon's gravity continues to dominate over the strain generated from the thermal shock of the propane torch.

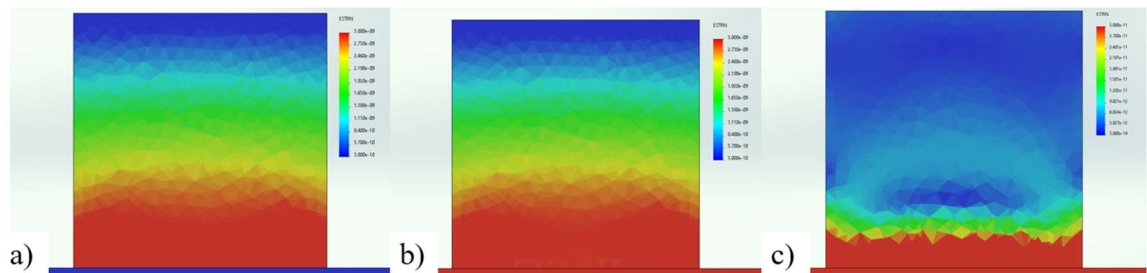


Figure 52a – 52c: Strain cut plot of the CSA simulation with lunar gravity loads only (52a), lunar gravity and thermal loads (52b), and thermal loads only (52c).

This section has attempted to describe and explain possible sources of strain seen in simulations. Bowing and gap patterns were observed in all simulations but varied slightly between materials. The shape of these patterns did not directly align with the shape of the temperature profile seen in Figures 15a – 26b, but might have some alignment with the heating profile seen in Figure 39. Other factors, such as the geometry or testing method may have influenced the strain response. In both Earth and lunar gravity conditions, the gravitational forces were shown to dominate the strain response. As expected, Earth's larger gravitational force resulted in more strain than the lunar gravity simulations. These patterns, relationships, and other factors influenced the strain response seen in simulations that could be confirmed with future physical testing.

4. Other possible influences on strain not seen in simulations.

Stress, strain, and displacement were not directly measured in the physical experiment. There are many limitations of the software that are unable to account for other possible influences on the mechanical response to high temperatures. One of these major influences that could not be considered in simulations include the effects of moisture within concrete.

As previously mentioned, the water to cement (W/C) ratio of all the tested samples was assumed to be 0.3 – 0.4 in order to coincide with the material property values found in literature for simulations. In reality, the water content of these samples may have been slightly lower or higher, and future structures built using in-situ resources will undoubtedly have a lower W/C ratio or use less water-dependent cement. The water content of concrete can affect the mechanical response to temperature change and flames. One study found that higher water content in concrete results in a lower compressive strength (Jansson &

Bostrom, 2013) while another study also found that a higher water content results in more severe fire spalling (BFT International, 2020). These trends are further supported by a study investigating concrete at temperatures seen in this experiment which found that “from about 22°C to 120°C the concrete compressive strength decrease is attributable to thermal swelling of the physically-bound water that causes disjoint pressures” (Naus, 2010). Rapid temperature changes in general result in the expansion of moisture retained by concrete, which causes cracks and spalling, which can be an indication of low bond strength. Although these materials were not directly exposed to the flame and no spalling was seen, it is likely that many of the effects of heating concrete were still seen, such as a decrease in bond strength and compressive strength.

In most conventional applications of concrete, there are also opportunities for additional moisture to seep into porous concrete. The moisture within the concrete expands as it freezes and leaves microcracks behind as it thaws. Thermal expansion joints and coatings are typically used to prevent expanding concrete from creating internal stress. Given the assumption of 0.3 – 0.4 W/C ratio used for these samples, it is possible that some of the physical materials that were tested experienced some additional strain due to this phenomenon, which was unable to be simulated.

5. *Mass loss of samples*

The SolidWorks software is incapable of simulating erosion, damage, phase changes, and other conditions described in the Chapter 2. Mass loss is one such condition that was seen in all samples tested, as shown in Table XIV. Much like the influences of strain not seen in simulations, many of the potential causes of mass loss discussed here are speculation and should be confirmed with additional testing.

Due to the copper plate being placed between the propane torch and the sample, it is believed that the mass loss seen in all samples was not caused by direct erosion. Because the cube samples were not in direct contact with the propane flame, it is also unlikely that the materials were directly burned off. However, heat can still induce outgassing that can result in mass loss, similar to a “bake-out” process used with concrete to release volatile organic compounds (VOCs) and accelerate curing. Moisture retained in concrete is also very susceptible to outgassing when heated. ASTM C566 even describes a process of slowly heating aggregate in order to measure moisture content. Although it is impossible to know the full extent of mass loss caused by these or other mechanisms, it is likely that some amount of outgassing occurred due to heat exposure and the water content of the concrete samples.

The AL and MGO + Martian Regolith Simulant samples experienced the lowest mass losses of 0.236% and 0.357% respectively. Given the assumption of heat-induced outgassing as a cause for mass loss, it would make sense that the AL sample experienced the lowest mass loss since it has no moisture. However, the cause of the MGO experiencing

a fraction of the mass loss compared to the LAVA and CSA samples (1.01% and 2.66% respectively) is unclear. The overall variation in mass loss across all concrete samples may be attributed to slightly different W/C ratios between samples or the different interactions between cement and water resulting in more or less moisture retained in the final concrete.

The CSA + Lunar Regolith Simulant sample experienced the most significant mass loss of 2.66% from the initial mass. On the moon, where CSA + LRS is likely to be used, there are additional considerations for avoiding mass loss. One of the main components of CSA is sulfur, which has been shown to easily sublime in concrete at low-pressure conditions (Grugel & Toutanji, 2008). This suggests that outgassing and mass loss may be even more significant under exposure to extreme heat in lunar conditions.

Although there remain unknowns surrounding the causes of mass loss in samples, it is reasonable to speculate that outgassing played a role. The full extent of that role is undetermined, but moisture and other compounds susceptible to heat-induced outgassing were present in concrete samples and experienced more mass loss than the aluminum sample as a result. Until simulations become capable of modeling phase changes in non-homogenous materials, further physical testing will likely be necessary to determine the contributing factors to mass loss of concrete exposed to high temperatures and low pressures.

B. Conclusion

1. Future Work

Future work could benefit from using software more capable of recreating physical conditions or altering the physical experiment to match software capabilities. The propane torch flame was sufficiently recreated based on matching temperature profile data. However, the simulation accuracy could further improve by simulating combustion, multi-phase flow, and fluid mixtures. Despite the simulated temperature profile matching reasonably well, the chemical reaction between the heated gas and the solid materials may provide more comparable data to the physical experiment. Other software packages, such as ANSYS Fluent, are capable of simulating these additional features at the cost of computation time and setup complexity that could not be afforded for this thesis. An alternative approach to better match the simulated and physical test would be to use heated air instead of propane. By using the same fluid to heat the cube sample as the environment, the single-fluid condition prescribed to the simulation would be consistent with the experiment. However, using air would also likely reduce the applicability of this work to the context in which these materials would be used on the moon and Mars.

For this experiment, the heat source used was a commercially available propane torch. The propane torch flame distance and orientation were maintained such that the blue flame tip was contacting the copper plate for all tests. However, despite the assumption of the blue flame tip being a constant temperature of 1018 K, the heat flux to the concrete sample changed between tests and remained relatively constant for each test, shown in Figure 39. As mentioned in the Section 5.A.1, changing the heating method of the material sample

will yield different results and allow for other analytical approaches. For example, the use of a constant heat flux source across all tests might allow for more direct comparisons between the temperature and strain response of each material. Similarly, a constant temperature condition at the top and bottom of the cube could allow for a calculation of the thermal conductivity. By changing the heat source and how it is applied to the material, other thermomechanical properties can be experimentally determined in order to better characterize these ISRU-based materials overall.

Several aspects of this thesis differ from expected use conditions on the moon or Mars. Before these materials are used for lunar or Martian infrastructure, testing under as many of the expected conditions as possible is necessary. The scale of the test article, the scale of the thermal and mechanical load, and the environmental temperature and pressure expected on the moon or Mars are a few of many conditions to test these materials. Lunar landing pads may be as large as 100 meters in diameter, with complex geometries. Upon scaling up the size and shape from a small cube to full-scale infrastructure made with ISRU materials, the applicability of subscale tests may be less direct. The landers that will be used for NASA's Human Landing System (HLS) and Commercial Lunar Payload Services (CLPS) programs will be significantly larger than Apollo missions, with more powerful engines. These larger engines will produce temperatures and pressures well beyond a propane torch, and as discussed in previous sections, the relationship between the thermal and strain response is neither direct nor linear. This may similarly limit the lessons learned from this thesis to being a survey of these conditions. Increasing the scale of the experiment

would also require additional instrumentation to measure strain and other parameters to directly compare with simulations. While these tests were performed in an open-air lab, future tests could implement a combination of a vacuum chamber and a drop test to simulate lunar or Martian ambient pressure and gravity. The change in ambient pressure will result in an under expanded plume that we are likely to see during launch and landing. Although gravity was observed to have a dominating effect over the strain response within the material according to simulations, the combination of all of these parameters changing at once may yield different results.

There are likely more opportunities to improve upon this work beyond what is discussed in this section. The examples in this section outline some of the most important parameters that would align the physical and simulated testing results, provide new information on material properties, and increase the relevance of this data in expected conditions.

2. *Conclusion*

The simulated and physical experimentation of lunar and Martian in-situ based concrete and other materials in this thesis has given insight into the expected performance of such materials when exposed to extreme thermal loads. By modeling the experiment with FEA and CFD simulations, we were able to gather high-resolution data that would otherwise be difficult to obtain. Internal cut plots of simulated temperature, heat flux, and strain provided the opportunity to see what was happening inside the physical samples and fill gaps in the physical data. Similarly, the photo and video of the test along with mass loss measurements allowed us to speculate about the effects of extreme heat exposure that would have otherwise been difficult or impossible to measure with simulations.

Similarities and differences between the physical tests and simulations highlighted discrepancies between the heating profile by using the assumption of the Draper point, the temperature fluctuation measured by the thermocouple, and the center temperature difference between physical and simulated tests. Using the Draper point assumption, it became clear that the simulated temperature was not reaching the temperature needed to emit the same glowing red heat. However, there are several limitations and conflicts with this assumption that could be better confirmed or denied with future tests using additional sensors. The temperature fluctuation observed in the physical test made it difficult to make direct comparisons with simulations without excess noise, but this could similarly be addressed with future tests using more precise sensors.

The Pearson Correlation Coefficient was used to compare physical and simulated temperature, and most tests showed a relatively high PCC value, with LAVA being the

lowest (~0.82) and MGO being the highest (~0.99). Given these PCC values, we can reasonably assume that simulations are capable of serving as a reliable starting point for estimating the thermal response of these materials. Future work may seek to use scalar multipliers that would be applied to the simulation data in order to achieve better alignment. However, in order to avoid arbitrarily “fixing” data to meet expectations, future work should seek to repeat this type of testing and comparison in order to thoroughly determine the validity of that approach.

Comparisons between physical and simulated data revealed how the application of material properties using the same cement but different aggregate can result in a different temperature response. The simulated concrete samples properties found in literature used the same type of cement, but with Earth-based aggregate instead of the lunar or Martian regolith simulant aggregates used to create the physical samples. This difference in aggregate properties was the likely the primary cause of the deviation between the simulated and physical temperature data. However, using the rule of mixtures to derive these material properties still did not sufficiently explain the misalignment.

Although no spalling, cracking, or other types of damage were directly observed in the physical test video footage, the simulated strain data and plots for each material revealed several unexpected and interesting trends. It was found that strain developed non-uniformly throughout the sample. Furthermore, the strain gap and bowing patterns in each sample could potentially be connected to the heating profile, the geometry of the cube samples, the order of magnitude of strain, or a combination of other factors, including or

excluding those listed. Ultimately, it is difficult to say for certain which of these reasons, if any, created the strain patterns seen in the plots without more and varied testing, but the information presented in this thesis serves as an initial reference point for those future tests. In addition to the simulation, several relevant sources were found that could explain causes of strain that could not be simulated, such as thermal swelling caused by water content found in concrete.

The mass of each sample was measured before and after testing in order to determine if and how much mass would be lost due to heating. Some amount of mass loss was to be expected, as various sources in literature describe a process of heat-induced outgassing of water, volatile organic compounds (VOCs), and in the case of CSA, sulfur components being especially prone to sublimation. Despite the assumption that each of the concrete samples had a similar water to cement (W/C) ratio of 0.3 – 0.4, the MGO sample experienced significantly less mass loss (~0.9g) than the LAVA (~2.7g) or CSA (~5.4g) samples for unknown reasons. The presence of sulfur might explain the much higher mass loss seen by the CSA sample, but questions remain as to why mass loss varied so much between samples.

Finally, upon reviewing the data collected and the test methods used in this thesis, potential objectives for future testing became clearer. A more thorough investigation of the mechanical and thermal properties of lunar and Martian-aggregate-based concretes, rather than the aggregates alone, will be necessary if we are to use simulation software to predict the performance of these materials on the moon or Mars. In addition to the derivation and

definition of material properties, the materials themselves should be tested in more relevant conditions, such as a vacuum, low gravity, different geometries, or a more significant heat source in order to empirically measure their performance. By repeatedly conducting these tests in parallel with simulations, we can validate and better understand the limitations of the software in this context.

Despite the ability of simulations to collect a variety of high-resolution data with reasonable alignment with physical data, it is important to recall the SHM axioms that served as the basis of this thesis. SHM Axiom II states “The assessment of damage requires a comparison between two system states” which have limited applications to the simulation where everything maintains an ideal, undamaged state and the software is incapable of modeling cracks, spalling, delamination, and other types of damage seen in concrete. Furthermore, SHM Axiom IVa states “Sensors cannot measure damage [...]” and calls for the use of signal processing and statistical classification in order to convert sensor data into damage information, which can be achieved by conducting physical and simulated tests in parallel, among other methods used in this thesis. The implementation of additional sensors, such as embedded strain gages, heat flux sensors or systems ensuring constant and uniform heating, and high-precision thermocouples to allow for more direct comparisons with simulation data would enable the application of SHM axioms in this new context. The combination of ISRU and additive manufacturing (AM) for extraplanetary structures creates new and exciting opportunities for the application of SHM techniques but requires further testing before being fully implemented.

3. *Summary*

The goal of this thesis was to create a test method for relevant subscale testing, collect physical and simulated data to draw meaningful conclusions, and serve as a basis for future testing and characterization of in-situ based materials. By exposing lunar and Martian regolith aggregate-based concrete to extreme temperatures and comparing their performance to simulations, we have identified several strengths of this approach, as well as opportunities for improvement. The work documented in this thesis also highlights the need for a broader and deeper investigation of structural health monitoring for extraterrestrial applications. The benefit of using simulation software for structural health monitoring is clear, and the analyses performed in this thesis are a demonstration of that value.

6. NOMENCLATURE

1-D – One-Dimensional
3-D – Three-Dimensional
AL – Aluminum 6061 Alloy
ASTM – American Society for Testing and Materials
AM – Additive Manufacturing
CAD – Computer-Aided Drawing
CFD – Computational Fluid Dynamics
CSA – Calcium Sulfoaluminate
FEA – Finite Element Analysis
FSHC – Fast-Setting Hydraulic Cement
HLS – Human Landing System
ISRU – In-Situ Resource Utilization
JSC – Johnson Space Center
LAVA – Lavacrete
LRS – Lunar Regolith Simulant
Lunar PAD – Lunar Plume Alleviation Device
MKP – Monopotassium phosphate
MGO – Magnesium Oxide (“Magnesia”)
MOC – Magnesium Oxychloride
MOS – Magnesium Oxysulfate
MRS – Martian Regolith Simulant
MSFC – Marshall Space Flight Center
NASA – National Aeronautics and Space Administration
OPC – Ordinary Portland Cement
PCC – Pearson Correlation Coefficient
PISCES – Pacific International Space Center for Exploration Systems
SHM – Structural Health Monitoring
VOC – Volatile Organic Compound
W/C – Water to Cement ratio

7. REFERENCES

- Allen, C. C., Morris, R. V., Jager, M. K., Golden, D. C., Lindstrom, D. J., Lindstrom, M. M., & Lockwood, J. P. (n.d.). MARTIAN REGOLITH SIMULANT JSC MARS-1. *Lunar and Planetary Science*.
- Al-masaeid, H. H. (2019). *Utilizing of Magnesium Oxysulfate Binders for Additive*. Retrieved from [egrove.olemiss.edu: https://egrove.olemiss.edu/cgi/viewcontent.cgi?article=2535&context=etd](https://egrove.olemiss.edu/cgi/viewcontent.cgi?article=2535&context=etd)
- Andersen, P. J., & Andersen, M. E. (1992). *A Guide to Evaluating Thermal Effects in Concrete Pavements*.
- Applied Ceramics, Inc. (n.d.). *ALUMINUM 6061*. Retrieved from [appliedceramics.net: https://www.appliedceramics.net/material/aluminum-6061/](https://www.appliedceramics.net/material/aluminum-6061/)
- Asadi, I., Shafigh, P., Hassan, Z., & Mahyuddin, N. (2018). Thermal conductivity of concrete - A review. *Journal of Building Engineering*.
- AZoNetwork UK. (n.d.). *Magnesia - Magnesium Oxide (MgO) Properties & Applications*. Retrieved from [AZo Materials: https://www.azom.com/properties.aspx?ArticleID=54](https://www.azom.com/properties.aspx?ArticleID=54)
- Bescher, E. (2018). *Calcium Sulfoaluminate-Belite Concrete: Structure, Properties, Practice*.
- BFT International. (2020, 11). *Strategies for enhancing fire resistance of high-strength concrete structures*. Retrieved from BFT International: <https://www.bft->

international.com/en/artikel/bft_Strategies_for_enhancing_fire_resistance_of_high-strength_concrete_3582973.html

Botha, J., & Spalding, D. (1954). The Laminar Flame Speed of Propane/Air Mixtures with Heat Extraction from the Flame. *Proceedings of the Royal Society of London: Mathematical and Physical Sciences*.

Campbell, A. I., Carson, C. H., Fiske, M. R., Martin, L. E., Murai, V. R., Ramirez, F. R., . . . Smith, K. C. (2022). Lunar PAD Post-Hot Fire Test Performance Evaluation. *AIAA SciTech*.

Carmichael, R. P. (2009). *Relationships Between Young's Modulus, Compressive Strength, Poisson's Ratio, and Time for Early Age Concrete*.

Davraz, M. (2014). The Effect of Boron Compound to Cement Hydration. *International Conference on Computational and Experimental Science and Engineering*.

Devadiga, A., & Rao, T. N. (2013). Optimizing Bunsen burner Performance Using CFD Analysis. *International Journal of Modern Engineering Research (IJMER)*.

Elgas. (2021, July). *Blue Flame vs Yellow Flame vs Red Flames – Gas Flame Color*. Retrieved from Elgas: <https://www.elgas.com.au/blog/1585-why-does-a-gas-flame-burn-blue-lpg-gas-natural-propane-methane/>

Emmons, P. H., & Vaysburd, A. M. (1995). *Performance Criteria for Concrete Repair Materials, Phase I*.

Farshad Rajabipour, Y. M. (2011). A Prediction Method of Tensile Young's Modulus of Concrete at Early Age. *Advances in Civil Engineering*.

- Fluke Process Instruments. (2021). *Emissivity Values for Metals*. Retrieved from Fluke Process Instruments: <https://www.flukeprocessinstruments.com/en-us/service-and-support/knowledge-center/infrared-technology/emissivity-metals>
- Fluke Process Instruments. (2022). *Emissivity Values for Metals*. Retrieved from [www.flukeprocessinstruments.com](https://www.flukeprocessinstruments.com/en-us/service-and-support/knowledge-center/infrared-technology/emissivity-metals):
<https://www.flukeprocessinstruments.com/en-us/service-and-support/knowledge-center/infrared-technology/emissivity-metals>
- Ge, Z. (2005). *Predicting temperature and strength development of the field concrete*.
- Grugel, R. N., & Toutanji, H. (2008). Sulfur “concrete” for lunar applications – Sublimation concerns. *Advances in Space Research*, 103 - 112.
- Huang, G., Pudasainee, D., Gupta, R., & Liu, W. V. (2021). Thermal properties of calcium sulfoaluminate cement-based mortars incorporated with expanded perlite cured at cold temperatures. *Construction and Building Materials*.
- Ihlefeld, J. F., Brown-Shaklee, H., & Hopkins, E. P. (2011). *Grain size and porosity effects on the thermal conductivity of SrTiO₃ thin films*.
- Ioannou, S., Reig, L., Paine, K., & Quillin, K. (2014). Properties of a ternary calcium sulfoaluminate–calcium sulfate–fly ash cement. *Cement and Concrete Research*.
- ISSI. (2013). *thin-filament velocimetry*.
- Jansson, R., & Bostrom, L. (2013). Fire spalling in concrete – The moisture effect, part II. *SP Technical Research Institute of Sweden*.

- Khalil, W. I. (2009). Using Citric Acid as an Admixture and its Influence on some Properties of Concrete. *Eng. Tech. Journal*.
- Khare, S., Bannerman, M., & Glasser, F. (2017). Pilot scale production of novel calcium sulfoaluminate cement. *The University of Sheffield: Chemical Engineering and Processing*. Retrieved from <https://eprints.whiterose.ac.uk/172110/7/Pilot%20scale%20production%20of%20novel%20calcium%20sulfoaluminate%20cement%20clinkers%20and%20development%20of%20thermal%20model.pdf>
- Kim, J. J., Youm, K.-S., & Reda Taha, M. M. (2014). Extracting Concrete Thermal Characteristics from Temperature. *The Scientific World Journal*.
- Klein Tools. (n.d.). *Emissivity Chart*. Retrieved from Klein Tools: <https://www.kleintools.com/sites/kleintools/files/instructions/Emissivity-Chart-139697ART.pdf>
- Lam, C., & Bremhorst, K. (1981). A Modified Form of the k-E Model. *ASME Journal of Fluids Engineering*.
- Lehigh Technical Services. (2002). *Type III, High-Early-Strength, Portland Cement*.
- Louis Schuman, J. T. (1943). Tensile And Other Properties of Concretes Made With Various Types of Cements. *Journal of Research of the National Bureau of Standards*.
- Mo, L., Deng, M., Tang, M., & Al-Tabbaa, A. (2014). MgO expansive cement and concrete in China: Past, present and future. *Cement and Concrete Research*, 1-12.

- Mounanga, P., Bastian, G., & Khelidj, A. (2018). A study of the apparent thermal conductivity of cement. *HAL*.
- National Weather Service. (2021). <https://w1.weather.gov/data/obhistory/KHSV.html>. Retrieved from <https://www.weather.gov/>.
- Naus, D. J. (2010). A Compilation of Elevated Temperature Concrete Material Property Data and Information for Use in Assessments of Nuclear Power Plant Reinforced Concrete Structures. *United States Nuclear Regulatory Commission*.
- Nobre, J., Hawreen, A., Bravo, M., Evangelista, L., & de Brito, J. (2020). Magnesia (MgO) Production and Characterization, and Its Influence on the Performance of Cementitious Materials: A Review. *Materials*.
- Nobre, J., Hawreen, A., Bravo, M., Evangelista, L., & de Brito, J. (2020). Magnesia (MgO) Production and Characterization, and Its Influence on the Performance of Cementitious Materials: A Review. *MDPI Materials*.
- Omega. (n.d.). *Super OMEGACLAD XL Thermocouple Probes Information Sheet*. Retrieved from <https://www.omega.com>: https://assets.omega.com/pdf/test-and-measurement-equipment/temperature/sensors/thermocouple-probes/KQXL_NQXL.pdf
- Portland Cement Association. (n.d.). *Concrete Aggregates*. Retrieved from [cement.org](https://www.cement.org): <https://www.cement.org/cement-concrete/concrete-materials/aggregates>

- Ravi, K., Sivananthan, S., & Samuel, S. J. (2019). Effect of SiC particles reinforcement on mechanical properties of aluminium 6061 alloy processed using stir casting route. *Materials Today: Proceedings 21*.
- Sato, K., Manabe, T., Polivka, J., Ihara, T., Kasashimra, Y., & Yamaki, K. (1996). Measurement of the complex refractive index of concrete at 57.5 GHz. *IEEE Transactions on Antennas and Propagation*. Retrieved from IEEE Xplore.
- Sauereisen. (2019, July). *Sauereisen Electrotamp Cement No. 8 Properties*. Retrieved from sauereisen.com: <https://www.sauereisen.com/wp-content/uploads/8.pdf>
- Siegler, M., Aharonson, O., Carey, E., Choukroun, M., Hudson, T., Schorghofer, N., & Xu, S. (2012). Measurements of thermal properties of icy Mars regolith analogs. *Journal of Geophysical Research*.
- Sobachkin, A., & Dumnov, G. (2013). Numerical Basis of CAD-Embedded CFD. *NAFEMS World Congress*.
- The Aluminum Association, Inc. (Revised 2001). *International Alloy Designations and Chemical Composition Limits for Wrought Aluminum and Wrought Aluminum Alloys*. Retrieved from MatWeb: <http://www.matweb.com/search/DataSheet.aspx?MatGUID=b8d536e0b9b54bd7b69e4124d8f1d20a>
- Tunna, L., O'Neill, W., Khan, A., & Sutcliffe, C. J. (2005). Analysis of laser micro drilled holes through aluminium for micro-manufacturing applications. *Optics and Lasers in Engineering*.

- Vahid Afroughsabet, L. B. (2019). Evaluation of Engineering Properties of Calcium Sulfoaluminate Cement-based Concretes Reinforced with Different Types of Fibers. *materials*.
- Walling, S. A., & Provis, L. J. (2016). Magnesia-Based Cements: A Journey of 150 Years, and Cements for the Future? *Chemical Reviews*, 116.
- Winnefeld, F., & Kaufmann, J. P. (2011). Concrete produced with calcium sulfoaluminate cement –. *First Middle East Conference on Smart Monitoring Assessment and Rehabilitation of Civil Structures*.
- Worden, K., Farrar, C. R., Manson, G., & Park, G. (2007). The fundamental axioms of structural health monitoring. *Proceedings of the Royal Society*.
- Yaws, C. L. (1999). *Chemical Properties Handbook*. McGraw-Hill.
- Yuan, Z.-G., & Kleinhenz, J. E. (2011). Measurement of Apparent Thermal Conductivity of JSC-1A. *AIAA Aerospace Sciences Meeting including the New Horizons Forum and Aerospace Exposition*.